ISSN 1880-8468

Technical Report of
International Development Engineering

国際開発工学報告

TRIDE-2016-04 May 9, 2016

Abstracts of Bachelor Theses
Presented in Feburary 2016

Department of International Development Engineering,
Graduate School of Science and Engineering,
Tokyo Institute of Technology
http://www.ide.titech.ac.jp/TR

Preface

Bachelor theses of Department of International Development Engineering, Tokyo Institute of Technology were presented successfully on August 4, 2015 and February 29, 2016, respectively. This technical report consists of the abstracts of those theses.

TECHNICAL REPORT OF INTERNATIONAL DEVELOPMENT ENGINEERING
TRIDE-2016-04

TABLE OF CONTENTS

Indoor Radio Propagation Prediction utilizing Diffuse Scattering Model

Student ID: 11_22001 Name: Haitao PANG
Supervisor: Junichi TAKADA, Kentaro SAITO

1. Introduction

In wireless communication systems designs, it is important to identify the characteristics of multipath effect, which results from myriad reflections and diffractions from walls, people and small objects in the propagation channel. The power delay profile (PDP) is the intensity of a signal received as a function of time delay. The PDP gives the time-domain signal spread in the multipath radio propagation, and it is important for the design of wireless communication system.

There are many existing techniques for predicting such multipath characteristics. For example, ray-tracing models based on geometric optics, finite-difference time-domain (FDTD) models, method of moment (MOM) models are among the popular ones. Although these models are proved to be accurate to some extent, they are time-consuming and they require specific inputs such as detailed geometry and accurate electromagnetic (EM) properties, which are not easy to get and thus quite unreliable sometimes.

On the other hands, the confinement of an indoor environment and the resemblance between room acoustic and room electromagnetics suggests applicability of existing methods in acoustics to indoor EM propagation. In [3] and [4], some of established acoustic knowledge is tested for EM scenarios. In this paper, we introduce a model for calculating PDP for an enclosure, which requires only three parameters: volume of the room, the surface area of the room and the overall equivalent absorption rate of the room surfaces. Experiment was also performed to verify the effectiveness of such an model.

2. Theories

2.1 Sabine's formula

Back to the beginning of the 20th century, W.C. Sabine has conducted various experiment and proposed an equation for indoor acoustics [1][2][3]. This equation is valid under two assumptions: total diffuse (or isotropic) field and energy conservation. Consider a narrow ray tube in direction (θ, φ), the rays of intensity is

$$dI(\theta,\varphi) = I(\theta,\varphi)\,\mathrm{d}\Omega \tag{1}$$

The corresponding energy density at a point is found by the intensity divided by the velocity of EM waves, equals to the speed of light

$$dw = \frac{I(\theta,\varphi)}{c} d\Omega \tag{2}$$

Since the field is fully diffuse, the intensity is independent of direction (θ, φ), so integrating the above equation over all directions gives the energy density

$$W = \frac{4\pi I}{c} \tag{3}$$

Assuming only a fraction α of overall incoming intensity is absorbed by indoor surface area A. Again knowing that $I(\theta, \varphi)$ is independent on any direction, the total absorbed power P_{abs} is

$$\begin{aligned} P_{abs} &= \alpha I A \int_0^{2\pi} d\varphi \int_0^{\pi/2} cos\theta sin\theta d\theta = \alpha A \pi I \\ &= \frac{\alpha A W c}{4} \end{aligned} \tag{4}$$

Under the law of conservation, the energy emitted inside the room is either dispersed into the room volume or absorbed by the indoor surfaces.

$$S(t) = V\frac{dW}{dt} + \frac{\alpha A c}{4} W \tag{5}$$

When the source is turned off $S(t) = 0$, then the above homogeneous differential equation can be solved as

$$\begin{aligned} &W(t) = W_0 e^{-2\delta t}, \\ &with\ \delta = \frac{c\alpha A}{8V}, W_0 = \frac{4S}{c\alpha A} \end{aligned} \tag{6}$$

This is also called as Sabine's equation. It describes the indoor power delay as a log linear function.

2.2 Free mean path and in-room PDP (IPDP) model

The free mean path l_c between reflections is the total path length divided by the number of wall collisions N during time t. According to [1][4], l_c can also be derived as relative to total volume V, total surface A and some constant F. F is dependent of the room shape. For simplicity we use 4 for typical rooms [4].

$$l_c = \frac{ct}{N} \equiv \frac{FV}{A} \equiv \frac{4V}{A} \tag{7}$$

Then the characteristic time t_c that a given set of rays makes one reflection is

$$t_c = 2\frac{t_c}{c} = \frac{8V}{cA} \tag{8}$$

Consider the overall average power reflection coefficient

$$\gamma = 1 - \alpha \tag{9}$$

Then the average power level of a bundle rays after n reflections is approximated by

$$P_n = D\frac{\gamma^n}{d_n^2} \tag{10}$$

D is a function of the transmitting and receiving antennas and

the transmitted power.

By normalizing the power to P_0 and initializing the delay time to 0 s, the power delay levels can be approximated by

$$PDP_0 = 1 \qquad \tau = 0, \qquad for\ n = 0$$
$$PDP_n = \frac{\gamma^n}{4n^2} \quad \tau = \frac{t_c}{2}(2n-1), for\ n \neq 0 \qquad (11)$$

2.3 The proposed model

In previous researches, the Sabine's equation predicts an log linear power decline and the experiment did show the same tendency in the late reflections but it failed to predict the power profile of early reflections [4]. Dunens and Lambert have suggested that reverberation described by Sabine's equation only occurs after several reflections, or more exactly after $8l_c/c\ s$ to $10l_c/c$ s [5]. On the other hand the IPDP model's prediction does not match well when there are many reflections. So we propose a model that combines two models, with a line-of-side (LOS) component, early reflections (before $5l_c/c$ s) with piece-wise power profile predicted by IPDP model, and late reflections (after $9l_c/c$ s) with log linear power decline predicted by Sabine's equation. The model are given as following

$$PDP_0 = P_t G_t G_r \left(\frac{\lambda}{4\pi d_0}\right)^2, PDP_n = \frac{PDP_0(1-\alpha)^n}{4n^2}$$
$$\tau_0 = \frac{d_0}{c}, \qquad \tau_n = \frac{t_c}{2}(2n-1) + \tau_0$$

with the above parameters, the power profile is

$$P(t) = \begin{cases} 0 \quad , for\ \tau < \tau_0 \\ \frac{PDP_1 - PDP_0}{\tau_c}(\tau - \tau_0), for\ \tau \quad > \tau \geq \tau_0 \\ \frac{PDP_2 - PDP_1}{\tau_c}(\tau - \tau_1), for\ \tau_2 > \tau \geq \tau_1 \\ \frac{PDP_3 - PDP_2}{\tau_c}(\tau - \tau_2), for\ \tau_3 > \tau \geq \tau_2 \\ \frac{PDP_5 - PDP_3}{2\tau_c}(\tau - \tau_3)\ , for\ \tau_5 > \tau \geq \tau_3 \\ \frac{4S}{c\alpha A} e^{-\tau\frac{c\alpha A}{4V}}\ , for\ \tau \geq \tau_5 \end{cases}$$

3. Experiment

3.1 Experiment background

The experiment was conducted in a room full of small objects. The width, depth, and height is 6.34 m, 5.65 m, and 3.46 m respectively. Two bi-conical antennae were used as transmitting and receiving antenna. The directivity of both antennae is omni-directional in both horizontal and vertical plane. Both antennae are set to be 1.2 m above ground. The transmitting antenna is located in the center of the room described as point B. And the receiving antenna is located at point A, C and D, with the distance to point B is 1.7 m, 2.2 m, 3 m respectively. In order to suppress the effect of rapid phasing, the measurement for each point was conducted at the measurement grid, which consists of 9 points within the 20 cm, by 20 cm square. A vector network analyzer (VNA) model No. VNB 8 produced by Rhode Schwarz is used as signal generator and also spectrum analyzer. The center frequency is set to 5 GHz. And for the purpose of maximizing delay domain resolution, the bandwidth is 1 GHz (4.5 GHz to 5.5 GHz) for this experiment.

3.2 Data processing

Since the data output for delay of the VNA is in frequency domain, we calculated the channel impulse response of each measurement point using inverse Fourier transform (IFT). Then we average the 9 experiment data around each receive antenna location to suppress phasing effect to obtain delay profile for each pair of antennae BA, BC and BD. Then we use the delay profile between 100 ns and 160 ns to calculate the decay rate 2δ of the log linear function with least square method. It is found to be 0.19 dB/ns. From the calculated data and with use of the volume of the room V and the inner surface of the room A we can calculate the overall equivalent absorption coefficient, in this experiment it is found to be 0.47.

$$\alpha = \frac{c\delta A}{8V} \qquad (12)$$

Then with α, V, A and the detected LOS component, we can calculate the overall PDP with the formulations given by the proposed model. Figure 1 shows the predicted and detected outcome for the experiment of BA.

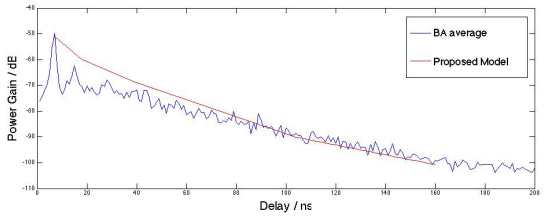

4. Conclusion

In analogy to applied acoustic theories, we proposed a prediction model for indoor radio propagation. Experiment was conducted to verify the model and the results showed well agreement between the model's prediction and the detected data. Still as part of the future work experiment conducted in more other rooms are needed. Although in the EM case polarization is important, in this research it is considered as vertical-vertical polarized. Therefore we need further consideration regarding to polarization in future works.

Reference

[1] H.Kuttruff, Room Acoustics, Fifth Edition, Spon Press

[2] W.C.Sabine, Collected Papers On Acousitcs, 1923, Harvard University Press

[3] J.B. Andersen *et al.*, Room Electromagnetics, Antennas and Propagation Magazine, IEEE (Volume 49, Issue: 2)

[4] C.L. Holloways *et al.*, A Model for Predicting the Power Delay Profile Characteristics Inside A Room, IEEE Transactions On Vehicular Technology (Volume 48, No.4, July 1999)

[5] E.K.Dunens and R.F.Lambert, Impulsive Sound-level Response Statistics in A Reverberant Enclosure, Journal Acoustics Society America (Volume 61, No.6 pp.1524-1532, 1977)

Acknowledgments I want to express my gratitude to professor Takada, Dr. Saito and other lab members, without whose support and encouragement I would be unable to finish this research.

Development of adhesion force measurement apparatus for glass-glass point contact

Student Number: 11B11718 Name: Mikhail SALYUKOV Supervisor: Kunio TAKAHASHI

1 Introduction

Understanding of the adhesion behavior between two solids is important in various fields of engineering, especially in designing the micro manipulation devices. JKR theory [1] explains the adhesion phenomena in a point contact between two solids by the work of adhesion. TMO theory [2] expands JKR theory by taking into account the effect of stiffness of the measurement system. Both theories are based on assumption of energy minimum condition, thus the path of the force curve during the contact process can be uniquely determined. However, the loading-unloading paths of the force curve are different in the practical contact system. Researches on adhesion hysteresis in the point contact using polymeric materials have been done to determine the main factor of the phenomena, and factors related to the properties of polymer materials are identified to influence the adhesion hysteresis [3-7].The experiments on adhesion hysteresis using non-polymeric materials are also needed to be conducted to know if the adhesion hysteresis is induced only by the properties of polymeric materials. In this paper, we developed the adhesion force measurement apparatus for glass-glass point contact i.e. contact between a convex glass lens and the plane parallel glass plate, by adjusting the parameters of the apparatus to achieve high measurement resolution ability and linear elasticity under high load conditions, which are the requirements for the apparatus that is capable of observing the adhesion hysteresis in the point contact between the non-polymeric materials.

2 Preliminary Estimations

For consideration of the requirements for the apparatus, we used the TMO point contact model (Fig.1) to estimate the range of the force curve and the required load resolution for its measurement. In the model, the force F working between two objects is obtained by eq.(1) as a function of contact radius a and gross displacement Z_t. The maximal adhesion force can be obtained by eq.(2).

$$F = \frac{2kEa}{2Ea + (1-\nu^2)k}\left(-Z_t - \frac{a^2}{3R}\right) \quad (1)$$

$$F_{adh} = -\frac{3\pi R\Delta\gamma}{2} \quad (2)$$

Among all the constant parameters in eq.(1) and eq.(2), curvature radius of the lens R and the stiffness of the measurement system k can be adjusted by the design of the apparatus. Considering the high load conditions of the experiment, pressure applied to the contact area must be lowered, to ensure the linear elasticity of the apparatus. The maximal adhesion force must be enhanced, taking into account the finite load resolution of the apparatus. From eq.(1) and eq.(2), it can be assumed that the curvature radius R must be increased to satisfy these conditions. Thus, the parameter of the curvature radius was set to R=2[m]. Using this value of curvature radius R and the physical properties of the glass ($\Delta\gamma$=0.03[J/m^2]), The maximal adhesion force can be calculated from eq.(2) to be F_{adh}= -0.28[N]. Thus, the load resolution of the apparatus needs to be no less than 0.01[N] to accurately measure the maximal adhesion force. Considering the installation of a motorized stage with a finite displacement resolution to control the gross displacement of two objects,

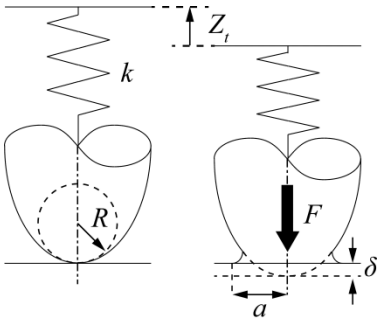

Fig.1 Schematic illustration of the TMO Point Contact Model

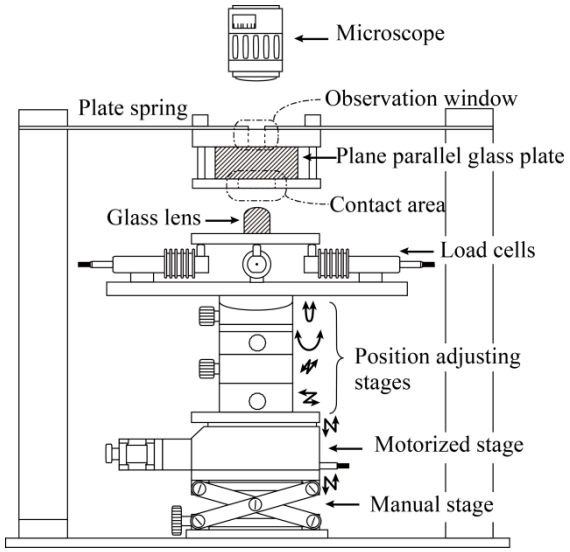

Fig.2 Schematic illustration of the apparatus

stiffness k must be decreased in order to decrease the change of load per unit displacement, and by that increase the load resolution of the apparatus. To obtain the necessary load resolution, we designed a plate spring mechanism with a spring constant of k_s=9882[N/m] and set the parameter of stiffness to this value.

3 Experimental

Based on the Preliminary estimations as above, adhesion force measurement apparatus for glass-glass point contact was developed as shown in Fig.2. An optical plane parallel glass plate (BK7,SIGMAKOKI Co.) was fixed in the center of a plate spring mechanism. Glass lens (BK7,SIGMA KOKI Co.) was set on a stage under the glass plate. Force F was measured using three load cells (LUB-B-10N,KYO WA Co.) set under the table with the lens. Motorized stage with a resolution of 0.73μm per step was used for manipulation of the gross displacement. The speed of the stage was set to 1step per sec. and the waiting period between steps to 5 sec. in order to minimize the dynamic influence. The contact experiment of two glass objects was conducted three times each for four different values (73μm, 146μm, 365μm, 730μm) of the maximal gross displacement Z_{tmax}, within the linear elasticity of the apparatus. An optical microscope was used to observe the contact area and measure the contact radius a through an observation window on the upper side of the plate spring. Both param-

eters F and a were measured simultaneously in the contact process.

4 Results and Discussions

The required load resolution of the apparatus was achieved by the proper design of the glass lens and the plate spring. Adhesion force was observed and measured with an accuracy of 0.01[N] in the point contact experiment of two glass objects, as demonstrated in Fig.5. Measured F_{adh} could be assumed to have dependence on Z_{tmax}, as shown in Fig.5. The observation of the contact area was done throughout the experiment, and the Newton's rings (i.e. a concentric interference pattern created by the reflection of light between two surfaces) were observed. As shown in Fig.6, the contact radius a was measurable as a radius of a dark reflection spot at the center of the pattern, when the force F was relatively large. In case of when the force F was small (e.g. at the beginning of the point contact), the contact radius a could not be measured due to the bright fringe formed in the center of the Newton's rings. This phenomenon could be attributed to the existence of the substances such as sub-micron sized particles on the surfaces of the two glass objects.

5 Conclusions

Adhesion force measurement apparatus for glass-glass point contact was developed using the TMO Point contact model for estimation of the necessary values of the parameters R and k, in order to achieve the high load resolution and linear elasticity under the high load conditions of the experiment. The maximal adhesion force F_{adh} was measured under four different maximal gross displacement $Z_{tmax.}$ From the results of the adhesion force measurement experiment, the apparatus was confirmed to have the load resolution required to measure the adhesion force in the glass-glass point contact. From the experimental results, the maximal adhesion force F_{adh} is suggested to have dependence on the maximum gross displacement Z_{tmax}. The contact radius a was measurable within the high load conditions, as a radius of the center of the Newton's rings. Effect of the sub-micron size particles on the surfaces of the two glass objects is considered to explain the inability to measure the contact radius a under a low load.

References

[1] K. L. Johnson, K. Kendall and A. D. Roberts: Proc. R. Soc. London A 324 (1971), pp. 301-313.
[2] K. Takahashi, R. Mizuno and T. Onzawa: J. Adhesion Sci. Technol., Vol. 9, No. 11 (1995), pp. 1451-1464.
[3] K. L. Johnson: Tribology International, Vol. 31, No.8 (1998), pp. 413-418
[4] G. Y. Choi, S. Kim and A. Ulman: Langmuir, Vol. 13, No. 23 (1997), pp.6333-6338
[5] H. She, D. Malotky and M. K. Chaudhury: Langmuir, Vol. 14, No. 11 (1998), pp.3090-3100
[6] Z. Wei, M. He and Y. Zhao: J. Adhesion Sci. Technol., Vol. 24, No. 6 (2010), pp. 1045-1054.
[7] H. Kesari, J. C. Doll, B. L. Pruitt, W. Cai and A. J. Lew: Philos. Mag. Lett., Vol. 90, No. 12 (2010) pp. 891–902

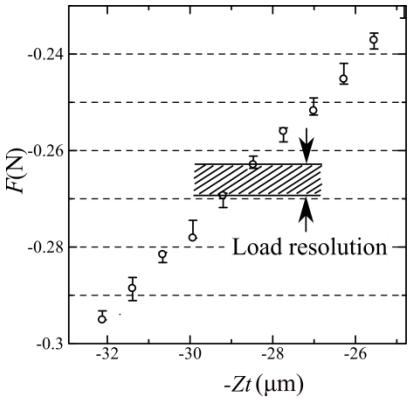

Fig.4 Load resolution of the apparatus (Z_{tmax}=730μm)

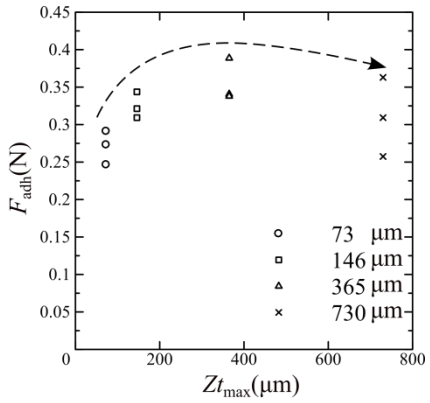

Fig.5 Relation between maximal gross displacement Z_{tmax} and maximal adhesion force F_{adh}

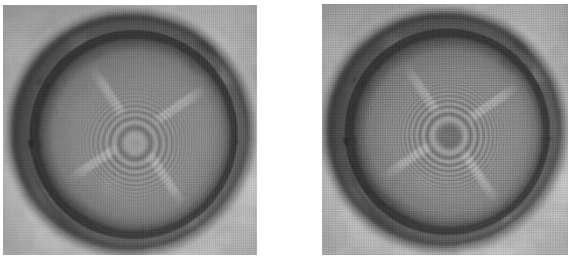

Fig.6 Newton rings observed at the contact surface under the low load (left) and high load (right)

Selective Catalytic Reduction of Nitrogen Oxides with Propene over Nb/TiO_2 catalyst supported Ba

Student Number: 11-27027 Name: Takuya Yoneda Supervisor: Hirofumi HINODE

1. Introduction

Nitrogen oxides (NO, NO_2 and N_2O) are major sources of atmospheric environmental problems such as photochemical smog, acid rain, ozone depletion and greenhouse effects. Furthermore, presence of nitrogen oxides in the atmosphere can cause problems to human health. Most of the NO_x comes from automobiles (48.5%) and power plants (46.2%) using fossil fuels [1].

Nowadays, three-way catalysts (TWC) are generally used to reduce NO_x in automobiles. This method can reduce NO_x with high efficiency at specific air to fuel (A/F) ratio. However, the development of lean-burn engines that have higher fuel economy and cleaner emissions requires catalyst for NO_x reduction that can function also at higher A/F ratio which cannot be achieved using TWC only. One potential method to reduce NO_x in exhaust gas is selective catalytic reduction of NO using hydrocarbon as reducing agent (HC-SCR of NO) [2]. Previous study showed that TiO_2 supported Nb catalyst was effective in HC-SCR of NO [3]

Therefore, in this study, the catalytic activities of Ba-Nb/TiO_2 catalysts prepared by two different methods, impregnation (IM) and manual mixing (MM), were investigated for HC-SCR of NO_x using propene as reducing agent.

2. Experimental

Nb/TiO_2 catalyst was prepared by impregnated method using TiO_2 (JRC-TIO-7) and $C_4H_4NbO_9 \cdot (H_2O)_5$ (ALDRICH) as precursors with the objective molar ratio for Ti and Nb[4]. First, $C_4H_4NbO_9 \cdot (H_2O)_5$ was dissolved in 300 ml deionized water with continuous stirring and TiO_2 was added to the solution and mixed. The resulting mixture was filtered, dried at 100℃ for 8 h and calcined at 550℃ in air for 5 h. The catalyst prepared by IM method was designated Nb/TiO_2.

In the case of consecutive IM method, $Ba(NO_3)_2$ (Wako) was dissolved in 300 ml of deionized water and mixed with Nb/TiO_2. Then the mixture was stirred at room temperature for 24 h and dried at 100℃ for 12 h. The catalyst prepared by consecutive IM method was designated $Ba/Nb/TiO_2$.

In the MM method, BaO (WAKO) is used prior to mixing with Nb/TiO_2 prepared earlier. The mixing was carried out by hand using a mortar and pestle with a little amount of ethanol. Finally, the catalysts were crushed and sieved to 0.71-1.00 mm [4]. The catalyst prepared by MM method was designated BaO+ Nb/TiO_2.

The HC-SCR activity experiments were carried out in a fixed-bed flow reactor. The reactant gas was composed of 1500 ppm NO, 10% O_2, 1500 ppm C_3H_6 and He as a balance gas. 0.8~1.2 g catalyst was used with a corresponding space velocity of 13000 h^{-1}. The temperature was changed stepwise from 150℃ to 550 ℃.

NO and NO_2 concentration were analyzed by NO_x analyzer (Shimadzu, NOA-7000). N_2O, CO_2 and CO were analyzed by gas chromatograph (GL Science, GC-323w for N2O; GL Science, GC-390 for CO_2 and CO). The catalysts were characterized by TG-DTA, XRD, and N_2 adsorption (Autosorb 1MP/TSU, BET analysis).

3. Results and discussion

Figure 1 shows the conversion of NO to N_2 over TiO_2, Nb/TiO_2, 10wt% $Ba/Nb/TiO_2$ 10wt% BaO+Nb/TiO_2 (BC and AC) catalysts. Nb/TiO_2 catalyst shows the highest activity at 350℃.

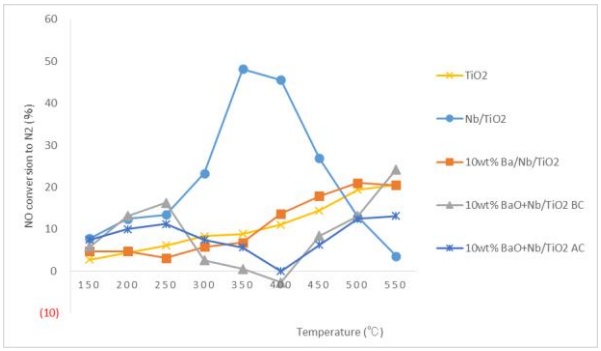

Fig.1. Catalytic activity of TiO_2, Nb/TIO_2, 10wt%$Ba/Nb/TiO_2$, 10wt%BaO+Nb/TiO_2 BC, 10wt%BaO+Nb/TiO_2 AC for the reduction of NO to N_2 using C_3H_6 as a reductant.

Figure 2 shows the conversion of NO to N_2 over BaO+Nb/TiO_2 catalysts by MM method with Ba

loading levels from 0-20 wt%. Catalyst with 0% BaO showed the highest catalytic conversion at 350℃ followed by 1% and 5%. However, further increase of Mo loading to 10% and 20% showed a decrease in activity as compared to the bare Nb/TiO_2 catalyst.10% and 20% showed the negative conversion at 400℃. BaO has a storage capacity for any gas.[5] It was thought that at lower temperature, NO was adsorbed to BaO, which then be released at 400 ℃ and caused negative conversion.

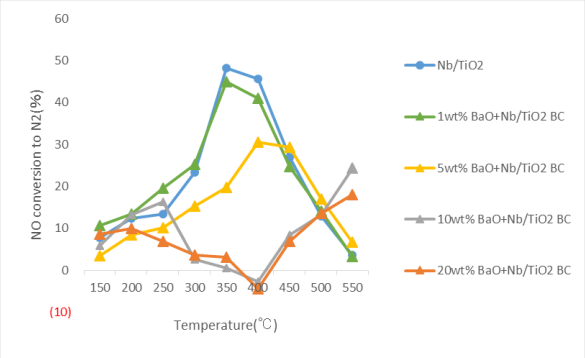

Fig.2. Catalytic activity of $BaO+Nb/TiO_2$ MM method catalyst for the reduction of NO to N_2 using C_3H_6 as a reductant.

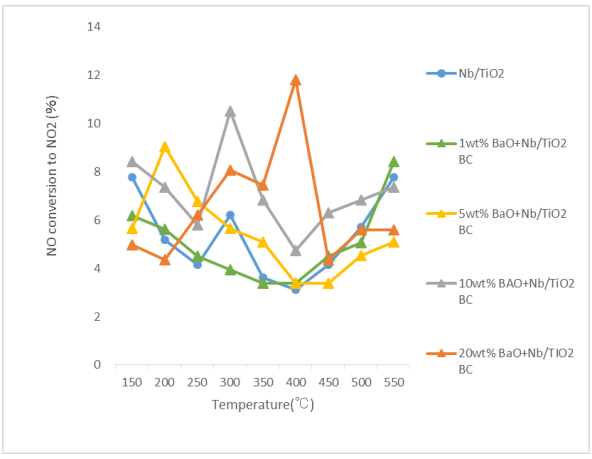

Fig.3. Catalytic activity of $BaO+Nb/TiO_2$ MM method catalyst for the conversion of NO to NO_2 using C_3H_6 as a reductant.

Figure 3 shows the conversion of NO to NO_2 over $BaO+Nb/TiO_2$ catalysts by MM method with Ba loading levels from 0-20 wt%. It can be seen that there is a sharp increase in the conversion of NO to NO_2 in which the conversion of NO to N_2 decreases (Fig. 2) with 20% MM method prepared catalyst convert NO to NO_2 starting at a lower temperature than bare Nb/TiO_2. The result shows 20% MM method prepared catalyst has a storage capability for NO_2.

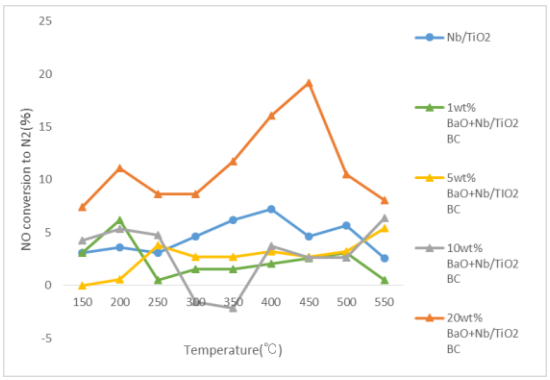

Fig.4. Catalytic activity of $BaO+Nb/TiO_2$ MM method catalyst for the reduction of NO to N_2 not using C_3H_6 as a reductant.

Figure 4 shows the conversion of NO to N_2 over all catalysts by IM and MM method with Ba loading levels from 0-20 wt%, without C_3H_6. It can be seen that there are much lower catalytic conversion compared to result using C_3H_6 for almost all catalysts except 20% MM method prepared catalyst. The result shows that the addition of C_3H_6 is necessary for the catalytic conversion of NO to N_2 oxidation-reduction reaction while a decrease in the conversion to NO_2.

.

4. Conclusions

The catalyst prepared by MM method $BaO+Nb/TiO_2$ catalyst showed catalytic activity towards selective catalytic reduction of NO to N_2 with C_3H_6 as reducing agent. Compared to the consecutive IM method, MM method exhibited higher activity and showed high storage capability. The addition of BaO with MM method reduced the activity of catalyst.

References

[1] Norio Arai Techno-System Corp (1997)

[2] R.Burch, T.C.Watling, Appl.Catal.B, 11, 207 (1997)

[3] Megumi Makii; Master Thesis, Tokyo Institute of Technology (2007)

[4] Yang Wang; Master Thesis, Tokyo Institute of Technology (2010)

[5] Naoki Takahashi; Doctor Thesis Nagoya University (2007)

Thermal Analysis of lithium evaporation process to fabricate lithium-drifted silicon detector for a dark-matter search project GAPS

Student Number : 12_01717 Name : Yosei Inoue Supervisor : Daisuke Akita

1 Introduction

It is said that in our universe a substance called dark matter exists in addition to normal substance.

Various theoretical models of dark matter have been proposed. Cold Dark Matter (CDM) , such as supersymmetric neutralino, is a candidate and is expected to generate antideuterons via pair annihilation or decay. GAPS project currently persued by JAXA and several institutes in Japan and US aims to search for antideuterons originated from CDM by using lithium-drifted silicon semiconductor detectors.[1]

In order to get a high antideuteron sensitivity, it is necessary to enlarge the detector fiducial volume while ensuring the performance of the detector. Among the detector manufacturing process, it is known that the uniformity of the heated temperature of silicon wafer during the lithium evaporation process in vacuum is essential to ensure good detector quality. Also, it is known the smaller the difference of the temperature between the heat source and the silicon wafer are, the shorter the production time of the detector becomes. To realize stable mass production of the detector, it is important to understand the heat transfer mechanism of the heating device and specify the factors to uniform the temperature and reduce the difference of temperature between the heat source and the silicon wafer.

In this paper, I conducted a numerical modeling and a thermal analysis of the heating device and compared the calculated temperature with the actual measured data in order to consider the heat transfer mechanism. The temperature measurement was conducted by Shimazdu Co., Ltd., which co-develops the silicon detector for the GAPS project.

2 Thermal Analysis

The thermal analysis was conducted by using a thermal analysis software, Thermal Desktop, which uses the finite difference method and the Monte Carlo method.

In vacuum, heat transfer is dominated by conduction heat transfer and radiation heat transfer. To reproduce the nonuniformity of the temperature at the silicon surface, I focused on the difference of the heat flux between conduction heat transfer and radiation heat transfer. Generally, it is known that the heat flux of conduction heat transfer is much larger than that of the radiation heat transfer. Figure 1 shows a conceptual diagram of the evaporation system.

The heating device consists of a hotplate, a holder, a silicon wafer, and a cover. All of their surfaces are machined flat but are not completely flat. Therefore when they are piled up, there must be some non-contact area with a tiny gap. Heat transfer in the contact area is dominated by the conduction heat transfer, and the non-contact area must be dominated by the radiation heat transfer. So, I anticipated that these mappings influence the nonuniformity of the temperature.

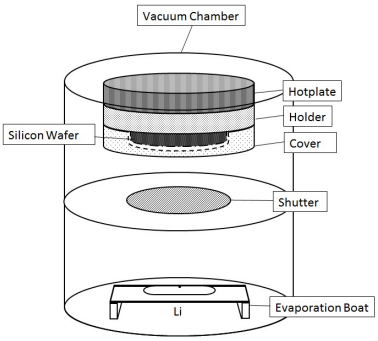

Figure 1: Evaporation system

In the thermal analysis, the contact area and the contact conductance per unit area must be assumed. However, it is difficult to evaluate them accurately. In this paper, the contact area is simulated by a model, and the contact conductance is treated as a parameter in a realistic range between 80 and 2000 $\mathrm{W \cdot m^{-2} \cdot K^{-1}}$.[3] Four cases of 80, 100, 1000, 2000 $\mathrm{W \cdot m^{-2} \cdot K^{-1}}$, called simulation (1)〜(4), are assumed, respectively. The Model 1 in Figure 2 shows the assumed contact area. In order to confirm it is correct, it must be verified the Model 1 reproduces experimental result and the Model 2 and the Model 3 in Figure 2 do not reproduce experimantal result.

At 1 atm environment, there is gas in the small gap of the non-contact area. Gas in the small gap couples the heat transfer between the both surfaces that can be approximated by direct contact heat transfer in the whole area (equal to Model 2 in Figure 2). The simulated temperature was compared with the experimental results at 1 atm, too.

3 Results

Figure 3 shows the comparison of the simulated temperatures of Model 1, 2, and 3 with the experimental results of silicon wafer in vacuum. Futher, simulation (2) and (3) of Model 2 and 3 are omitted because simulation (2) and (3) must be placed between simulation (1) and (4).

The experimental data locate between simulaion (2) and (3) for Model 1. Therefore, the simulated temperatures reproduce the experimental data well. On the

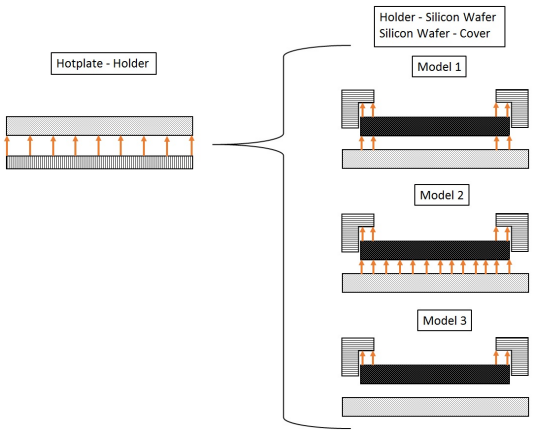

Figure 2: Assumed contact area and compared contact area (wafer diameter : 4 inch)

other hand, the experimantal data locate out of simulated range for Model 2 and Model 3. Therefore, the simulated temperatures don't reproduce the experimental data. From the above, the validity of Model 1 is shown.

Focused on simulation (2) and (3) of Model 1, the temperature distribution at silicon surface is in the range of $\pm 0.70 \sim 2.07$ K. Also, the differenece of the temperarure between hotplate and silicon wafer is about 100 K.

Figure 4 shows the comparison of the analysis results with the experimental data of silicon wafer at 1 atm.

The experimental data locate between the simulation (2) and (3). So the entire surface contact model reproduces the experimental data at 1 atm well. This result corroborates the validity of the numerical model.

Focused on simulation (2) and (3), the temperature distribution at silicon surface is in the range of $\pm 0.21 \sim 0.58$ K, and we can find it is improved compared with it in vacuum. Also, the difference of the temperature between hotplate and silicon wafer is about 20 K, and we can find it is improved compared with it in vacuum.

From the above, the major factor of the nonuniformity of the silicon temerature and the difference of temperature between hotplate and silicon wafer is considered to be the existence of the non-contact area between the parts. Also, we can improve them if we can make a thermal condition corresponding to 1 atm in vacuum.

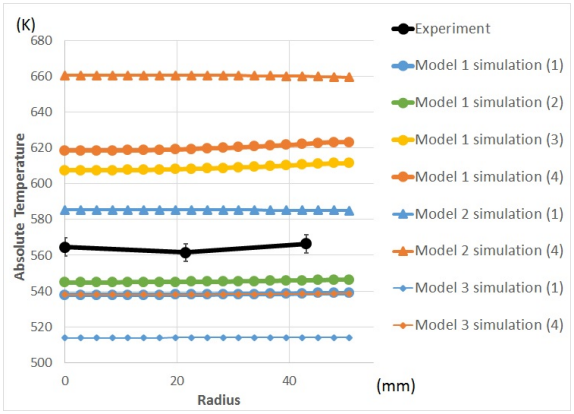

Figure 3: Comparison of the simulated temperatures using Model 1, 2, 3 with the experimental data about the slicon wafer temperature in vacuum

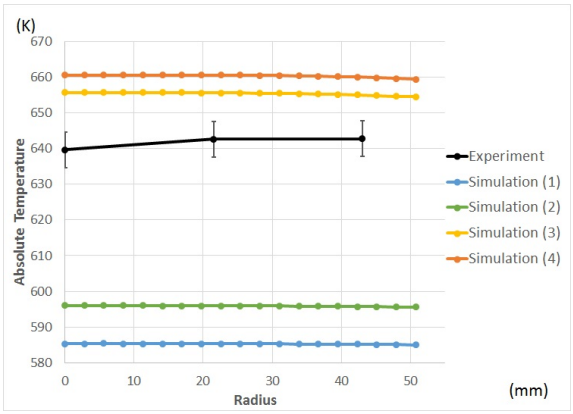

Figure 4: Comparison of the simulated temperature with the experimental data about the silicon wafer temperature at 1 atm

4 Conclusions

In this paper, I conducted a modeling and a thermal analysis of the heating device for the lithium evaporation process to produce lithium-drifted silicon detectors, and compared the simulated temperature with experimental data. As a result, the followings can be concluded:

- The experimental data are well reproduced by the heat contact model shown by Model 1 in Figure 2.
- The major reason which causes the nonuniformity of the silicon temperature and the difference of temperature between hotplate and silicon wafer is considered to be the existence of the non-contact area between the parts.
- Reproduction of the experimental data at 1 atm by the entire contact model also confirms the validity of the model.
- The nonuniformity of the silicon temperature and the difference of the temperature between hotplate and silicon wafer can be improved if a thermal condition corresponding to 1 atm in vacuum is realized.

Acknowledgments

I would like to thank Dr. Hideyuki Fuke, and Dr. Shun Okazaki, JAXA/ISAS and Mr. Minoru Yamada, Shimazdu Co., Ltd. for their instructions for this study.

References

[1] Hideyuki Fuke. Report of the current state of a cosimic ray antiparticle search project GAPS by a polar patrol balloon. Balloon Symposium2015

[2] T.Aramaki. Antideuteron Sensitivity for the GAPS Experiment. 2015. [pdf] Available at:⟨ `http://arxiv.org/pdf/1506.02513.pdf` ⟩ [Accessed 18 February 2016].

[3] David G. Gilmore ed. Spacecraft Thermal Control Handbook Volume 1: Fundamental Technologies

Applicability of a 3D Numerical Model for Assessing the Effectiveness of Wooden Pile Breakwaters

Student Number: 11_13752 Name: Shoya Sekiguchi Supervisor: Hiroshi Takagi

1. Introduction

In developing countries, coastal cities often experience rapid economic development because of their geographical advantages. However, some detrimental effects from these developments are often ignored. One of these negative effects is coastal erosion. Coastal erosion is a process which occurs when beaches are approaching its disequilibrium profile. If the beach receives less sand than outbound sand volume, an erosion likely occurs, causing an increase in coastal vulnerability. In Phan Thiet, local people have installed wooden piles to prevent coastal erosion as a wave-breaking countermeasure. However, these piles are randomly placed and there has been no extensive research conducted about the effects of these wooden piles. Therefore, the purpose of this research is to develop the methods with a 3D numerical model to assess the effectiveness of wooden pile breakwaters.

Fig1. Coastal erosion in Phan Thiet city, Vietnam (January, 06, 2012)

2. Coastal erosion in Phan Thiet

Phan Thiet is a coastal city located in southern Vietnam. It is a popular tourist spot with numerous resorts and hotels near the beach area. Recently, the coastal areas of the city have been suffering from severe coastal erosion problems caused by coastal development such as land reclamation and jetties. In Duc Long, a small coastal community in Phan Thiet, several dozens of houses have been destroyed by serious erosion problem and still a number of houses are on the verge of disappearance. According to the 2001 and 2010 coastline, the beach appears to have retreated towards the shore by about 40m. According to Takagi (2014), the coastline would retreat by more than 30m as it gradually approaches its equilibrium beach profile. The community has set up wooden piles and sandbags to break waves and prevent erosion but this has not showed any significant effects.

3. Numerical analysis

In this research, numerical analysis was carried out using IhFoam which is a solver of OpenFOAM, which is an open-source software. IhFoam is a three-dimensional two-phase flow solver using VOF method. Figure 2 shows the geometry of this simulation which was derived from the measured bathymetry of Duc Long. The simulation was carried out for five cases: (1) “No pile”, (2) “Single pile”, (3) ”20.0cm spacing between each pile”, (4) “10.0cm spacing between each pile” and (5) “Thin vertical wall instead of piles”. Figures 2 and 3 show the case of “20.0cm spacing between each pile”. Table 1 indicate the settings used in the numerical simulation.

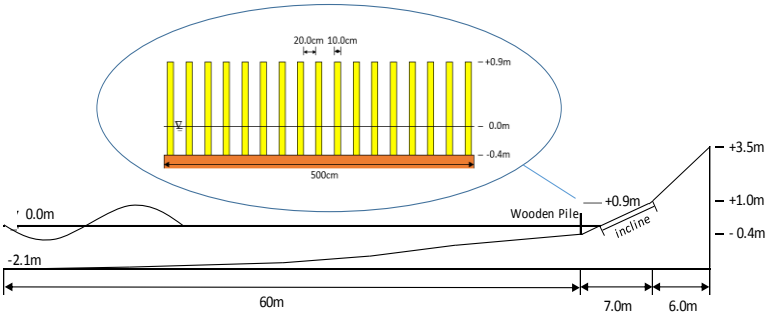

Fig2. Geometry of simulation (cross-shore direction) and Wooden pile model assumed in Case 3 (alongshore direction)

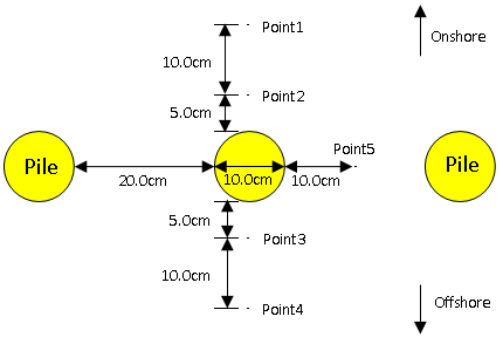

Fig3. Observation points around the pile

Table1. Calculation settings

Item	Outline
Mesh size	3.47～100cm cube mesh
Time step	⊿t=less than 0.01sec
Wave height	H=1.0m
Wave period	T=8.0sec
Wave theory	Cnoidal theory
Turbulence	LES model
LES SGS	Smagorinsky

4. Assessment of wooden pile

This research proposes three criteria to evaluate the performance of wooden pile breakwaters. The first criterion is the wave run-up height. Figure 4 shows that the run-up height tends to decrease as the spacing between piles is reducing. The second criterion is the maximum bending stress acting on the pile. In Figure 5, the “Wall” case has the largest bending stress and the stress is much larger compared to other cases. Figure 5 indicates that the bending stress acting on the pile tends to increase as the spacing between the piles is reduced. One of the reasons for this result is that an increase of the spacing between piles releases wave energy by passing it through between the piles. Given the bending strength of Larch with a diameter of 10.1~13.8cm is about 36~57 MPa, however, the pile would not snapped by the impact of waves considered in this study. On the other hand, the vertical wall is subjected to high bending stresses because the structure receives the entire wave energy.

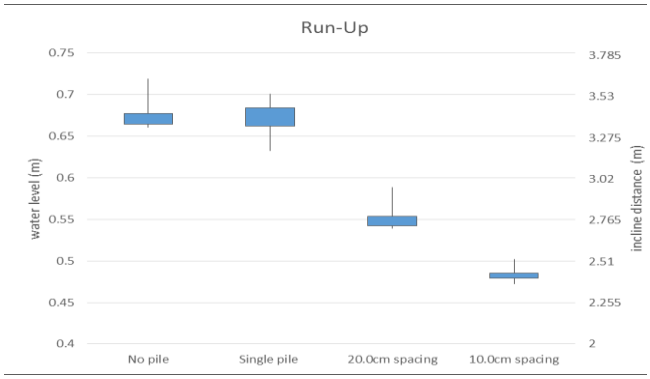

Fig4. The run-up heights and incline distances of the waves

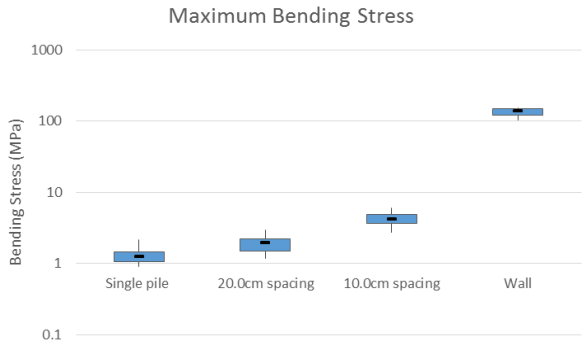

Fig5. The maximum bending stress

The third criterion is the sediment transport around the piles based on the velocities of the bottom flow inputted into the dimensionless sediment transport calculation formula as suggested by Dibajnia and Watanabe (1992). Inui et al. (1995) and Yamashita et al. (1996) extended this formula as

$$\Phi_{net} = \frac{q_{net}(1-\lambda)}{w_0 d} = 0.0023 \cdot \mathrm{sign}(\Gamma)|\Gamma|^{0.5} \tag{1.1}$$

$$\Gamma = \frac{u_c T_c(\Omega_c^3+\Omega_t'^3) - u_t T_t(\Omega_t^3+\Omega_c'^3)}{(u_c+u_t)T} \tag{1.2}$$

$$u_c^2 = \frac{2}{T_c}\int_0^{T_c} u^2\,dt \ , \ u_t^2 = \frac{2}{T_t}\int_{T_c}^{T} u^2\,dt \tag{1.3}$$

$$\begin{cases} \text{if } \omega_j \le \omega_{cr} \begin{cases} \Omega_j = 0 \\ \Omega_j' = \omega_j \cdot \frac{2w_0 T_j}{d} \end{cases} \\ \text{if } \omega_j \ge \omega_{cr} \begin{cases} \Omega_j = (\omega_j - \omega_{cr}) \cdot \frac{2w_0 T_j}{d} \\ \Omega_j' = \omega_{cr} \cdot \frac{2w_0 T_j}{d} \end{cases} \end{cases} \tag{1.4}$$

$$\omega_c = \frac{1}{2}\frac{u_c^2}{sgw_0 T_c} \ , \ \omega_t = \frac{1}{2}\frac{u_t^2}{sgw_0 T_t} \tag{1.5}$$

where Φ_{net} is the dimensionless sediment transport, q_{net} is the sediment transport volume per unit time and unit width, λ is the void fraction, w_0 is the sedimentation rate of sand, d is the particle size of the sand, s is the water specific gravity of sand, g is the acceleration of gravity, T is the wave period and ω_{cr}, the function related in the sediment transport system, becomes 0 at the time of sheet flow. The individual waves are defined by the zero-upcrossing method and *j* in Eq. (1.4) will be replaced by *c* or *t*.

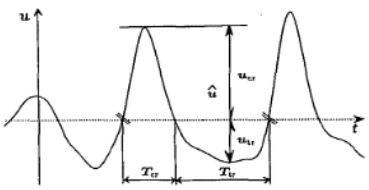

Fig6. The definitions of the symbols (Yamashita et al., 1996)

The velocities were observed at five points in Figure 3. Figure 7 shows the result of calculation and the length of vectors is the amount of dimensionless sediment transport Φ_{net}. According to Figure 7, at Point3 and Point4 the "Wall" case has a large effect in transporting the sand offshore. This can be explained by considering that the waves, which are mostly reflected by the wall, intensify wave-induced flows towards offshore. Moreover, it is apparent that when the spacing between piles becomes narrower, the sand is more likely transported offshore. Finally, both of the "20.0cm spacing" and the "10.0cm spacing" cases have a significant effect on transporting the sand offshore at Point 5. One of the reasons for this result is that the spacing between piles accelerates the velocity of waves which passes through between the piles.

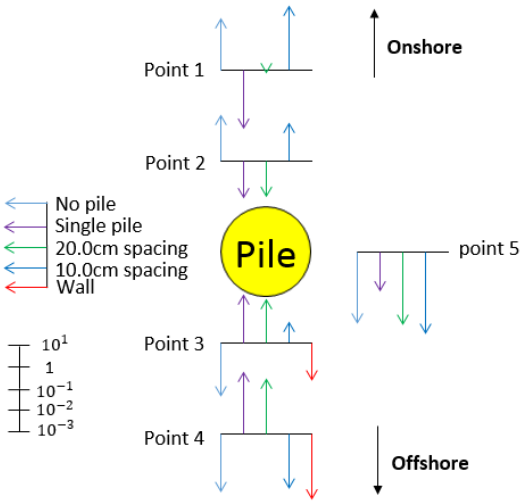

Fig.7 The amount of dimensionless sediment transport

5. Conclusion

By coupling with the 3D numerical analysis, this research proposed three criteria to assess the performance of wooden pile breakwaters that aim at mitigating coastal erosion. The difference in wave run-up and velocity around the structures were clearly observed according to the difference in the pile arrangement. This research proved that the methodologies proposed in this study can be used to design wooden pile breakwaters.

References

[1] Takagi H. et al., Coastal Vulnerabilities in a Fast-Growing Vietnamese City, *Coastal Disasters and Climate Change in Vietnam*, Elsevier, pp.157-171, 2014

[2] Dibajnia, M. and A. Watanabe, Sheet Flow under Nonlinear Waves and Currents, *Proc. 23rd Int. Conf. on Coastal Eng.*, ASCE, pp. 2015-2028, 1992

[3] 乾ら, 細粗混合砂のシートフロー漂砂量の算定式について, 海岸工学論文集, 第 42 巻, 1995

[4] 山下ら, 不規則波浪下でのシートフローによる漂砂量算定式, 海岸工学論文集, 第 43 巻, 1996

[5] 徳島県立農林水産総合技術センター森林林業研究所, すぎ(間伐) 丸太の強度, 技術情報カード, No.47, 2003

Image matching using affine-invariant GAT correlation method

Student Number: 10B07895 Name: Tiansheng Jin Supervisor: Yukihiko YAMASHITA

1 Introduction

Image matching refers to a process of recognizing a specific object in an image. Template matching is a technique in image matching for finding small parts of an image which match a template image. A basic method of template matching is the normalized cross-correlation (NCC). NCC has qualities such as high accuracy, high adaptable, and strong anti-jamming. However it is sensitive to the deformation of images. To this issue, the validity of a method using the global affine transformation (GAT) correlation has been reported. In this study, an experiment using an improved GAT correlation method in the image matching has been performed. And the validity of the method is examined.

2 Global affine transformation correlation

2.1 Normalized cross-correlation

Consider there are two images, the input image $\mathbf{F}$ and the target image $\mathbf{G}$, which are represented by gray level function $f(\boldsymbol{x})$ and $g(\boldsymbol{x})$ respectively, as $\mathbf{F} = f(\boldsymbol{x}),\ and\ \mathbf{G} = g(\boldsymbol{x}),\ \boldsymbol{x} \in \boldsymbol{K}$, where $\boldsymbol{x}$ denotes a 2D location vector defined in the bounded 2D domain of $\boldsymbol{K}$. By using the theory of definite canonicalization:

$$\int_{\boldsymbol{K}} f(\boldsymbol{x})d\boldsymbol{x} = 0,\ \int_{\boldsymbol{K}} g(\boldsymbol{x})d\boldsymbol{x} = 0,$$
$$\int_{\boldsymbol{K}} f(\boldsymbol{x})^2 d\boldsymbol{x} = 1,\ \int_{\boldsymbol{K}} g(\boldsymbol{x})^2 d\boldsymbol{x} = 1,$$

we obtain the matching measure of normalized cross-correlation simply given by:

$$C(f,g) = \int_{\boldsymbol{K}} f(\boldsymbol{x})g(\boldsymbol{x})d\boldsymbol{x}. \tag{1}$$

However, there is still the problem that the correlation measure in itself cannot compensate for geometric image distortion such as affine transformation.

2.2 Global affine transformation correlation

GAT is a uniform affine transformation as applied to an input gray-scale image $\mathbf{F}$. A 2D affine transformation from vector $\boldsymbol{x}$ to $\boldsymbol{x}'$ can be expressed by

$$\boldsymbol{x}' = \boldsymbol{A}\boldsymbol{x} + \boldsymbol{b} \tag{2}$$

Let $f(\boldsymbol{x})$ and $g(\boldsymbol{x})$ be an input image to be transformed and a target image. Let $f_A(\boldsymbol{x})$ be the transformed image of the input image $f(\boldsymbol{x})$. Then we have

$$f_A(\boldsymbol{z}) = \frac{1}{\sqrt{|\boldsymbol{A}|}} f(\boldsymbol{A}^{-1}(\boldsymbol{z} - \boldsymbol{b})), \tag{3}$$

which is different from the conventional $f_A(\boldsymbol{x}) = \frac{1}{|\boldsymbol{A}|} f(\boldsymbol{A}^{-1}(\boldsymbol{z}-\boldsymbol{b}))$. The reason why I apply the root determinant term is to insure the variance of transformed image to be one. Therefore, the correlation is given by $C(f_A, g) = \int_{\boldsymbol{K}} \frac{1}{\sqrt{|\boldsymbol{A}|}} f(\boldsymbol{A}^{-1}(\boldsymbol{x}-\boldsymbol{b}))g(\boldsymbol{x})d\boldsymbol{x}$. However, $\boldsymbol{A}$ and $\boldsymbol{b}$ are directly embedded in the variable of function f, it requires exhaustive trials and errors to determine optimal $\boldsymbol{A}$ and $\boldsymbol{b}$. To eliminate this step, I change the function by using the Gaussian function, let $\boldsymbol{A}$ and $\boldsymbol{b}$ appear only in the Gaussian function. Furthermore, in order to achieve a higher process speed, I introduce a new edge direction function

$$q(\boldsymbol{v}) = \begin{cases} 0 & (||\boldsymbol{v}||) = 0) \\ n & (||\boldsymbol{v}||) > 0 \\ & \frac{\pi(n-1)}{4} - \frac{\pi}{8} \le \arg(\boldsymbol{v}) < \frac{\pi(n-1)}{4} + \frac{\pi}{8}) \end{cases}$$

As a result, it reinforces the contribution of steep regions or edges to correlation for matching while suppressing or neglecting the contribution of flat regions or grounds. Finally the criterion for GAT correlation is given by

$$JGAT = \iiiint G(\boldsymbol{A}\boldsymbol{x}_1 + \boldsymbol{b} - \boldsymbol{x}_2)\delta_{>0}(q(\nabla f(\boldsymbol{x}_1)), q(\nabla g(\boldsymbol{x}_2)))f(\boldsymbol{x}_1)g(\boldsymbol{x}_2)\sqrt{|\boldsymbol{A}|}d^2\boldsymbol{x}_1 d^2\boldsymbol{x}_2. \tag{4}$$

3 Successive iteration bethod for optimal GAT determination

3.1 Optimization

Following the necessary condition of maximization yields both derivatives of J_{GAT} equal to zero with re-

spect to each element of $\boldsymbol{A}$ and $\mathbf{b}$. By defining

$$\begin{aligned} F(\boldsymbol{x}_1, \boldsymbol{x}_2) &= G(\boldsymbol{x}_1 - \boldsymbol{x}_2)\delta_{>0}(q(\nabla f(\boldsymbol{x}_1)), \\ &\quad q(\nabla g(\boldsymbol{x}_2)))f(\boldsymbol{x}_1)g(\boldsymbol{x}_2), \quad (5) \\ \overline{1} &= \iiiint F(\boldsymbol{x}_1, \boldsymbol{x}_2)d^2\boldsymbol{x}_1 d^2\boldsymbol{x}_2, \quad (6) \\ \overline{\boldsymbol{x}_1} &= \iiiint F(\boldsymbol{x}_1, \boldsymbol{x}_2)\boldsymbol{x}_1 d^2\boldsymbol{x}_1 d^2\boldsymbol{x}_2, \quad (7) \\ \overline{\boldsymbol{x}_2} &= \iiiint F(\boldsymbol{x}_1, \boldsymbol{x}_2)\boldsymbol{x}_2 d^2\boldsymbol{x}_1 d^2\boldsymbol{x}_2, \quad (8) \\ \overline{\boldsymbol{x}_1\boldsymbol{x}_1^T} &= \iiiint F(\boldsymbol{x}_1, \boldsymbol{x}_2)\boldsymbol{x}_1\boldsymbol{x}_1^T d^2\boldsymbol{x}_1 d^2\boldsymbol{x}_2, \quad (9) \\ \overline{\boldsymbol{x}_2\boldsymbol{x}_1^T} &= \iiiint F(\boldsymbol{x}_1, \boldsymbol{x}_2)\boldsymbol{x}_2\boldsymbol{x}_1^T d^2\boldsymbol{x}_1 d^2\boldsymbol{x}_2 \quad (10) \end{aligned}$$

and substituting it into the differential equations, we have

$$\boldsymbol{A}\left(\overline{\boldsymbol{x}_1\boldsymbol{x}_1^T} - \frac{\overline{\boldsymbol{x}_1\boldsymbol{x}_1}^T}{/\overline{1}}\right) - \left(\overline{\boldsymbol{x}_2\boldsymbol{x}_1^T} - \frac{\overline{\boldsymbol{x}_2\boldsymbol{x}_1}^T}{\overline{1}}\right) - \frac{\sigma^2}{2}\overline{1}\boldsymbol{A}^{-1} = \boldsymbol{O}. \quad (11)$$

Define

$\boldsymbol{P} = \left(\overline{\boldsymbol{x}_1\boldsymbol{x}_1^T} - \frac{\overline{\boldsymbol{x}_1\boldsymbol{x}_1}^T}{/\overline{1}}\right), \boldsymbol{Q} = \left(\overline{\boldsymbol{x}_2\boldsymbol{x}_1^T} - \frac{\overline{\boldsymbol{x}_2\boldsymbol{x}_1}^T}{\overline{1}}\right)$,
and $R = rI = \frac{\sigma^2}{2}\overline{1}I$. The equation is written as

$$\boldsymbol{A}\boldsymbol{P} - \boldsymbol{Q} - r\boldsymbol{A}^{-1} = \boldsymbol{O}. \quad (12)$$

To solve eq.(12), I used the Newton Raphson's method.

3.2 Successive iteration method for affine-invariant correlation determination

The successive iteration method provides the iterative procedure for optimal GAT determination and calculation of the affine-invariant correlation. It first calculates the inital value of $C_0 = C(f, g)$ between the original input and target images. Next determine the GAT components of $\boldsymbol{A}$ and $\boldsymbol{b}$, generate the transformed image $\mathbf{F}^*$, and substitute $\mathbf{F}^*$ into the input image $\mathbf{F}$. Next calculate the update value of $C_1 = C(f, g)$ between the renewed $\mathbf{F}$ and $\mathbf{G}$, and compare C_1 with C_0. If the correlation value increases, substitute C_1 into C_0, and repeat the process, otherwise, output the value as the GAT correlation.

4 Experiment

In the experiment, by using five photos of an object with gradually changed visual angles and matching with the previously taken reference image, we can evaluate the performance of the GAT correlation methods. Then I contrast the correlation values between the conventional GAT and the proposed edition. The correlation is indeed enhanced, however very limited.

The two GAT correlation methods have high accuracy than the original correlation. We can see the affine transformation is more completed in the proposed version.

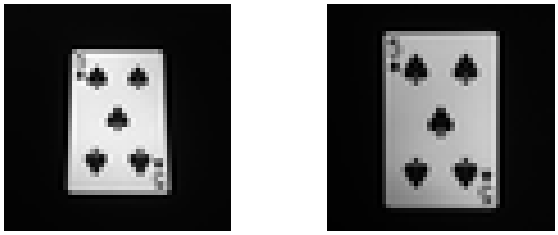

(a)Original (b)Target

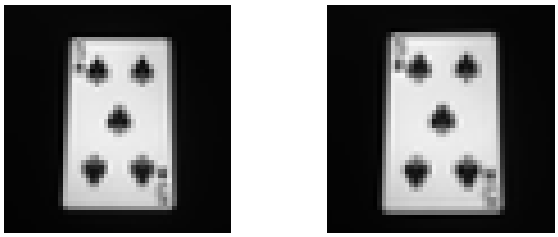

(c)GAT (d)proposed GAT

Figure 1: Images of experiment(Image no.: 3)

Table 1: Correlations

Image number	Original correlation	GAT correlation	
		Conventional	Proposed
1	0.863265	0.947115	0.969616
2	0.753867	0.931570	0.964143
3	0.701449	0.923636	0.953321
4	0.772810	0.899374	0.933814
5	0.783496	0.860661	0.905002

5 Conclusions

In this study, I conducted an experiment of template matching by using the conventionial and the proposed GAT correlation. By the proposed criterion, GAT correlation has been more accurately calculated. In the algorithm I stop the process when C_1 is smaller than C_0. However if continue the calculation, a higher value appeares sometimes. To get a more accurate correlation, we could use the maximal value among calculation results. Strong practicality might be considered in recognizing areas while the computation speed becomes higher. Also, in order to apply to perspective transformation, GAT and PPT are needed to be conbined.

References

[1] T.Wakahara, Y.Kimura, A Tomono, "Affine-Invariant Recognition of Gray-Scale Characters Using Global Affine Transformation Correlation," IEEE Transactions on pattern analysis and machine intelligence, Vol 23, No.4, pp.384-395, 2001.

[2] T.Wakahara, Y.Yamashita, "Acceleration of GAT correlation for distortion tolerant image matching," ICPR 2012, November, 11-15, pp.746-749, 2012.

Separation of Nitrogen Heterocyclic and Homocyclic Compounds Contained in Atmospheric Residue by Solvent Extraction

Student Number: 12B11555 Name: Akira HASEGAWA Supervisor: Ryuichi EGASHIRA, Hiroaki HABAKI

1. Introduction

The demand for heavy petroleum fractions have been shrinking recently, so that it is desired to convert these fractions into lighter fractions, for which the demands are relatively high. This conversion can be achieved by catalytic cracking [1]. Before this catalytic reaction, it is necessary and favorable to remove nitrogen heterocyclic compounds and polycyclic aromatic hydrocarbons in order to avoid catalytic poisoning etc. In this thesis, the solvent extraction using non-polar and polar solvent[2-6] was applied to the separation of the above compounds contained in the atmospheric residue, a petroleum heavy fraction obtained from the bottom of atmospheric distillation tower in the refinery.

2. Experimental

Table 1 shows the conditions of the extraction using non-polar solvent. The feed was atmospheric residue (AR), whose boiling range was 623 K~. Heptane etc. were used as non-polar solvents. After the feed and solvent were equilibrated under specified conditions, the liquid extract (solvent phase) and solid residue were separated from each other by filtration[2].

The conditions of the extraction by polar solvent are summarized in **Table 2**. The following mixtures were used as feeds: AR; the liquid extract from non-polar solvent extraction (Table 1) of AR (DAAR); heptane solution of vacuum gas oil (VGO) as a model for DAAR (MDAAR); etc. The VGO is the lighter fraction of two obtained from the vacuum distillation of AR, of which boiling range was 623~823 K. In some runs with polar solvent, the additive, such as, aluminum chloride, was used in the solvent in order to enhance the extraction [3]. After equilibration of feed and solvent phases, separatory funnel was used to separate the raffinate and extract.

The samples of the feed, extract, solid residue, and raffinate were analyzed by FT-ICR MS, chemical luminescence (JIS-K 2609), potentiometric titration. In FT-ICR MS analysis, more than ten thousands of heterocyclic and homocyclic compounds contained in AR or VGO were identified and quantified. The contents of total nitrogen and total basic nitrogen were determined by chemical luminescence and potentiometric titration, respectively.

3. Results and Discussions

The compositions of AR and VGO are given in **Table 3**. These heavy fractions mainly contained cyclic compounds and the contents of alkanes were quite low. The content of nitrogen compounds in AR was much higher than that in VGO. The content of nitrogen compounds with shorter side chain and more aromatic rings was higher.

A major part of AR dissolved in heptane, non-polar solvent to form the liquid extract, and the other small part remained as solid residue. The distribution ratio of component i, m'_i, in the non-polar solvent extraction was defined as,

$$m'_i = z_i / y'_i \quad (1)$$

where z_i was the mass fraction of component i in the solid residue ,and y'_i was that in the liquid extract. **Figure 1** shows the effects of the number of carbon atoms in side chain and that of aromatic rings on m'_i in the extraction of AR by heptane. The m'_i decreased, as the side chain lengthed and the number of aromatic rings decreased. There was not clear difference of m'_i between nitrogen heterocyclic and homocyclic compounds. However, since the nitrogen compounds contained in AR was those with shorter side chain and more aromatic rings as mentioned above, the content of the nitrogen compounds in total

Table 1 Experimental conditions in extraction by non-polar solvent

Feed	AR
Mass of feed	0.02 kg
Solvent	heptane etc.
Mass ratio of solvent to feed	5
Temperature	303 K
Time	48 h

Table 2 Experimental conditions in extraction by polar solvent

Feed	AR, DAAR*, MDAAR**, etc.
Mass of feed	0.13 ~ 0.24 kg
Solvent	aqueous solution of methanol
Additive to solvent	aluminum chloride etc.
Mass ratio of solvent to feed	1
Mass fraction of methanol	0.9
Mass fraction of additive	0, 0.027
Temperature	303 K
Time	48 h

* The extract from non-polar solvent extraction of AR.

** Heptane solution of VGO as a model for DAAR. The mass fraction of VGO in MDAAR was 0.33.

Table 3 Composition of AR and VGO (in mass fraction)

	heterocyclic compounds			homocyclic compounds
	N	NS	S	
AR	0.0332	0.048	0.556	0.3421
VGO	0.0072	0	0.4595	0.459

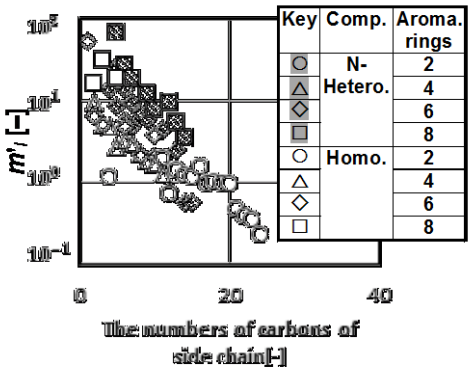

Fig. 1 m'_is of nitrogen heterocyclic and homocyclic compounds in AR extraction by heptane

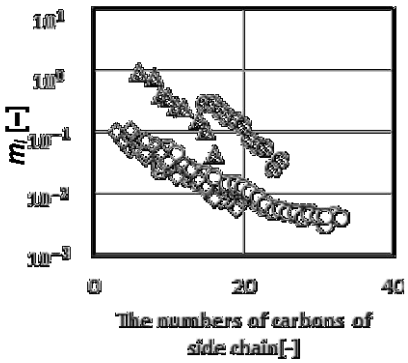

Fig. 2 m_is of nitrogen heterocyclic and homocyclic compounds in MDAAR extraction by aqueous solution of methanol

Table 4 Effect of aluminum chloride, $AlCl_3$, addition to polar solvent on m_i of total and basic nitrogens

	m_i [–]	
	without $AlCl_3$	with $AlCl_3$
Total nitrogen	0.4	0.4
Basic nitrogen	0.03	0.23

was reduced from 0.0813 in AR to 0.0796 (solvent free) in the liquid extract. The compounds with shorter side chain and more aromatic rings could be removed and the content of nitrogen compounds in total was lowered by non-polar solvent extraction of AR.

While it was difficult to conduct the direct extraction of AR by aqueous solution of methanol, polar solvent, in the range of this work, the extraction of DAAR, MDAAR, etc. could be carried out satisfactorily. The distribution ratio, m_i, was written as,

$$m_i = y_i / x_i \quad (2)$$

with the mass fraction in the extract, y_i, and that in the raffinate, x_i, in the polar solvent extraction. In **Figure 2**, the m_is are plotted against the number of carbon atoms in side chain with the various numbers of aromatic rings, where MDAAR was extracted by aqueous solution of methanol, polar solvent. The m_is decreased with number of carbon atoms in side chain. The effects of the number of aromtic rings on m_is were not obvious. The m_is of nitrogen heterocyclic compounds were larger than those of homocyclic compounds. The effects of aluminum chloride addition to the solvent on the m_is of total and basic nitrogens in the MDAAR extraction are shown in **Table 4**. The m_i of basic nitrogen with $AlCl_3$ in the solvent was higher than that without $AlCl_3$, while that of total nitrogen was not affected by $AlCl_3$ addition. The high affinity of aluminum ion with the lone pair of nitrogen atom in the basic nitrogen compound would enhance the dissolution of the nitrogen compound into aqueous solvent phase [3].

Based on the above experimental results, the following process was suggested. The AR is, first, extracted by non-polar solvent to remove nitrogen heterocyclic and homocyclic compounds with shorter chain and more aromatic rings as solid residue and to lower the nitogen compound content in the liquid extract to some extent. In the second, this liquid extract from the non-polar solvent extraction is extracted again by polar solvent to remove light nitrogen compounds. The raffinate after this polar solvent extraction mainly contains homocyclic compounds with longer side chain and less aromtic rings without nitrogen, which is an appropriate fraction for the downstream catalytic reaction.

4. Conclusions

The nitrogen heterocyclic and homocyclic compounds with shorter side chain and more aromatic rings contained in atmospheric residue could be removed and, thus, the total content of nitrogen compounds could be lowered by non-polar solvent extraction. The polar solvent could extract the nitrogen compounds selectively from the liquid extract obtained in the non-polar solvent extraction. According to these results, it was suggested to extract atmospheric residue with non-polar and polar solvents to provide an appropriate fraction for the downstream catalytic reaction operation.

Nomenclature

m_i = distribution ratio of i in polar solvent extraction, m'_i = distribution ratio of i in non-polar solvent extraction, x_i = mass fraction of i in raffinate phase in polar solvent extraction, y_i = mass fraction of i in extract phase in polar solvent extraction, y'_i = mass fraction of i in liquid extract in non-polar solvent extraction, z_i = mass fraction of i in solid residue in non-polar solvent extraction

<Subscripts>

i = component i

References

[1] 石油学会；石油精製プロセス，第五章，接触分解，pp.125-138

[2] Hasegawa, H.，東京工業大学2014年卒業論文

[3] Chris, S.，東京工業大学2000年度卒業論文

[4] Kodera, Y., et al., Fuel, 70, (6) 765 (1991)

[5] Nagai, M.，東京工業大学1999年卒業論文

[6] Masuda, T.，東京工業大学2015年度卒業論文

Scale-up the producing of functional compost and examine the disease suppressing effect

Student Number: 12_13940 Name: Takuya MITSUHASHI Supervisor: Kiyohiko NAKASAKI

1 Introduction

In recent years, many researches about the biological pesticide that prevent plant disease utilizing microorganisms instead of chemical pesticides were reported [1]. However, the steadily effective biological pesticide has not been produced yet. The failure of the production of biological pesticide is thought to be caused by a lack of nutrient source for the activity to suppress bacteria in the soil. If the disease suppressive microorganism grows in the compost, nutrient for the microorganism is fertilized simultaneously with biological pesticide to the soil. Therefore, the compost containing the disease suppressive microorganism is expected to be the effective biological pesticide. In this experiment, strain GM-21 [2] which can suppress bottom rot disease of pak-choi was used as the disease suppressive microorganism.

The objective of this study is to produce functional compost that can suppress the plant disease using oil cake as raw material.

2 Materials and methods

2-1 Mini scale production of functional compost

Functional compost was produced by the primary fermentation for the degradation of organic matter and the secondary fermentation for the propagation of strain GM-21.

The experimental system is the same as that in the previous paper [3]. The oil cake, sawdust and seeding material were mixed at a ratio of 15:4:1 on dry weight basis to create a raw composting mixture. At the start of primary fermentation, the pH level was adjusted to 8 by the addition of slaked lime, and the moisture content was adjusted to 50% by adding distilled water. Twelve grams of composting mixture was put into the reactor. Reactor itself was placed in an incubator to regulate the composting temperature. The temperature was raised from room temperature to a set point of 60^{o}C at a constant rate of 2.5^{o}C h^{-1}, and then, kept at the set point until 12 days. The exhausted gas from the composting reactor was introduced into a 10 L plastic bag for 24 hours and the total gas volume and the concentration of CO_2 is analysed. The conversion of carbon (Xc), corresponding to the degree of organic matter decomposition, was taken as a molar ration of the carbon loss as CO_2 to the decomposable carbon contained in the oil cake. Compost samples were recovered on day 0, 3, 6 and 12 in the primary fermentation and subjected to secondary fermentation. The values of pH of the composts were adjusted to 6 using 20% sulfuric acid. Strain GM-21 was inoculated with the initial DNA concentration of 10 ng g^{-1} DS and secondary fermentation was carried out for 5 days at 30^{o}C. The compost samples were withdrawn from the mini reactor at 0, 1, 3 and 5 days and subjected to physicochemical analyses, cell density of mesophilic bacteria and DNA concentration of strain GM-21 analyses.

2-2 Bench scale production of functional compost

Functional compost was produced using the bench-scale reactor. Raw compost mixture was same as mini scale production, but the temperature was left self-heating. Sterilized compost sample after the primary fermentation for 10 days was used for production of functional compost.

2-3 Assessment of the suppressive effect of functional compost

Plant growth assay was subjected to ascertain the disease suppressive effect of functional compost. Three test plots were subjected. Run A was without the inoculation of strain Pak-choi 2 as the pathogen; Run B was with the inoculation of only the pathogen; Run C was with the fertilization of the functional compost and inoculation of the pathogen. The mixture of the soil, compost and pathogen was put into polycarbonate pot and 15 surface-sterilized Pak-choi seeds were planted to the mixture in the pot. The pots were placed in a growth chamber and incubated at 25°C for 3 weeks with continuous illumination. The disease severity was rated on a scale from 1 to 5 by calculating a percentage of the number of diseased seedlings over the total number germinated 3 weeks after sowing. The soil samples were withdrawn from the pot at 0, 1, 2 and 3 weeks, and subjected to the measurement of DNA concentration of strain Pak-choi 2.

2-4 Real-time PCR

The concentrations of the DNA of strain GM-21 and Pak-choi 2 in the soil samples were evaluated by the real-time PCR method using the DNA extracted from the soil samples as a template. The primers specific to strain GM-21, 25F, 5’- gtgttgcatgtagctgcctcctc -3’ 52R,

5’- tgacgcgagagttatccagacctac -3’ , and specific to strain Pak-choi 2, ST-R1F, 5′- agtgttatgcttggttccact -3’, and ITS4(R), 5′- tcctccgcttattgatatgc -3’ were designed and used.

3 Results and discussion

3-1 Mini scale production of functional compost

The courses of concentration of strain GM-21 in the compost samples are shown in Fig. 1. When the conversion of carbon was too low (primary composting for 0 day) or high (primary composting for 12 days), strain GM-21 couldn’t grow in the compost. It was revealed that the optimum conversion of carbon for strain GM-21 to grow was around 75%.

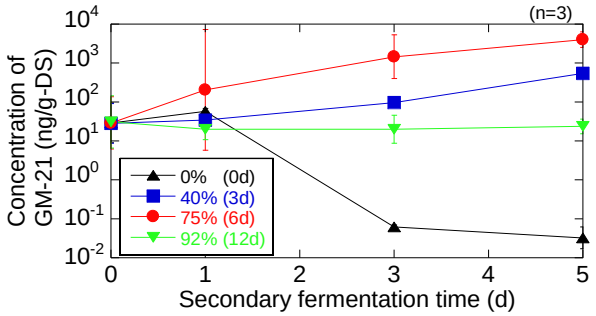

Fig. 1 Courses of concentration of strain GM-21 during the secondary fermentation.

3-2 Bench scale production of functional compost

The concentration of strain GM-21 in the compost samples is shown in Fig. 2. Strain GM-21 also could grow in bench scale composting.

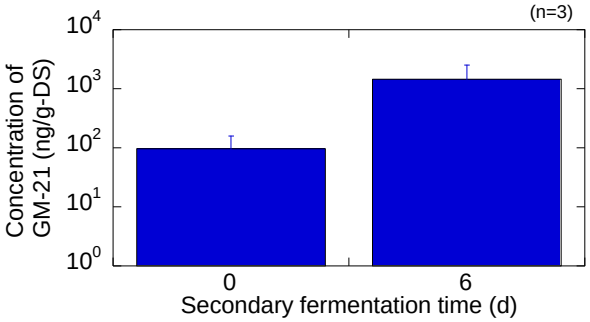

Fig. 2 The concentration of strain GM-21 in the compost samples.

3-3 Assessment of the suppressive effect of functional compost

Courses of disease severity during the plant growth assay are shown in Fig 3, Courses of concentration of strain Pak-choi 2 during the plant growth assay is shown in Fig. 4. In Run B, disease severity was almost 100% on 3 week after sowing and DNA concentration of strain Pak-choi 2 increased.

However in Run C, disease was significantly suppressed and DNA concentration of strain Pak-choi 2 didn’t increase.

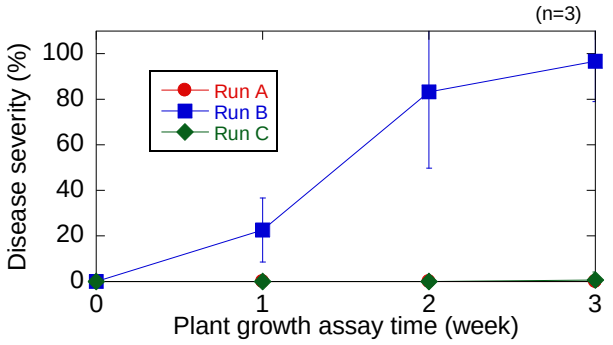

Fig. 3 Courses of disease severity during the plant growth assay.

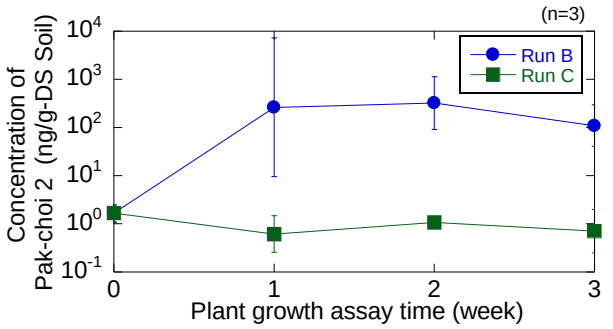

Fig. 4 Courses of concentration of strain Pak-choi 2 during the plant growth assay.

4 Conclusions

Optimal composting conditions for strain GM-21 were investigated. The bench scale production of functional compost succeeded. Plant growth assay was performed using the functional compost which was produced in this experiment and it was revealed that strain GM-21 could significantly suppress the pathogen.

References

[1] Seiber N. J, Coats J., Duke O. S., Gross D. A. 2014. Biopesticides: State of the art and future opportunities. *J. Agric. Food Chem*. 62: 11613−11619.

[2] Nakasaki K., Saito M., Suzuki N. 2007. Coprinellus curtus (Hitoyo-take) prevents diseases of vegetables caused by pathogenic fungi. *FEMS Microbiol. Lett*. 275: 286-291.

[3] Nakasaki K, Nagasaki K, Ariga O. 2004. Degradation of fats during thermophilic composting of organic waste. *Waste Manage Res* 22: 276-282.

Initial parameter setting in the propagation estimation based on EM/SAGE algorithm

Student ID : 12B14068 Author : Tokio MIYAKE
Supervisor : Prof. Jun-ichi TAKADA Asst.Prof. Kentaro SAITO

1 Introduction

Multiple-Input Multiple-Output (MIMO) transmission in the higher frequency band above 10 GHz is expected to be future mobile communication method. MIMO is the method to improve the capacity of network by using multiple transmitter and receiver antennas.

The performance of MIMO transmission in high frequency is strongly depends on the radio channel condition because of the fading and the scattering. Spatial Channel Model (SCM)[1] proposed by 3GPP has been widely used, and it is based on the ray-based channel model. This method needs propagation parameter. Space-Alternating Generalized Expectation (SAGE) algorithm[2] is one of the propagation parameter estimation method from the measurements.

This algorithm is iterative algorithm which is known that the accuracy heavily depends on the initial parameters. Successive Interference Cancellation (SIC) parameter estimation[3] is one of the initial parameter estimation method. This algorithm, however, has searching problem and can't estimate the propagation parameter on the specific condition (see subsection of related works). This paper propose new initialization method of SAGE algorithm by improving SIC parameter estimation using Single-Input, Multiple Output (SIMO) data.

2 Related works

2.1 Signal model and SAGE algorithm

In this paper, we define the received signal of MIMO transmission as frequency response. Assuming plane wave, we can introduce propagation path, which is identified by 9 parameters $\tau, \phi_T, \theta_T, \phi_R, \theta_R, \gamma_{HH}, \gamma_{HV}, \gamma_{VH}, \gamma_{VV}$. τ is the propagation time from the transmitter to the receiver, ϕ_T, θ_T is azimuth and elevation of Angle of Departure(AoD), ϕ_R, θ_R is azimuth and elevation of Angle of Arrival(AoA), and $\gamma_{HH}, \gamma_{HV}, \gamma_{VH}, \gamma_{VV}$ is polarized path weights. This paper ignore Doppler shift for simplicity and assume received signal as superposition of plane waves. The received signal $\boldsymbol{x}$ of L of plane wave is expressed in vector notation as

$$\boldsymbol{x} = \sum_{l=1}^{L} \boldsymbol{x}_l + \boldsymbol{n} = \sum_{l=1}^{L} \mathfrak{B}(\boldsymbol{\mu}_l) \cdot \boldsymbol{\gamma}_l + \boldsymbol{n} \qquad (1)$$

where $\boldsymbol{x}_l$ is received signal from l-th path, $\boldsymbol{n}$ is additive white Gaussian noise, $\boldsymbol{\mu}_l$ is vector notion of propagation parameter $\tau, \phi_T, \theta_T, \phi_R, \theta_R$ of l-th path, $\mathfrak{B}$ is angular frequency response of array antenna, and $\boldsymbol{\gamma}_l$ is polarized path weight $\gamma_{HH}, \gamma_{HV}, \gamma_{VH}, \gamma_{VV}$ of l-th path. Since $\boldsymbol{n}$ follows complex normal distribution, we can get likelihood function of $\boldsymbol{\mu}_l, \boldsymbol{\gamma}$. By simplifying of that likelihood function, we obtain next formula, which is called correlation function.

$$c(\boldsymbol{\mu}_l|\boldsymbol{x}_l) = {\boldsymbol{x}_l}^H \mathfrak{B}(\boldsymbol{\mu_l})(\mathfrak{B}(\boldsymbol{\mu_l})^H \mathfrak{B}(\boldsymbol{\mu_l}))^{-1} \mathfrak{B}(\boldsymbol{\mu_l})^H \boldsymbol{x}_l \qquad (2)$$

By maximizing this correlation function, we maximize likelihood of parameter and get l-th path propagation parameter. Eq. (2) can be used on the condition that $\boldsymbol{x}_l$ is known. SAGE algorithm estimates $\boldsymbol{x}_l$ by using initial propagation parameter.

2.2 SIC parameter estimation

Since SAGE algorithm is iterative algorithm, the initial parameter estimation of SAGE algorithm is important part. SIC parameter estimation is a algorithm which estimate initial parameter by maximizing correlation function. Since the parameter search is the 5-dimensional optimization problem, the calculation complexity becomes very large. Therefore, SIC parameter estimation divide this calculation into 4 steps for calculation reduction. Assuming l-th path estimation, we set temporary parameter to the propagation parameter of $(l-1)$-th path estimation result. By using this temporary propagation parameter, we estimate propagation parameter as shown below

$$\begin{aligned}
(a_1, a_2, a_3, a_4, a_5) &= (\hat{\tau}_{l-1}, \hat{\phi}_{T,l-1}, \hat{\theta}_{T,l-1}, \hat{\phi}_{R,l-1}, \hat{\theta}_{R,l-1}) \\
\hat{\tau}_l &= \arg\max_{\tau_l} \boldsymbol{c}(\hat{\tau}_l, a_2, a_3, a_4, a_5) \\
(\hat{\phi}_{T,l}, \hat{\theta}_{T,l}) &= \arg\max_{\phi_{T,l}, \theta_{T,l}} \boldsymbol{c}(\hat{\tau}_l, \phi_{T,l}, \theta_{T,l}, a_4, a_5) \\
(\hat{\phi}_{R,l}, \hat{\theta}_{R,l}) &= \arg\max_{\phi_{R,l}, \theta_{R,l}} \boldsymbol{c}(\hat{\tau}_l, \hat{\phi}_{T,l}, \hat{\theta}_{T,l}, \phi_{R,l}, \theta_{R,l})
\end{aligned} \qquad (3)$$

3 Proposed method

SIC-parameter estimation reduce the amount of calculation. However, SIC-parameter estimation uses temporary parameters which are unreliable. The

result of SIC parameter estimation is not accurate when the temporary parameter is different from true propagation parameter.

To solve the problem, in this paper, we proposed the SIMO(Single-Input, Multiple Output)-based initial parameter estimation method. In our proposal, MIMO channel matrix is decomposed into the set of SIMO channel matrices. Since SIMO channel matrices don't have Tx-side information, the dimension of parameter estimation problem is reduced from 5 to 3. The estimated SIMO parameters are then used as input to the correlation function. Then the remaining two parameters of correlation function are estimated.

4 Results

We evaluated our proposed method through simulations. The simulation data were generated by following table condition. The propagation parameter is generated to follow normal distribution.

Table 1: Simulation data condition

Number of path	10 path
Delay τ	$2.5 \leq \tau \leq 100$ ns
AoA azimuth ϕ_R	$0° \leq \phi_R \leq 359°$
AoA elevation θ_R	$30° \leq \theta_R \leq 150°$
AoD aimuth ϕ_T	$0° \leq \phi_T \leq 359°$
AoD elevation θ_T	$30° \leq \phi_T \leq 150°$
Path weight	$\gamma_{\mathrm{HH}}, \gamma_{\mathrm{HV}}, \gamma_{\mathrm{VH}}, \gamma_{\mathrm{VV}} = 1$
SNR	-10, 10, 30 dB
Center frequency	11 GHz
Bandwidth	400 MHz
Tx/Rx antenna array	12 elements Cylindrical Array

We conducted parameter estimation of 30 simulation data. We evaluate obtained result by using next error function P.

$$P = \frac{||\boldsymbol{x} - \boldsymbol{s}||^2}{||\boldsymbol{x}||^2} \tag{4}$$

where $\boldsymbol{x}$ is original simulation signal which doesn't include noise, and $\boldsymbol{s}$ is estimated signal. This error function evaluates the difference of estimated signal and original signal. The smaller value of the error function means the better estimation result. Fig.1, Fig.2 and Fig.3 show the result of 30 runs of SAGE results by using initial parameter estimation.

These results show that proposed method is better method in comparison with conventional method. We can also say that the result difference between the proposed method and conventional method become bigger when the SNR is bad. The conventional method can estimate propagation parameter when the SNR is large enough even if the temporary parameter is not correct. However, in the condition that SNR is bad and temporary parameter is not correct, conventional method lose correlation function peak and can't estimate propagation parameter. Proposed method is designed not to use temporary parameter. This result shows the validity of that idea.

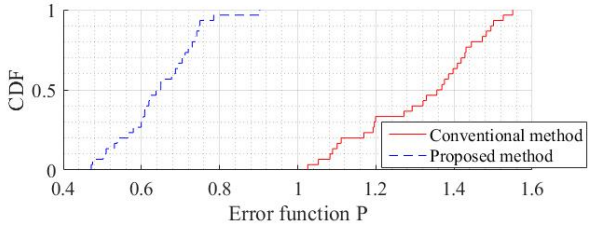

Figure 1: CDF plot of error function (SNR=-10 dB)

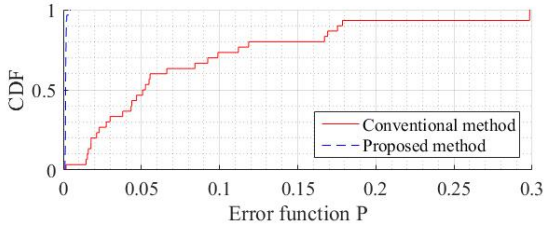

Figure 2: CDF plot of error function (SNR=10 dB)

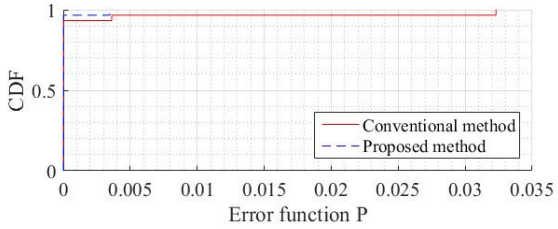

Figure 3: CDF plot of error function (SNR=30 dB)

5 Conclusion

In this paper, we propose new initial parameter estimation of SAGE algorithm. This paper shows proposed method improve accuracy of initial parameter estimation of simulation data in comparison with conventional algorithm. For future work, we will conduct propagation parameter estimation by using proposed method.

References

[1] v7.0.0 3GPP, TR 25.996. Spatial channel model for multiple input multiple output(mimo) simulations (release 9), 2009.

[2] Jeffrey A Fessler and Alfred O Hero. Space-alternating generalized expectation-maximization algorithm. *Signal Processing, IEEE Transactions on*, 42(10):2664–2677, 1994.

[3] V. H. Pham. Radio channel parameter estimation using sage algorithm. Master's thesis, Tokyo institute of technology, 2014.

全球高解像度人工排熱データベースの構築

学籍番号: 12_10001　氏名：トウゲツ　指導教官：神田学

1. はじめに

都市化の拡大に伴い、ヒートアイランド現象が顕著となる。その形成要因の一つとして、人間活動に伴うエネルギー消費による排熱、即ち、人工排熱(Anthropogenic Heat Emissions, AHE)が挙げられる。人工排熱は都市部の気温変化のみではなく、局地豪雨を促進，大気境界層高度を上昇させるなど、気候・気象面での影響が指摘されている。特に、AHE の影響で夏季の気温が上昇すると、冷房によるエネルギー消費が増加し、更に多くの熱量が排出されるというフィードバック機構も指摘されている。

AHE の時空間分布の推定について、既往研究ではボトムアップとトップダウンの二種類の手法がある。前者は現地調査を通じ、詳細な地理情報と局地的なエネルギー統計値を用いて AHE を定量化する手法である。しかし、このようなデータは現地で個別に収集する必要があり、広域又は全球について同様の手法を適用することは困難である。それに対し、後者は国ごとの年間エネルギー総量をより細かい時空間解像度へ配分させる手法である。この手法はグローバルに展開できる一方で、解像度と精度の制限が問題となる。本研究は広域への適用可能性を前提として、高解像度且つより正確に都市のエネルギー消費の分布を再現できるトップダウン手法を開発し、全球の人工排熱データベース(空間解像度:30 arc-seconds, 時間解像度:1hour)を構築することを目的とする。

2. 人口排熱時空間分布の推定

本研究では、国別の一次エネルギー消費量が最終的に全て熱フラックスとして排出されると仮定し、年間エネルギー消費から地域別(空間分布)の年平均 AHE を算出する。また、年平均から月変化と日変化（時間分布）を推定する。グローバルなエネルギー統計データは U.S.Energy Information Administration (EIA)および International Energy Agency (IEA)から得られた。人口データは LandScan Global 2013 Population Database を使用した。

各グリッドにおける年平均 AHE(Q_{f-y})は、エネルギーロス（一次エネルギーと最終エネルギーの差）の排熱(Q_L)、産業・農業部門の排熱(Q_{IA})、商業・家庭・運輸部門の排熱(Q_{CRT})、人間代謝熱(Q_M)という四つの成分に分けて求めた。Q_Lはエネルギーロスを国全域に、Q_{IA}はその部門のエネルギーを居住人口のある地域に、一様に配分して計算した。Q_{CRT}について、既往研究では人口密度分布によって配分する手法が一般的であるが、通常の居住人口と昼間の都市人口には大きな隔たりが存在するため、都市部の排熱を正確に把握できない。そこで、夜間の経済活動やエネルギー消費をよく表現できる、NOAA のナイトライトデータで人口密度を補正する手法を提案した。ナイトライトと人口密度の相関に着目すると、両者の線形関係から逸脱したグリッドは昼夜の人口差が著しく大きいオフィス街と住宅地となる。ナイトライトと人口密度の線形関係に基づき、外れ値の人口データを補正した。補正後の人口データを用いて、商業部門など都市の活動と密接に関連しているエネルギー消費量を配分して Q_{CRT} を求めた。Q_M については、Sailor *et al.*(2015)が提案した代謝率を用いて、LandScan の人口密度によって算出した。

年平均から月平均を求めるために、AHE に関する気温感応度を提案した。平成 15 年環境庁の調査および米国の AHE データセット(Sailor *et al*,2015)を見ると、都市別の月平均 AHE は、おおよそ20℃を境にして(分岐気温点)V 字型となる傾向が示されている。各都市のプロットに対して、回帰直線の傾きを用いて、年間平均の AHE に対する気温が分岐気温点より 1℃上昇または低下による増分の比率、即ち気温感応度(%/℃)を算出した。これらを元に AHE の気候感応度に関する経験式を見積もり、グローバルに一般

化させることで、AHE の月変化を求めた。一方日変化については、東京二十三区の AHE データセット(Moriwaki *et al.*, 2008)を参照すると、月平均気温に対応した四つのパターンがあることが分かり、それに基づき一日の時間別 AHE を見積もった。

3. 全球人口排熱のデータベースおよびバリデーション

前述のトップダウン手法を用いて全球の人口排熱データベース(2013)を構築した(図 1)。グローバル平均の AHE が 0.13 W/m^2であり、いくつかの大都市では AHE の値が 100 W/m^2 以上となった。最高値は 493 W/m^2 (香港)である。時間変化に関して、12 月から 2 月までの期間は年間を通して最も大きい人工排熱がなされる時期となった。都市に注目すると(図 2、東京の例)、ナイトライトで補正した結果、都市中心部と周囲の住宅地区の空間的偏差がよく表現されている。

本研究の結果を、既存の地域スケールのデータセット(ボトムアップ手法)およびグローバルスケールのデータセット(LUCY model、トップダウン手法)と比較し、東京、ロンドンと米国 52 大都市について検証を行った。空間と時間の両方において、LUCY model よりボトムアップ手法で再現したデータと一致する傾向となった。特に、気候感応度による補正を適用することで、ボトムアップ手法で解析したローカル AHE の月変化を LUCY model より精確に再現できた。その一方で、ナイトライトによる補正は東京では顕著であったが、ロンドンでは同様の補正効果は得られなかった。その原因として、ナイトライトの感度は地域差があるため、グローバルに展開する際には、ナイトライトの感度に関するパラメータを都市ごとに考慮すべきである。

4. おわりに

本研究では、グローバルなエネルギー統計データと衛星画像を用いて、全球人口排熱の時空間分布を推定するトップダウン手法を開発した。ナイトライトによる人口密度の補正と、都市別の気候感応度を導入することで、都市の排熱分布および時間変化が大幅に改善した。これにより高空間解像度のグローバルな AHE データベースを構築することができた。本研究成果を気象シミュレーションの境界条件として応用することで、人工活動が気候に及ぼす影響について検討することが今後可能となる。

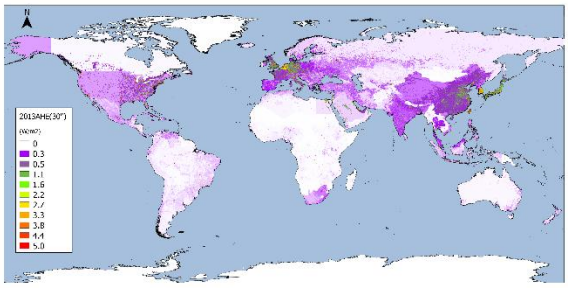

図 1 全球における年平均 AHE の空間分布図

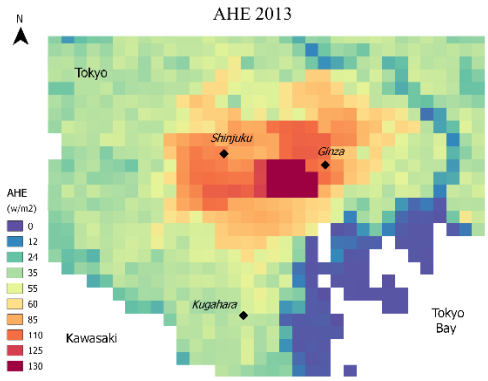

図 2 東京 23 区における AHE の空間分布図

参考文献

[1] 平成 15 年度 都市における人工排熱抑制によるヒートアイランド対策調査 (国交省・東京都・環境省) http://www." *env. go. jp/air/report/h16-05/index. html* (15).

[2] Sailor, D.J., Georgescu, M., Milne, J.M. and Hart, M.A. (2015) 'Development of a national anthropogenic heating database with an extrapolation for international cities', *Atmospheric Environment*, 118, pp. 7–18. doi: 10.1016/j.atmosenv.2015.07.016.

[3] Moriwaki, R., Kanda, M., Senoo, H., Hagishima, A. and Kinouchi, T. (2008) 'Anthropogenic water vapor emissions in Tokyo', *Water Resources Research*, 44(11), p. n/a–n/a. doi: 10.1029/2007wr006624.

Feasible study of Space debris removal by using electromagnetic force

Student number: 12-13904 Name: Jun Mitani Supervisor: Daisuke Akita

1, Introduction

Space debris is trash in orbit. As a result of space activity, a large number of space debris is left in orbit around the earth. We can observe and track big debris. And can protect satellite from small debris collisions with shield. But for 1cm to 10cm debris, we cannot observe them, and cannot protect the satellites from their collisions. The feasible solution for the space debris has not been found out yet.

Table 1 shows the number of space debris by its size.

Table 1: Number of space debris[1]

Size	~1cm	1cm~10cm	>10cm
Total Numbers	0.15 billions	0.65 millions	22 thousands
Numbers under 2,000km Alt	1.6 millions	0.27 millions	14 thousands
Shield	○	×	×
Observation	×	×	○

2, Mission concept

Figure 1 shows the mission concept

1. A satellite is launched to an orbit of 400km Altitude.
2. The satellite produces a magnetic field around its own self.
3. Space debris fly by the satellite with relative orbit velocity.
4. Electromagnetic induction induces a current inside the debris.
5. The debris is declare by a Lorentz force of the induced current and the magnetic field.
6. The decelerated debris re-enter the Earth's atmosphere and finally burn up.

This study investigates the followings.

1. Required Δ V for debris to re-enter the atmosphere.
2. Model of a induced current inside a debris and a Lorentz force acting on it.

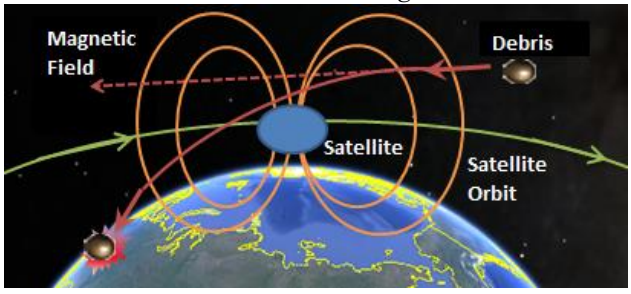

Figure [1] :Mission concept

3, Required deceleration for debris

Forces on the space debris are modeled as shown in Fig 2.Equations of motion are written as below.

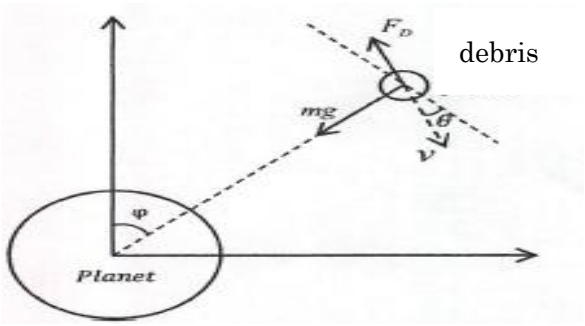

Figure [2]:Calculation model during atmosphere entry

$$\frac{dv}{dt} = -\frac{C_D S}{2m}\rho v^2 + g\sin\theta \qquad (1)$$

$$v\frac{d\theta}{dt} = \left(g - \frac{v^2}{r}\right)\cos\theta \qquad (2)$$

θ :Flight path angle C_D: Drag coefficient.
r:Distance from the center of the Earth.
ρ:Atmosphere density. m:Mass.
S:Frontal area.

The time to remove a space debris at 400km altitude is shown in Fig 3.At least 60 m/s is the needed to remove the debris in a reasonable time.

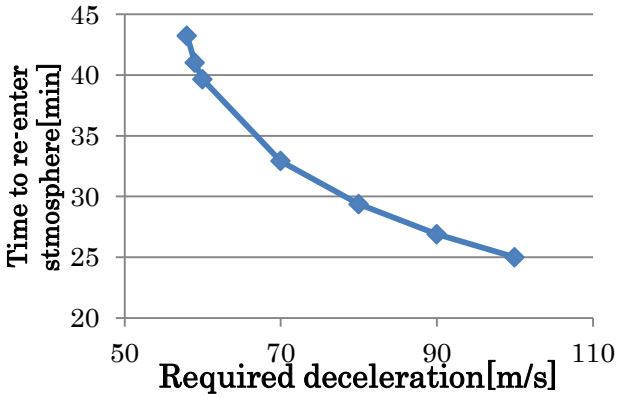

Figure [3]:Time to remove space debris vs. Δv

4, Lorentz force on debris

In Maxwell equations, the charge density inside a debris is assumed to be zero. For the conductive material as below.

$$\nabla \cdot \vec{E} = 0 \qquad (3)$$

Introducing a vector potential $\vec{A}$ of $\vec{E}$, we can write [3].

$$\vec{E} = \nabla \times \vec{A} \qquad (4)$$

Using equation(4) and Faraday's law, we can calculate an induced electro field by numerically solving.

$$\nabla^2 \vec{A} = \frac{\partial \vec{B}}{\partial t} \qquad (5)$$

Equation (5) is solved by SOR method, An induced current is calculated using

$$\vec{J} = \sigma \vec{E} \qquad (6)$$

Finally, A Lorentz force $\vec{F}$ is obtained by.

$$\vec{F} = \vec{J} \times \vec{B} \qquad (7)$$

E: Electro field B: Magnetic flux density
ϵ_0: Dielectric constant of vacuum
ρ: Charge density σ :Electric conductivity
$\mathcal{J}$: Current density F:Lorentz force

I simulated a situation shown in Fig 4.Space debris go through a magnetic flux density field that produced with a magnet. The velocity of space debris is 10km/s.

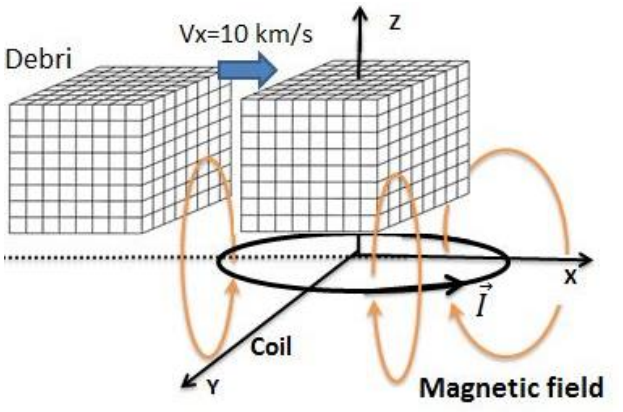

Figure [4] :Space debris goes through B field

The indeed current distribution inside the space debris is shown in Fig[5].

The current flows to counteract the change of magnetic field inside the debris. Integrating the current density, we could obtain a Lorentz force that decelarates the soace debris.

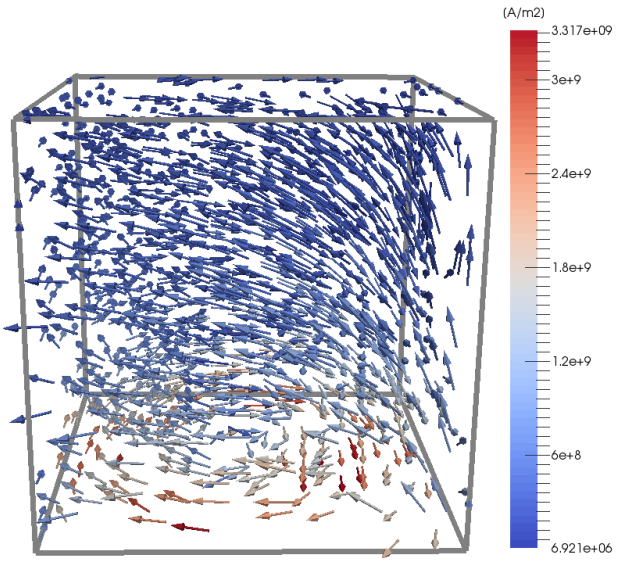

Figure[5]:Induced current dencity distribution

Fig[6] shows the vector of decelation in the whole motion. I confirm the induced Lourentz force always decelarates debris. Furthermore, I confirm the induced Lourentz force is three–demensional power.

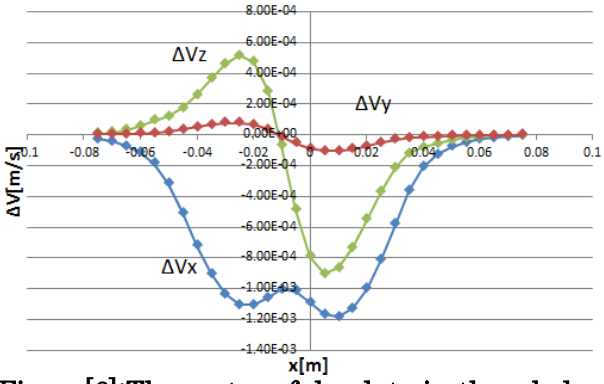

Figure[6]:The vector of decelate in the whole motion

4, Conclusion

This study showed an artifical magnetic field can decelerate the space debris, in orbit. However, we have to investigate the optimal magnetic field distribution. To obtain a sufficient deceleration for the space debris removal.

References

[1]He Ping," Feasibility on Removal of Space Debris by an Artificial Magnetic Field," p6 ,2009

[2]SeiyaFuruki "Titan Aero capture for Saturn Orbit Insertion," p14 ,2011

[3]Kenzo Miya "Analysis Electromagnetism and Electromagnetic structure," YOKENDO, pp,179-199,1995

Effect of microbial pretreatment for oil in methane fermentation from wastewater containing soybean oil

Student Number: 12-13229 Name:Takuya MAEKAWA Supervisor: Kiyohiko NAKASAKI

1. Introduction

Fat is one of the major organic matters in wastewater from food processing factory. Fat can be a good substrate for methane fermentation as in theoretical value, 850 mL of methane gas can be produced from 1 g of fat, even though 500 mL of methane gas can be produced from 1 g of protein, and 395 mL of methane gas can be produced from 1 g of carbohydrate [1]. So methane fermentation of wastewater containing fat is desired.

However, fat contained in the wastewater is usually separated and discarded as the industrial waste before the biological treatment stage because it is known that the production of the methane from fat is difficult. Fat is separated from aqueous phase and is hardly biodegradable. To solve the problems, oil is generally hydrolyzed by reagent of acid-base solution or enzyme. But there is few research of methane fermentation from pretreated oil by microorganism producing surfactant.

In this study, pretreatment of the soybean oil by the microorganism was applied in the methane production from the wastewater containing fat and the effectiveness of the pretreatment depending on the amount of oil was investigated by the methane fermentation using soybean oil.

2. Materials and methods

An yeast strain, *Pseudozyma rugulosa* NBRC 10877 was used to pretreat the soybean oil. *P. rugulosa* was known as a producer of a surfactant, MEL [2]. MEL has no toxic effect on microorganism [3]. The yeast was precultivated in 20 mL of YM broth at 25 ºC for 2 days 150 spm. After the cultivation, 1 mL of the preculture was centrifuged and the yeast was rinsed with Yeast oil broth that was composed of 20 g/L of soybean oil, 3 g/L of yeast extract and inorganic nutrients. Then, 50 µL of Yeast oil broth containing the yeast was inoculated to 10 mL of Yeast oil broth and cultivated at 25ºC for 7 days. After 7 days cultivation, the culture was supplied to methane fermentation.

Glucose, sodium acetate, lactic acid (GAL) and soybean oil were used as substrates for methane fermentation and two experiments, Run A and Run B were conducted. In Run A, the reactor was fed with untreated Yeast oil broth, and in Run B, the reactor was fed with Yeast oil broth pretreated by yeast. Three kinds of the substrate with different mixing ratio of Yeast oil broth, glucose, sodium acetate and lactic acid, designated as O-0, O-25 and O-50, were prepared. But amount of carbon of O-0, O-25, O-50 were same. The compositions of those substrates are shown in Table 1. Those substrates were supplied to each reactor in a stepwise manner: day 0-20 with O-0, 21-95 with O-25 and day 96-232 with O-50.

For the startup of the experiment, 1545 mL of distilled water, 200 mL of O-0 and 65 g of granular sludge from food processing factory that had been already acclimated with O-0 were mixed in two of the anaerobic sequencing batch reactor (ASBR). These reactors were made of Pyrex glass and had a working capacity of 2.5 L. These reactors were flushed with 5 L of N_2. The temperature in the reactors was maintained at 39 ºC by water jacket, and the solution in the reactors was agitated with a stirrer at 100 rpm. In these experiments, 200 mL of supernatant was extracted from the reactor, and the same volume of fresh substrate was fed every day.

The value of pH was measured by the pH meter. A sample of the exhaust gas was captured into a sampling bag and gas compositions were measured by GC-TCD. Gas volume was measured using dry test gas meter. The concentration of GAL and organic acids in culture of Run A and Run B during day 0-20 was measured by HPLC.

	O-0	O-25	O-50
Glucose (g/L)	12.5	9.38	6.25
Sodium acetate (g/L)	6.25	4.69	3.13
Lactic acid (g/L)	6.25	4.69	3.13
Soybean oil contained in the substrate (g/L)	0	3.05	6.1

Table 1 Composition of the O-0, O-25 and O-50

3. Results and discussion

The pH value of Run U and Run P is around optimum value, 6.3-7.4, for whole period of methane fermentation.

Fig. 1 shows the courses of gas volume of CH_4 and CO_2 in the fermentation of Run A and Run B. During day 1 to 20 of fermentation the gas productions of both Runs were stable at around 1.07 L. As was not shown here, GAL and organic acid were not detected and were considered to be completely degraded.

After changing the substrate to O-25 at day 20, the gas volume of Run B during day 21 to 95 was almost the same volume with that before day 21. This result indicated that pretreated oil could be completely degraded and converted to CH_4 and CO_2 since in total amount of carbon in the substrates of O-0 and O-25 were the same. By contrast, the gas volume of Run A decreased to around 0.80 L at day 21.

The results suggest that immediately after the oil was supplied, oil was not available for microorganisms. Then, the gas volume of Run A gradually increased from day 24 and reached at around 1.09 L on day 74 that is almost the same volume with that observed before day 21. It is considered that during day 24 to 74, some microorganisms were acclimated to utilize oil in the O-25.

After changing the substrate to O-50 at day 95, the gas volume of Run A and Run B decreased to around 0.65 L. After the pretreatment, O-50 was considered to contain higher amount of long chain fatty acid (LCFA) that was produced in the degradation of fat than that in O-25. It is known that more than 0.1 g/L of oleic acid causes the inhibition against microorganisms [4]. When the oil in the O-50 is completely degraded, concentration of oleic acid produced from is estimated at 0.15 g/L that is higher than the concentration of 0.1 g/L causing inhibition of microbial activity, and it is considered that LCFA produced in the degradation of oil in O-50 caused the decrease of the gas production of Run A and Run B.

Around day 155, the gas volume of Run A and Run B gradually increased and reached to 1.09 L on day 175 that is almost the same volume observed before day 21.This result suggests that some microorganisms have been acclimated to high concentration of LCFA and could degrade LCFA.

Fig.2 shows the DGGE pattern for bacteria in the methane fermentation process of bacteria of Run A and Run B. There were some characteristic bands, band 1-7 in Fig.2. Among those bands, only the DNA sequence of Band 5 could be determined. Light intensity of band 5 and band 6 of increased in the period of day 155-232 which coincided with the increase in the methane production in Run A and B. DNA sequence of band 5 was close to that of *Segniliparus rotundus*. The results indicated that *Segniliparus rotundus* could degrade LCFA.

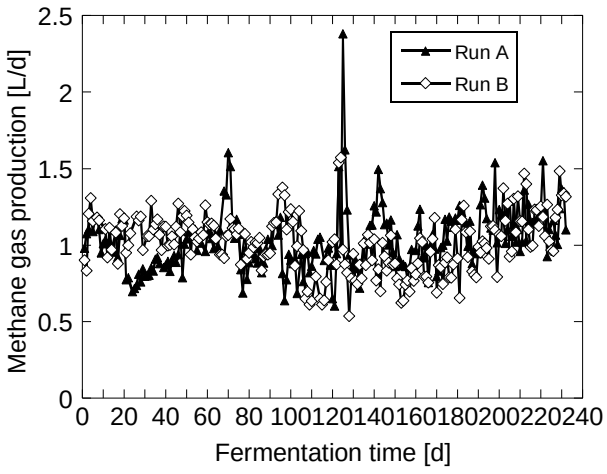

Fig. 1 Courses of CH_4 gas production of Run A and Run B

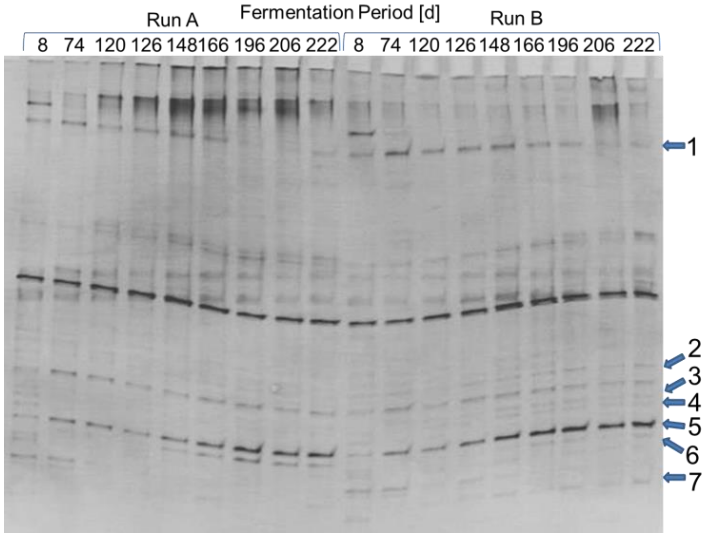

Fig. 2 DGGE pattern for bacteria of Run A and Run B

4. Conclusions

It was revealed that the microbial pretreatment of oil could keep the organic matter degradation in methane fermentation from wastewater containing oil at the oil content of 3.05 g/L and when the content of oil was set at 6.10 g/L, it was suggested that the pretreatment was not sufficient for the methane production.

Gas volume of Run A and Run B was recovered in the late stage of fermentation and a bacteria, *Segniliparus rotundus*, was identified as the candidate of LCFA degrading bacteria. The possibility of enhancement in the methane production from high content of oil by employing *Segniliparus rotundus* was suggested in this study.

Reference

[1] Noaki. Kataoka et al. : Studies on a Methane Fermentation Process for Treating Oil and Fat Containing Food-processing Wastewater, Ebara engineering review, 212, 3-9 (2006).

[2] Tomotake Morita, Masaaki Konishi, Tokuma Fukuoka, Tomohiro Imura, Dai Kitamoto, Discovery of Pseudozyma rugulosa NBRC 10877 as a novel producer of the glycolipid biosurfactants,mannosylerythritol lipids, based on rDNA sequence, Appl Microbiol Biotechnol, 73, 305–313, (2006)

[3] 福岡　徳馬, 森田　友岳, 井村　知弘, 北本　大, 酵母が作り出す高機能界面活性剤（バイオサーファクタント）の開発, 化学と工業, 83, 103-110, (2009)

[4] Irini Angelidaki et al. : Effects of free long-chain fatty acids on thermophilic anaerobic digestion, Appl Microbial Biotechnol, 37, 808-812 (1992).

大域的射影変換相関法を用いたテンプレートマッチング

学籍番号：12_09653　学生氏名：趙偉成　指導教員：山下幸彦

1　はじめに

テンプレートマッチングとは，テンプレートと呼ばれるパターンが，テスト画像全体の中に存在するかどうかを調べるコンピュータビジョンの一手法である。この技術は対象物体の位置検出，部品の位置決め等広い分野で応用されている。テンプレートマッチングの基本原理は画素どうしの比較によって，類似度が一番高い位置を見つけることである。類似度としては，正規化相互相関 (NCC)，輝度差の二乗和 (SSD) または輝度差の絶対値和 (SAD) が代表的である。そのうち，正規化相互相関法には照明変動など外乱に対する耐性が高いという利点がある。しかし，それらの手法にはアフィン変換や射影変換による影響を受けやすいという問題がある。

そのため，画像の線形変換や平行移動に頑張な大域的アフィン変換 (GAT) 相関法 [1,2,3] や射影変換に拡張した大域的射影変換 (GPT) 相関法 [4] が提案された。しかしながら，今までの GAT/GPT の実験では入力画像とテンプレート画像の画像サイズが同じ場合だけで実験が行われていた。本論文では入力画像が大きくその中からテンプレートを効率的に探し出すアルゴリズムを提案し，実験を行う。

2　GAT 相関法

2 次元画像のファフィン変換は次式で与えられる。

$$\boldsymbol{x}' = \boldsymbol{A}\boldsymbol{x} + \boldsymbol{b} \tag{1}$$

ここで，$\boldsymbol{x}$ は 2 次元座標を表す 2 次元ベクトルであり，$\boldsymbol{x}'$ はアフィン変換されたベクトルである。$\boldsymbol{A}$ と $\boldsymbol{b}$ はアフィン変換を表す $(2,2)$-行列と 2 次元ベクトルである。定義域が D である画像 $f(\boldsymbol{x})$ に対し，式 (1) のアフィン変換で変換した画像を $f'(\boldsymbol{x})$ とおけば，

$$f'(x) = \frac{1}{|\boldsymbol{A}|} f(\boldsymbol{A}^{-1}(\boldsymbol{x} - \boldsymbol{b})) \tag{2}$$

が成立する。その時，2 つの画像 $f(\boldsymbol{x})$ と $g(\boldsymbol{x})$ の GAT 相関値は次式の目的関数を $\boldsymbol{A}$, $\boldsymbol{b}$ を変化させた時の最大値で定義される。

$$J_{GAT} = \int_D f'(\boldsymbol{x}) g(\boldsymbol{x}) d\boldsymbol{x} \tag{3}$$

式 (3) では，未知成分 $\boldsymbol{A}$, $\boldsymbol{b}$ が画像の中にあり，計算することが難しい、そのため，2 次元ガウス関数

$$G(\mathbf{x}) = \sqrt{\gamma} e^{-\gamma \|\boldsymbol{x}\|^2} \tag{4}$$

による近似と，エッジ方向の同一性を導入し，次の目的関数を定義する。

$$\begin{aligned} \tilde{J}_{GAT} \quad = \quad & \int_D \int_D G(A\boldsymbol{x}_1 + \boldsymbol{b} - \boldsymbol{x}_2) \\ & \delta(\nabla f(\boldsymbol{x}_1), \nabla g(\boldsymbol{x}_2)) f'(\boldsymbol{x}_1) g(\boldsymbol{x}_2) d\boldsymbol{x}_1 d\boldsymbol{x}_2 \end{aligned} \tag{5}$$

ここで，$\delta(\nabla f(\boldsymbol{x}_1), \nabla g(\boldsymbol{x}_2))$ はクロネッカーデルタであり，2 つの画像の勾配ベクトルが同方向である場合に 1，異なる場合に 0 となる。

GAT 相関法では，$\boldsymbol{A}$ と $\boldsymbol{b}$ に対する $\tilde{J}_{GAT}$ の微分が 0 となる時に最大値を取る。その条件から得られる方程式を近似的に解いて $\boldsymbol{A}$ と $\boldsymbol{b}$ の値を得る。この計算で得られたアフィン変換で入力画像を更新して，この操作を相関が最大になるまで繰り返す。

3　GPT 相関法

2 次元画像の射影変換は次式のように与えられる。

$$\boldsymbol{x}' = \frac{\boldsymbol{A}\boldsymbol{x} + \boldsymbol{b}}{1 + \langle \boldsymbol{c}, \boldsymbol{x} \rangle} \tag{6}$$

ここで，$\boldsymbol{x}$ は 2 次元座標を表す 2 次元ベクトルであり，$\boldsymbol{x}'$ は射影変換されたベクトルである。また，2 次元画像の部分射影変換 (PPT) を次式で定義する。

$$\boldsymbol{x}' = \frac{\boldsymbol{x}}{1 + \langle \boldsymbol{c}, \boldsymbol{x} \rangle} \tag{7}$$

上式により，射影変換はアフィン変換と部分射影変換の組み合わせで表すことができることがわかる。したがって，GPT 相関法を部分射影変換 (PPT) とアフィン変換 (AT) の 2 つの部分に分けて計算する。部分射影変換での目的関数を次式で定義する。

$$\begin{aligned} J_{PPT} \quad = \quad & \int_D \int_D G\left(\frac{\boldsymbol{x}_1}{1 + \langle \boldsymbol{c}, \boldsymbol{x}_1 \rangle} - \boldsymbol{x}_2 \right) \\ & \delta(\nabla f(\boldsymbol{x}_1), \nabla g(\boldsymbol{x}_2)) f'(\boldsymbol{x}) g(\boldsymbol{x}) d\boldsymbol{x}_1 d\boldsymbol{x}_2 \end{aligned} \tag{8}$$

これを最大にする $\boldsymbol{c}$ を 1 次近似を用いて求める。アフィン変換と部分射影変換を交互に計算し，入力画像を変形させたものを新しい入力画像として，相関値が収束するまで繰り返す。最後に得た最大の相関値を GPT 相関と定義する。

4 GPT 相関法によるテンプレートマッチング

本論文で提案するアルゴリズムは，テスト画像の各位置で抽出した画像の類似性を評価して，閾値を超えた位置で GPT 相関法を適用し，GPT 相関が最大になる位置を検出することである。第m回目の繰り返しにおいて，射影変換 $\boldsymbol{A}_m$，$\boldsymbol{b}_m$，$\boldsymbol{c}_m$ を用いて入力画像からテンプレート画像と同じ大きさの画像を切り出す。次に，線形方程式を解いて $\boldsymbol{A}'$，$\boldsymbol{b}'$，$\boldsymbol{c}'$ を計算する。そして，新しい射影変換 $\boldsymbol{A}_{m+1}$，$\boldsymbol{b}_{m+1}$，$\boldsymbol{c}_{m+1}$ を次式で計算する。

$$\boldsymbol{A}_{m+1} = \boldsymbol{A}'\boldsymbol{A}_m + \boldsymbol{b}'\boldsymbol{c}_m^{\mathrm{T}} \quad (9)$$

$$\boldsymbol{b}_{m+1} = \boldsymbol{A}'\boldsymbol{b}_m + \boldsymbol{b}' \quad (10)$$

$$\boldsymbol{c}_{m+1} = \boldsymbol{A}_m^{\mathrm{T}}\boldsymbol{c}' + \boldsymbol{c}_m \quad (11)$$

この変換により画像を切り出し，相関値が最大になるまで線形方程式を解くことと変形を繰り返す。

5 実験結果

本論文では，大域的射影変換 (GPT) 相関法で射影変換やアフィン変換により変形したテスト画像の中で，参照画像の位置を検出する実験を行った。そして，GPT 相関法の結果と正規化相互相関法の結果を比較して考察した。表 1 に最大正規化相互相関値，GPT 相関法で検出された位置の初期相関値，検出された位置の GPT 相関値を示す。図 1 は $\boldsymbol{c} = (0, 0.005)$ の射影変換と 30° せん断変換で変形したテスト画像である。図 2 はそれぞれテンプレート画像，輝度差の二乗和 (SSD) による検出位置の画像，輝度差の絶対値和 (SAD) による検出位置の画像，正規化相互相関法による検出位置の画像，GPT 相関法による検出位置の画像，GPT 変換した後の画像である。

表 1 及び図 2 により，GPT 相関法はアフィン変換や射影変換に対する耐性を持ち，正規化相互相関法より相関値の高い画像位置を検出でき，GPT 相関値が 0.9 以上に向上したことがわかった。

6 おわりに

本論文では，GPT 相関法をテンプレートマッチングに適用することを提案し，その有効性を計算機実験によって確認した。今後の課題は，計算精度の向上と，計算速度を上げることである。

表 1: 正規化相互相関及び GPT 相関法による相関値

	正規化相互相関	Org	GPT 相関
縦 1.3 倍拡大	0.772618	0.772618	0.997546
縦 1.1 倍拡大	0.799914	0.450031	0.997078
縦 0.8 倍縮小	0.739234	0.291620	0.993366
縦 0.5 倍縮小	0.535498	0.478905	0.985412
10° 回転	0.669099	0.548039	0.993027
20° 回転	0.547836	0.499562	0.990889
30° 回転	0.467166	0.368555	0.957391
10° せん断	0.641445	0.555850	0.996402
20° せん断	0.660606	0.581996	0.996544
30° せん断	0.583002	0.555452	0.922667
$\boldsymbol{c} = (0.003, 0)$ 射影変換	0.576191	0.544649	0.990156
$\boldsymbol{c} = (0.005, 0)$ 射影変換	0.445867	0.445867	0.988551
$\boldsymbol{c} = (0, 0.003)$ 射影変換	0.583002	0.515562	0.995552
$\boldsymbol{c} = (0, 0.005)$ 射影変換	0.639396	0.478628	0.990321
射影変換とせん断	0.492940	0.282011	0.913418

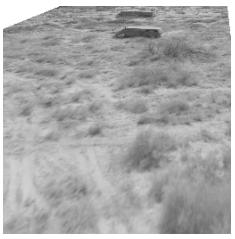

図 1: 変形されたテスト画像

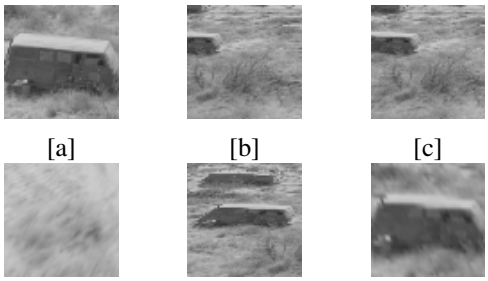

[a] [b] [c]

[d] [e] [f]

図 2: テンプレート，検出位置の画像及び変形画像

参考文献

[1] 若原　徹, 小高　和己, **大局的アフィン変換を用いた形状マッチング**, 信学技報, PRMU96-2, May, 1996.

[2] 若原　徹, 木村　義政, 山下　喜義, *GAT* **反復を用いたアフィン変換不変の濃淡文字相関法**, 信学技報, PRMU99-31, June, 1999.

[3] Toru Wakahara, Yukihiko Yamashita, “Acceleration of GAT Correlation for Distortion-tolerant Image Matching”, Proc. of ICPR 2012, pp746–749, Tsukuba, Dec. 11-15, 2012.

Influence of curing water containing various ions on permeability of concrete and its application to water supply curing method

Student Number: 12-01232 Name: Kazuki Ishihara Supervisor: Prof. Nobuaki OTSUKI

1. Introduction

Curing is known to affect the quality of concrete, especially durability, that is closely related to permeability.

The solution used for curing must not contain harmful amounts of substances affecting the surface of the concrete, such as oil, acids and salts. Thus, it is possible to use various solutions for curing.

However, investigation on the effect of the type of curing water on performance of concrete is very few.

One of the curing method used in the actual construction is water supply curing method[1]. If the effects obtained in water supply curing method are almost equal to the results of those in underwater curing, it can be applied to the actual construction.

In this study, the purposes are following two.

(1) To clarify influence of various ion in curing water on material permeability of concrete.

(2) To clarify the applicability of water supply curing method with using various solution.

2. Experiment outline

2.1 Specimens

(1) Mortar specimens

Cylinder specimens were used for compressive test (φ5cm×10cm) .Prism specimens were used for Carbonation test and chloride ion penetration test (4cm×4cm×16cm) . The mix proportion is shown in Table 1.

(2) Concrete specimens

Cylinder specimens were used for compressive test (φ10cm×20cm). Prism specimens were used for Carbonation test and chloride ion penetration test (10cm×10cm×40cm) .

The mix proportion is shown in Table 2.

(3) Reverse T-type specimens assuming the actual structure

Two sizes of cylinder cores were taken from the actual wall φ7.5cm×10cm cylinder cores were used for compressive test. φ10cm×10cm cylinder cores were used for carbonation test and chloride ion penetration test .

The mix proportion is shown in Table 2.

2.2 Measurement items

(1) Compressive strength

(2) Carbonation rate coefficient

Concrete specimens has been exposed under CO_2 10% condition. Except exposure side (underside in construction), surface of concrete is sealed by epoxy. Results is conversed into air environment by using Uomoto formula[2].

(3) Chloride ion diffusion coefficient

Salt water (NaCl 3%) was sprayed at 50℃ environment. Except exposure side (underside in construction), surface of concrete is sealed by epoxy.

2.3 Kinds of solution and curing method

Table 3 shows kinds of solution and curing method.

As solution, seawater, bittern (Table 4) and magnesium acetate solution were selected expecting magnesium hydroxide deposition which colud cover surface on concrete.

Natto bacteria, sodium carbonate (Na_2CO_3) and sodium hydrogen carbonate ($NaHCO_3$) solution was selected expecting densification by carbonation.

Natto bacteria need nutrient and O_2. So, solution in natto bacteria contained a material (Table 5), and it was pumped air.

Curing of mortar specimens and concrete specimens cured in under each solution. Curing of

Table1, mix proportions of mortar specimens

W/C(%)	S/C	C(Kg/㎥)	S(Kg/㎥)	W(Kg/㎥)
55	2	612.5	1224.9	319.9

Table2, mix proportions of concrete and reverse T-type spacemen

Cement type	slump (cm)	air content (%)	water-cement ratio W/C (%)	sand-aggregate ratio s/a (%)	quantity of material per unit volume of concrete (kg/m³)					
					water	Cement	sand S		gravel	chemical admixture
					W	C	S1	S2	G	Ad.
OPC	12.0±2.5	4.5±1.5	55	44	169	307	547	245	1038	3.28

Table3, solution and curing method

No.	name	Use solution	demoulding	curing after demoulding
1	Tap water	Tap water	1 day	Atmospheric curing after 7days curing in underwater
2	Seawater	Artificial seawater		
3	Bittern	Bittern		
4	Natto bacteria	Natto bacteria		
5	Na_2CO_3	sodium carbonate 1.0mol/l		
6	$NaHCO_3$	sodium hydrogen carbonate 1.0mol/l		
7	$(CH_3COO)_2Mg1$	Magnesium acetate 1.0mol/l		
8	$(CH_3COO)_2Mg0.1$	Magnesium acetate 0.1mol/l		
9	$(CH_3COO)_2Mg0.01$	Magnesium acetate 0.01mol/l		

Table4, bittern

item	Analysis value
Magnesium chloride·$MgCl_2$	12.70%
Sulfate·SO_4	3.00%
Bromide·Br	2.5% or less
zinc·Zn	70μg/g
calcium·Ca	0.1% or less
sodium·Na	2.60%
potassium·K	1.00%
heavy metal·As Pb	5μg/g or less
arsenic·As_2O_3	1.0μg/g or less

Table5, nutrient of natto bacteria

Reagent name	concentration (g/l)
glucose : $C_6H_{12}O_6$	20
Ammonium chloride : NH_4Cl	7
dipotassium hydrogenphosphate : K_2HPO_4	0.5
Magnesium Sulfate Heptahydrate : $MgSO_4 \cdot 7H_2O$	0.5
Ferrous chloride tetrahydrate : $FeCl_2 \cdot 4H_2O$	0.031
Calcium chloride dihydrate : $CaCl_2 \cdot 2H_2O$	0.15
Manganese(II) sulfate hydrate : $MnSO_4 \cdot H_2O$	0.1
D-Biotin : $C_{10}H_{16}N_2O_3S$	0.0005

Photograph 1, water supply curing method

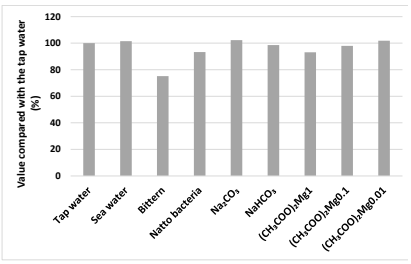

Figure 1, compressive strength of mortar specimens

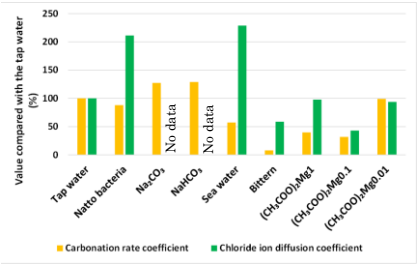

Figure 2, carbonation rate coefficient and chloride ion diffusion coefficient

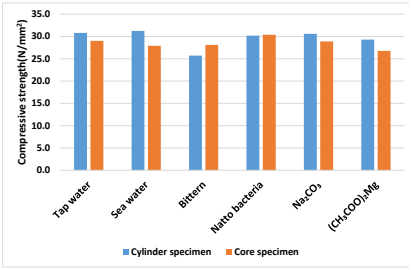

Figure 3, compressive strength of Cylinder specimens and core specimens

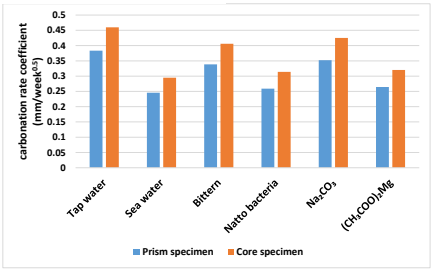

Figure 4, carbonation rate coefficient of prism specimens and core specimens

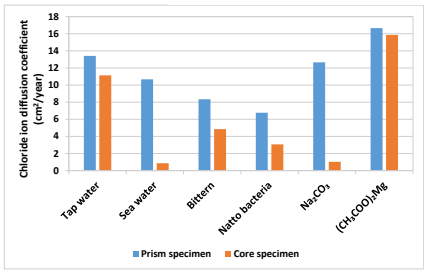

Figure 5, chloride ion diffusion coefficient of prism specimens and core specimens

reverse T-type specimens used water supply curing method as shown in the photograph 1.

3. Results and discussion

3.1 Select of solutions by using mortar specimens

Figure1 shows the result of the compressive test of Mortar specimens. Figure 2 shows the result of the carbonation test and chloride ion penetration test of Mortar specimens.

According to Figure 2, the result of carbonation rate coefficient and chloride ion diffusion coefficient cured in seawater, bittern and natto bacteria is better than that cured in tap water.

The most effective concentration of magnesium acetate to material permeability is 0.1mol/L.

Compared with sodium carbonate and sodium hydrogen carbonate, sodium carbonate is better than sodium hydrogen carbonate.

It is found that the best concentration of magnesium acetate is 0.1mol/L .

It is found that sodium carbonate is effective in the solution containing carbonate ions.

3.2 Compressive strength

Figure 3 shows the result of the compressive test of concreate specimens and core specimens.

According to Figure 3, compressive strength of cylinder specimens cured in all solution except bittern is equal to that cured in tap water. However, compressive strength of core specimens cured in bittern is equal to that cured in tap water. It is considered that surface affected by the curing is only one in water supply curing method.

3.3 Carbonation

Figure 4 shows the result of the carbonation test of concreate specimens and core specimens.

Carbonation rate coefficient of prism specimens cured in all solution is better than that cured in tap water, particularly seawater, natto bacteria and magnesium acetate is good.

Trend is the same in underwater curing and water supply curing method. It is considered that water supply curing method can be applied about durability to carbonation.

3.4 Chloride attack

Figure 5 shows the result of the chloride ion penetration test of concreate specimens and core specimens.

Chloride ion diffusion coefficient of prism specimens cured in all solution except magnesium acetate is better than that cured in tap water.

Chloride ion diffusion coefficient of prism specimens which cured in natto bacteria solution is the lowest. However, chloride ion diffusion coefficient of core specimens cured in seawater and sodium carbonate solution is the lowest.

It is found that effect about durability to chloride attack is not necessarily the same in underwater curing and water supply curing method.

4. Conclusions

(1)Compressive strength cured in solution containing various ions by water supply curing method is almost equal to that cured in tap water.

(2) Carbonation rate coefficient cured in seawater, natto bacteria and magnesium acetate is smaller than that cured in tap water.

(3) Chloride ion diffusion coefficient cured in seawater, sodium carbonate and natto bacteria is smaller than that cured in tap water.

(4) Water supply curing method can be applied with little advantages compared to underwater curing.

5. Reference

1) Hazama Ando Corporation: Water Supply Curing System of Concrete Structure, "Aqua Curtain";2013.4

2) K.Uomoto・Y.Takada: The effect of carbon dioxide concentration on the neutral rate of concrete, Production research, Vol.43,No. 6, pp.35-pp.38, 1991.6

Relationship of Automobile Use with Urban Residential Zones Classification and the Transition

Student Number: 12_16096 Name: Tianzi LU Supervisor: Shinya HANAOKA, Kumiko NAKAMICHI

1. Introduction

Outflow of population from rural areas causes population increasing in metropolitan area which results in wider and wider range of living area. As urban area spread chaotically to suburbs, where transportation facilities, especially public transportation are not in place, residents have high dependence on automobile. As a result, motorization was progressed rapidly that caused higher environmental load. Moreover, Japan is facing problems of population decreasing and aging, especially in local area, which makes urban center declining. Since the city is sprawled with low population density, the whole city is no longer efficient for infrastructure management and welfare care.

Compact city is considered as an efficient and ecological urban structure with the concept of high population density, mixed land use and residential zones linked by public transportation[1]. In April 2014, Japan modified "Act on Special Measures concerning Urban Reconstruction", which makes local government formulate "Location Optimization Plans" and decide "Urban Function-attracting Districts" and Resident-attracting Districts" along public transportation corridors, in order to promote compact city policy. While determine Location of the Urban Function-attracting Districts and the Resident-attracting Districts, there is a need of database reference that based on the latest urban data on scale of residential zones which corresponds actual scale of urban development plans. To begin with, it's important to clarify the transition of residential zone types in the past based on nationwide data. Though Hashimoto et al.[2] focused on change of population density, analysis for other characteristics of residential zones is required.

The objective of this study are 1) to clarify transition of characteristics of residential zones and the relationship with automobile use, 2) to make new residential zones classification based on the latest data considering results of objective 1).

2. Data Collection and Target

The National Person Trip Surveys (NPTS) in 1992 and 2010 are used for gasoline consumption calculation and residential zones classification. Population density is collected from the National Population Census by corresponding to each district to survey zone of NPTS.

The ratio of each land use regulation area is calculated by overlapping municipal map, district map and urbanization control area map from the National Land Numerical Information (NLNI) with using GIS. The latitude-longitude of zones' center, stations and city center of every city are collected from NLNI and changed into rectangular coordinate, in order to calculate distance from center of zones to city centers or the nearest cities.

Research target of objective 1) are zones investigated in NPTS in both 1992 and 2010 (except Tokyo). Zones of NPTS in 2010 are used for objective 2). Since survey target and zone names of NLNI and NPTS are different from each other, zones could not be found in both of them are excluded. In order to ensure accuracy of average gasoline consumption, zones with less than 5 persons are excluded. As a result, 1,878 zones in 69 cities were analyzed in this study.

3. Methodology

3.1 Per capita automobile gasoline consumption [3]

This study targets car single trips and the mixed trips of car and walking. The targeted trips constitute the majority of car using trips (97.5%). It's a reasonable proxy for the amount of the car use. The automobile gasoline consumption for each unit distance on weekday was calculated using Eq.(1) and Eq.(2) in consideration of traffic congestion etc. using car velocity. S_c and □□ was calculated by ratio of car and walking in every trips.

$$FC=\frac{829.3}{v_c}-0.8572v_c+0.007659v_c^2+64.9 \quad (1)$$

$$GC=FC*S_c \quad (2)$$

FC: Gasoline consumption per kilometer

v_c: Automobile speed. S_c: Distance by automobile

3.2 Residential zones classification model

For objective 1), comparison of residential zones types in 1992 and 2010 was based on existing residential zones classification[4].

For objective 2), five characteristics (Table 1) that have high relation with the concept of compact city are decided as classification criteria. Compared with existing classification[4], non-city planning area is added as one land use regulation type.

Table 1 Residential zone characteristics used for classification

Items	Categories		
City type	Central City in Metropolitan Area (CM)		
	Satellite City in Metropolitan Area (SM)		
	Central City in Local Area (CL)		
	Local City in Local Area (LL)		
Population density	1: < 50 (persons/ha)		
	2: 50 ~100 (persons/ha)		
	3: 100~150 (persons/ha)		
	4: ≥150 (persons/ha)		
Land use regulation	Urbanization control area	25% ~50% (UCA-1)	
		50% ~75% (UCA-2)	
		≥75% (UCA-3)	
	Residential type	Low-height residential use	≥90% (LR-1)
			60%-90% (LR-2)
		High,medium-height residential use	≥90% (HR-1)
			60%-90% (HR-
		Genertal residential use	≥60% (GR)
	Commercial type	Neighbourhood commercial use	≥60% (C-1)
		Commercial use	≥60% (C-2)
	Industrial type	Ligh industrial use	≥60% (I-1)
		Ind.and exclusively ind.use	≥60% (I-2)
	Residential-commercial mixed type (RCM)		
	Mixed use type	Mixed-use residential (M-R)	
		Mixed-use commercial (M-C)	
		Mixed-use indurstrial (M-I)	
	Non-city planning area	Non-city planning area>urban planning area (NCP)	
Distance to the nearest station	1:<1 (km)		
	2:≥1 (km)		
Distance from city center	1: <1.6 (km)		
	2: 1.6~<5 (km)		
	3: ≥5 (km)		

Fig.1 shows the classification process. Correlation coefficient (r) of characteristics with gasoline consumption are criteria for classification. r is significant when $|r|\geq 1.9407*x^{-0.498}$ (Eq.(3)). Eq.(3) is cumulative approximate of r when p=0.05, x=sample number. For criteria 3 and 4, categories were decided based on Table 1, but categories were merged when difference of

average gasoline consumption was less than 200cc.

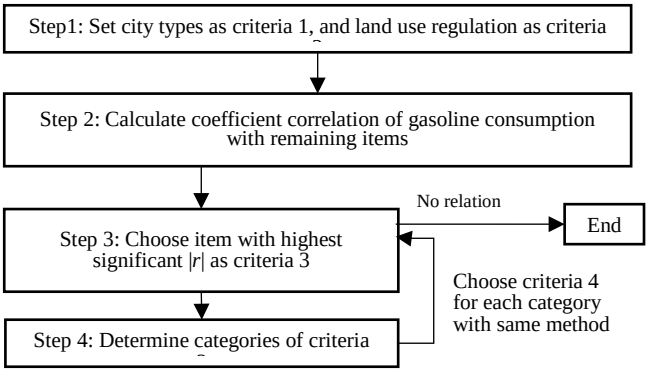

Fig.1. Process for classification of residential zones types

4. Results and Discussion

Among 601 common investigated residential zones in 1992 and 2010, 53 zones (22/135 residential zones types) disappeared and 10 types of them are residential type. By plotting residential zones with more than 5 zones changed to, we found many residential zones was belonged to residential land use types changed to mix-use land use types (Fig.2). There is no big change in residential zones belongs to commercial type. Changes of land use regulation occurred in 300 zones. When land use regulation changed into residential-commercial mixed use from other land use regulation, gasoline consumption decreased remarkably.

Based on residential zones data in 2010, 1,878 zones are classified into 119 types. Table 2 shows the classification result of CL. In CL, gasoline consumption depends on location of zones in that city. Gasoline consumption of zones in CM and SM is low and has high relation with population density. Zones in LL generally have high automobile use and low population density, and relation of gasoline consumption with urban layout is weak. As for land use regulation, residents living in zones that contain commercial areas tend to have lower gasoline consumption.

5. Conclusion

This study analyzed 1,878 residential zones of 69 cities which can cover all existing residential zones in Japan and calculated automobile use of each zone type. Zone types of 66.7% of common investigated zones changed from 1992 to 2010, especially many specific residential land use regulation districts changed to mix-use land use districts.

This study shows urban layouts affects automobile use, but the zone characteristics that affects automobile use differs a lot in case of land use regulation and city types. Many residents in local area are living in zones belong to non-city planning area with high automobile use. Therefore the “Location Optimization Plan” needs to be promoted in local areas. This study analyzed characteristics of residential zones and how it affects automobile use by residential zone type classification and the results proved compact city urban layout is efficient in reducing automobile use.

For further study, analysis of residents attributes such as age and household type in every zone types could show patterns of residents flow needed in every residential zone types. That will be an indicator of ideal house moving which has high relation with urban function location.

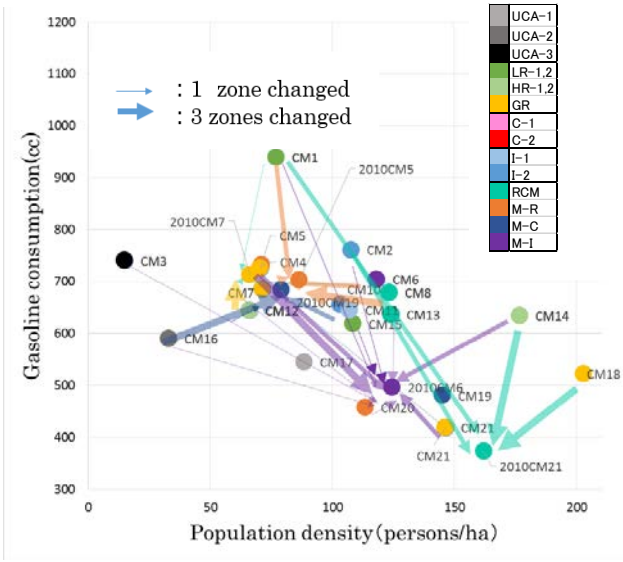

Fig.2 1992-2010 change of residential zones types(CM)

Table 2. Classification result of CL

Zone types	Land use	Population density (persons/ha)	Distance from city center (km)	Distance to nearest station (km)	Gasoline consumption(cc)	No. of zones
CL1	UCA-1		<1.6		521.8	5
CL2	UCA-1		1.6~5		911.8	23
CL3	UCA-1		≧5		1208.7	17
CL4	UCA-2	<50			1092.9	21
CL5	UCA-3			<1	938.4	12
CL6	UCA-3			≧1	1184.7	60
CL7	RCM				838.9	63
CL8	LR-2		<1.6		828.2	1
CL9	LR-2		≧1.6		1034.1	25
CL10	LR-1	<100		≧1	1017.5	5
CL11	HR-2	<100			933.4	24
CL12	HR-1	<50	<1.6	<1	854.3	2
CL13	HR-1	<100	≧1.6	<1	520.7	3
CL14	HR-1		>1.6	≧1	916.6	3
CL15	GR		<5	<1	702.5	41
CL16	GR	<100	<5	≧1	855.0	21
CL17	GR		≧5		1108.2	7
CL18	C-1		≧5		574.2	7
CL19	C-2		<5		704.2	26
CL20	I-1		<1.6		564.8	3
CL21	I-1		≧1.6		776.5	7
CL22	I-2	<100	<5	<1	907.6	4
CL23	M-R	<50	<5		800.3	42
CL24	M-R	<100	≧5		1155.8	8
CL25	M-C	<100			824.9	8
CL26	M-C	≧100		<1	509.3	2
CL27	M-I	<100		<1	893.7	11
CL28	M-I	<100		≧1	1139.5	4
CL29	NCP		≧5		1019.0	36

:Criteria 3 :Criteria 4

References

[1]OECD: Compact City Policies, A comparative assessment, OECD green growth studies, OECD publishing, 2012

[2] 谷口守, 松中亮治, 橋本晋輔: 公共交通整備状況と地区人口密度からみた都市拡散の関連分析, 都市計画論文集, No.44-1, pp.117-123, 2009.

[3]平野全宏, 中道久美子, 谷口守, 松中亮治: 都市別自動車 CO_2 排出量の定量化とその経年変化分析, 環境システム研究論文集, Vol.36, pp.19-26, 2008.

[4]中道久美子, 谷口守, 松中亮治: 交通環境負荷低減に向けた都市コンパクト化政策検討のためのデータベース「住区アーカイブ」の構築, 土木学会論文集 D, Vol.64, No.3, pp.447-456, 2008.

Numerical Analysis of Tsunami Overflow behind Coastal Dykes

Student Number: 12B10811 Name: Tomoya NAKAMURA Supervisor: Hiroshi TAKAGI

1. Introduction

The 2011 Great East Japan Earthquake and Tsunami caused devastation of sea dykes, exacerbated by overflow and scouring behind the structure. In the course of the reconstruction from the disaster, the Committee for Technical Investigation on Countermeasures for Earthquakes and Tsunamis of Cabinet Office emphasized that coastal protection facilities need to be more resilient so that a moderate structural performance which contributes to a reduction in tsunami impacts could be sustained even after the dyke has been partially destroyed. In order to put this into practice, the mechanisms on how a coastal dyke has been devastated need to be more understood. Particularly, the influence of the shape of coastal dykes on the tsunami overflow should be investigated.

This study, took the following steps: (1) conducted a field investigation to measure the dimensions of the coastal dykes; (2) verified the numerical model by comparing with previous experimental data; and (3) evaluated the tsunami overflow behind a coastal dyke in Ishinomaki using a hydraulic model.

2. Field Investigation

The authors conducted a field investigation to measure the dimensions of new coastal dykes using a high-precision GPS and leveling staff in Ishinomaki City and Sendai Plain. The shapes of coastal dykes are different between Ishinomaki City and Sendai Plain, and thus three different shapes of coastal dikes were analyzed in this research:

1) Type A: Thin rectangular wall with 5-m height (the dyke type in Ishinomaki before the 2011 event);
2) Type B: Trapezoidal shape with 1:2 slope and 5-m height (the dyke type in Sendai Plain after the event);
3) Type C: Trapezoidal shape with one sloping side with 1:2 slope (inward) and one vertical side with 7.5-m height (seaward) (the dyke type in Ishinomaki after the event).

Fig.1 The locations of the coastal dikes investigated in the current study

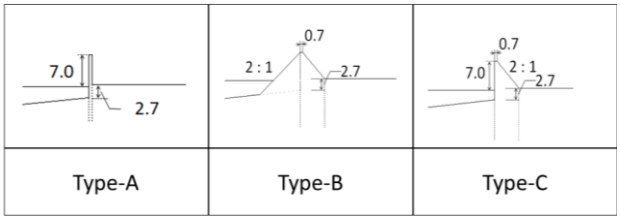

Fig.2 The coastal dyke under construction in Ishinomaki City (photo taken on Sep 2015)

3. Numerical analysis

In this research, ANSYS FLUENT (Ver.16.1) was applied to investigate the tsunami overflow passing the coastal dyke. Firstly, the comparison with experimental data [1] was made in order to confirm the suitability of the numerical analysis. Secondly, numerical analysis of tsunami overflow using the three types of dyke was performed.

Table.1 Calculation settings for vertical 2D simulation

	Model verification	Investigating tsunami overflow
Domains	L17m × H1.5m	L500m × H49m
Grid space	0.5cm ~ 5cm	0.1m ~ 1.0m
Time increment	0.001sec	0.01sec
Total duration	120sec	150sec
Wave type	Cyclic waves	Tsunami-like wave
Boundary conditions	Water surface elevation at the offshore boundary and transmitted wave condition at the inshore boundary	
Basic equations	Navier-Stokes equation, Continuity equation	
Turbulence model	Standard k-ε	
Free surface analysis model	Volume of Fluid Method	

3.1 Validation of the model from the experimental data

The model validation was conducted by comparing the water pressures measured from the experiment, in which a vertical breakwater was placed as shown in Figure 3. Input wave is a cyclic wave with a period of 1s and wave height of 10cm. The data of experiment and the result of numerical analysis measured at 6cm below the water surface were processed by a bandpass filter (0.5~20Hz). The comparison of the results is shown in Figure 4. Despite the minor differences being observed, the results of numerical analysis fitted well the experimental values.

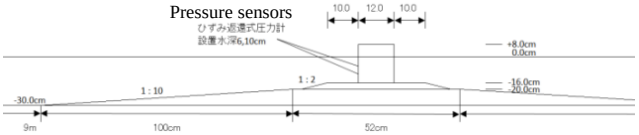

Fig.3 The breakwater installed in the experiment

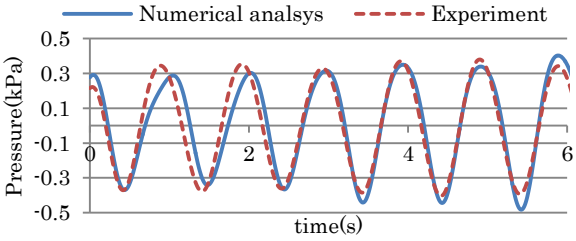

Fig.4 The result of comparison between numerical analysis and experiment

3.2 Flow characteristics around dykes

3.2.1 Settings of numerical analysis

Numerical analysis was performed under the settings shown in Table 1. The dimensions derived from the field investigation were used for the three models. The height of the dike for all models was set to 7 meters. Velocity and water level was measured at 25m, 50m, 75m and 90m points behind the dyke. In order to avoid the effect of unrealistic wave reflections from the offshore boundary, relatively short-period tsunamis were used as input wave as depicted on Figure 5. Therefore, it is noted that this study focuses on the maximum velocities and water levels, rather than the time-history of tsunami overflows.

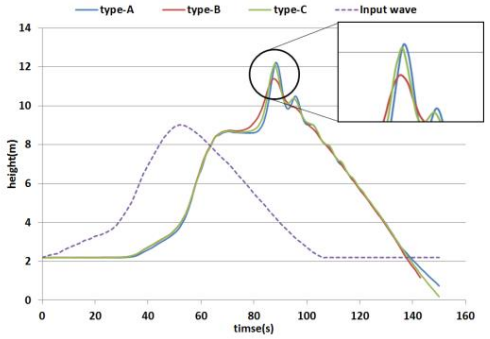

Fig.5 Input wave (offshore wave height 9m) and water levels simulated 150m off the dyke

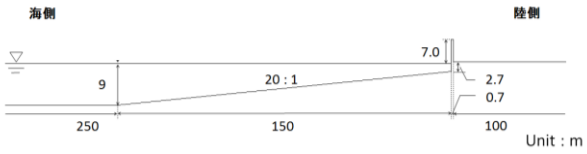

Fig.6 Cross-section of the domain with Type A dyke

3.2.2 The velocity behind the dykes

Figure 7 shows that Type A dyke produced the least velocity values, which may be attributed to the strong turbulence generated behind the dyke as shown in Figure 8.

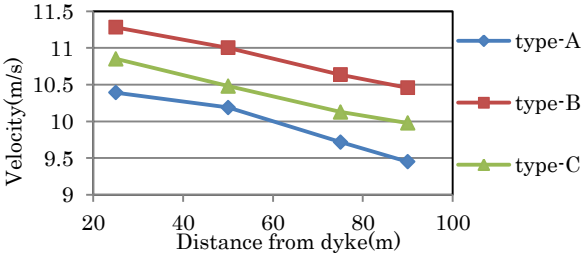

Fig.7 The relationship between velocity and distance from the dyke

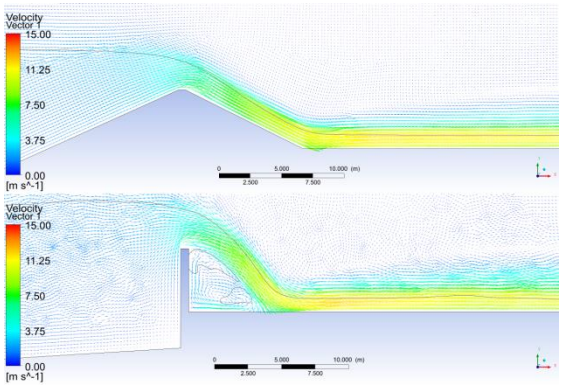

Fig.8 Velocity around dykes

3.2.3 Water level behind the dykes

Figure 9 shows the results of relation between water depth and tsunami. Four cases of incident tsunamis with 6m, 7m, 8m and 9m-height were used. To obtain the flow rates, the authors multiplied the maximum value of velocity and water depth for each case. The result shows that Type B produced the largest flow rate. This may be attributed to the shape of the dyke where the sloping side facing the sea causes weak reflection waves. Figure 5 shows that Type A and Type C induce higher water levels than Type B due to reflection from the dyke.

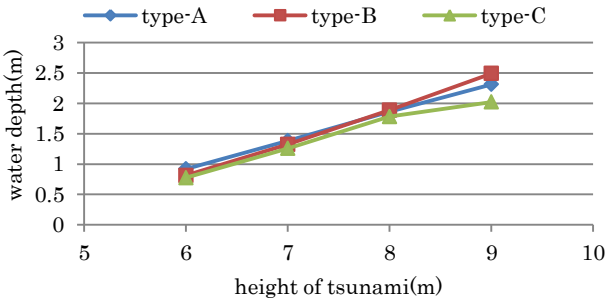

Fig.9 Water depth and tsunami height

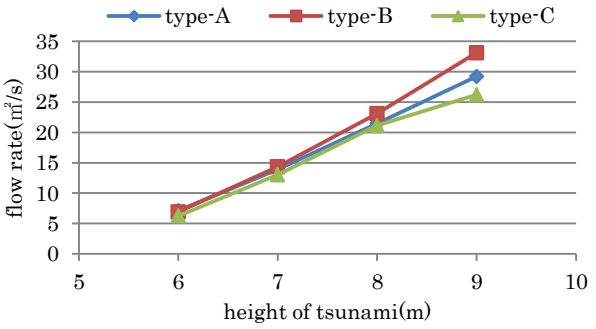

Fig.10 Flow rate and tsunami height

4. Conclusion

The numerical model was validated through the comparison with the previous experimental data. Furthermore, the effects of the difference in dyke shape to velocities and water levels behind the dykes were confirmed.

References

[1] 高木泰士，中島ちひろ (2007):“防波堤に作用する重複波圧の推定精度の定量的評価に関する研究”，土木学会論文集 B，Vol.63，No.4，pp291-294，2007

Effects of arc current and voltage between electrodes on arc re-ignition

Student Number:12_03640 Name: Tadayuki Omata Supervisor: KunioTakahashi

1 Introduction

Arc discharge is an electrical breakdown of a gas that produces a plasma discharge, resulting from a current through normally nonconductive media such as noble gas. Arc discharge is applied to welding because it has high temperature around seven thousand to twelve thousand degree. The breakdown voltage usually ranges from a few kV to tens kV. But arc re-ignition voltage is lower than the breakdown voltage. The arc re-ignition is same to the voltage needed to hold arc discharge, usually around tens voltage.

In arc welding, anode has higher temperature than cathode because of emission of energy which is equivalent to work function of anode. This causes problems because the amount of melt effects on strength and shapes of welded part. So it is important to control arc re-ignition, which means it is possible to stop arc among intended time and re-ignite arc discharge in the arc holding voltage. To do so, it is needed to know the mechanism of arc re-ignition at lower voltage. In this research, the effect of arc current before the re-ignition and voltage between electrodes on the re-ignition is investigated.

2 Experimental Equipment

Electrode bars are used in arc re-ignition experiment. The electrodes for anode and cathode have a same material and form. The material is W containing 2% ThO2. The diameter is 1mm. The electrodes is covered by a glass tube and Ar is flowed into the tube for preventing oxidation. The flow is around 0.17m^3/min. The distance of electrodes, d, is controlled by a micrometer connected to the anode.

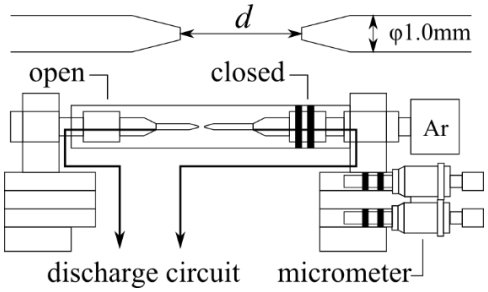

Fig.1 schematic illustration of electrodes

Arc current and voltage between electrodes are also controlled by the experimental circuit. The circuit is shown in Fig.1. The circuit contains three differential amplifiers, non-converting amplifier, FET and a capacitor. The capacitor is used as a constant power supply and the capacitor is charged by transfer.

When arc current flows, the current control system is started. Increasing current in the resistance R1 shown in Fig.1, The output of ① increases. The difference between output of ① and another output of ③ is output of ②. Then non-converting amplifier adds output of ② to gate source voltage of FET. So, the more there is electric potential in R1, the less gate source voltage is. Therefor arc current is controlled.

When there is output from PIC, the input to differential amplifier of ① is zero. Then voltage of output of ① is below zero. So, gate source voltage of FET is also below zero and FET is off. So, arc current flowing in R1 is stopped. Therefor arc-less time, which is time that arc current is stopped, is controlled by output of PIC.

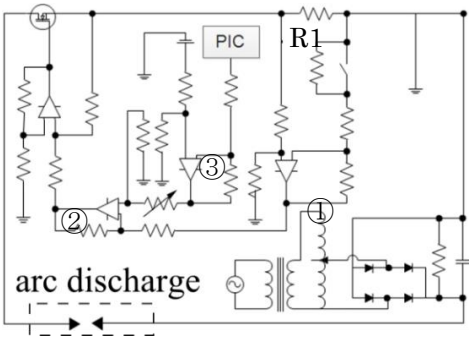

Fig.2 electrodes and arc discharge circuit

Fig.3 shows how voltage between electrodes is controlled. I is ampere of current flowing in R1. Ic is an ampere of controlled current before the current is interrupted. U is voltage between electrodes. τ is arc-less time. FET on or off in Fig.3 means the gate source voltage of FET is high or low. Re-ignition in Fig.3 means start of arc re-ignition after arc current is interrupted. Before arc current is interrupted, I=Ic, U is determined by current-voltage characteristic. When arc current is interrupted, I and U is zero. After the end of arc interruption, U become same to Vc, because electrical voltage of drain source of FET and R1 is zero. So U is controlled by controlling Vc after the end of arc interruption

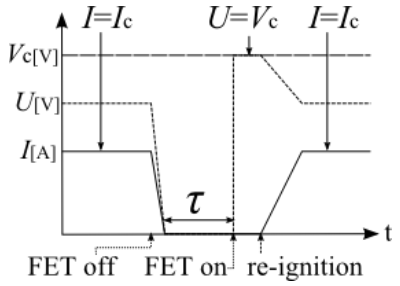

Fig.3 image of U control system after arc-less time

3 Experiment Result

When FET control or stop arc current, certain amount of voltage is generated at Vds, which is drain source voltage of FET. So, in order to know current control is worked, Vds is measured in the arc re-ignition experiment. The schematic illustration of waveform is shown in Fig.4. Vds is determined by amount of interrupted current and voltage. In arc-less time, Vds increases to Vc, therefor U is zero and arc current is interrupted. After arc-less time, Vds is zero because current is not interrupted. When I start to increase and reaches certain amount of ampere, current control also starts. Therefor Vds starts to increase.

At first, re-ignition experiment is done in case that Ic=0.8～1.4A, U=30～60V, d=5.0mm, 10.0mm, and τ=700μs. In Fig.5, I showed results of success of the re-ignition in each of the conditions. ○ is in case of d=5.0mm. □ is in case of d=10.0mm. △ means success rate is from 30% to 70% in case of d=5.0mm. White means success and black means failure. Field intensity is calculated by U/d.

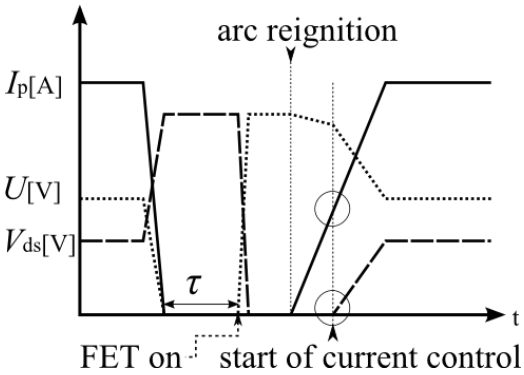

Fig.4 schematic illustration of waveforms of current, *U*, and *Vds* in the arc re-ignition experiment

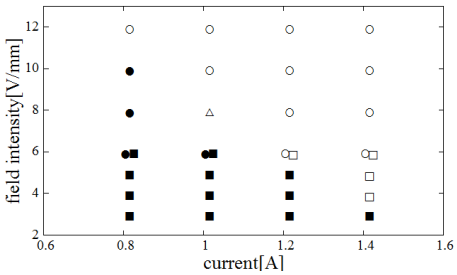

Fig.5 Results of arc re-ignition in case that *Ic*=0.8～1.4A, *U*=30～60V, *τ*=700μs, and *d*=5.0mm,10.0mm

Fig.6 is a part of current waveforms in case that *Ic*=0.8A, 1.0A and 1.2A, *U*=30V, *d*=5.0mm, *τ*=200μs. The time range of Fig.6 is from 200μs to 350μs. The zero point is start of τ. Vertical lines are drawn at the points when *Vds* is 1V in each conditions. Current control is not started before the intersections of waveform and vertical lines, because 1V is low compared with *U*. ○ in Fig.6 are points of intersection of the current waveform and vertical line.

In Fig.6, all waveform succeeded arc re-ignition. There are vibrations at waveform of *Ic*=0.8A and 1.0A. The time period is 60μs and 40μs. Looking more detail, it is found that there are vibrations having another time period ranging from 220μs to 250μs at the waveform of *Ic*=1.0A and ranging from 330μs to 340μs at the waveform of *Ic*=0.8A.

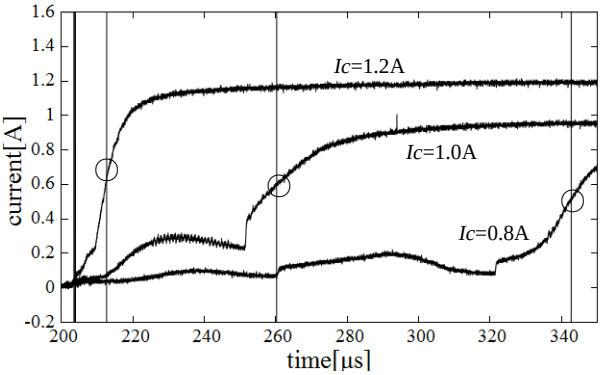

Fig.6 a part of current waveforms in case of different *Ic*

Fig.7 is a part of current waveform in cases that *Ic*=0.8A, *U*=30V, 40V, and 50V, *d*=5.0mm, and *τ*=200μs. The time range is from 200μs to 230μs, and the zero point is when arc current is interrupted.

In each of waveforms, the rate of increase of arc current is different. The more *U* is, the higher rate of increase is. There are vibrations of arc current in case of *U*=30V and 40V. Each of the time periods is 3μs and 60μs.

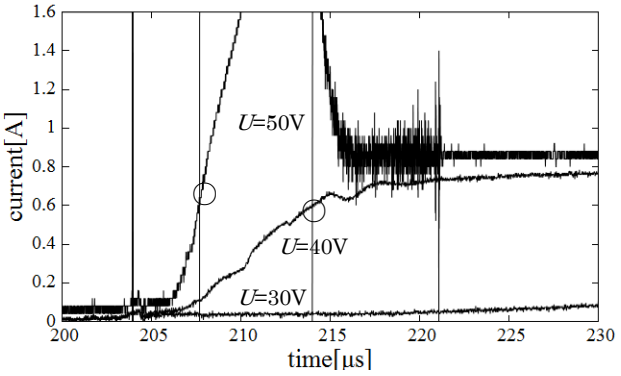

Fig.7 a part of current waveform in case of different *U*

4 Discussion

In Fig.5, it is found that both of arc current and electric intensity affect success of the arc re-ignition. It is shown that if distance between electrodes were not same, the success of the re-ignition is expected by measuring the arc current and field intensity calculated by *U/d*.

On the process of breakdown between electrodes, there is a vibration of arc current having certain amount of time period. The increase of current with the vibration would be concerned with γ_{ph} and γ_i effect as shown in Fig.8.

The effect happens when electrons collide with anode, and the energy is released as photons. Some photon makes ions near the anode. The ions go across electrodes and collide with cathode and electrons are released. That is called for γ_i effect. Other photons released in anode collide with cathode directly and make the cathode to release electrons. That is called for γ_{ph} effect. These electron would be measured as current with two type of vibrations having certain amount of time period which is when electron and ion cross the electrodes.

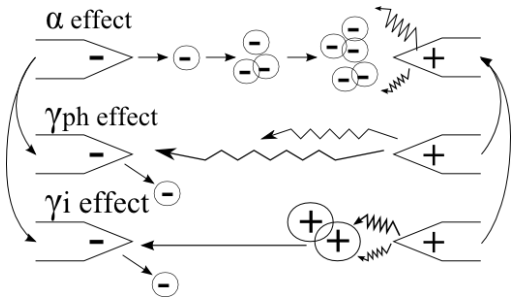

Fig.8 image of α, γ_{ph} and γ_i effect

5 Conclusion

Arc current and field intensity affects success of arc re-ignition. The waveform of current of arc re-ignition is investigated and it is shown that it is different how arc current or field intensity affect arc re-ignition. There is a possibility that γ_{ph} and γ_i effect works in arc re-ignition.

6 References

1:Masanori Hara, Yousuke Sakai, "KITAIHOUDENNRONN" Asakurasyoten 2015 2:Orimo "the Effect of Arc Current and Distance between Electrodes on Reignition Executable Time in DC Arc Discharge" bachelor thesis, Tokyo Institute of Technology, 2015

Analyzing linkages between solid waste management and other urban development sectors in developing countries: The case of Dhaka City, Bangladesh

Student Number: 12_07105 Name: Shinnosuke SAWAMURA Supervisor: Naoya ABE

1. Introduction

Globally more people live in urban areas than in rural areas, with 54% of the world's population residing in urban areas in 2014 [1]. Particularly developing countries are experiencing much faster urbanization than were ever experienced by today's developed countries. Due to this situation, cities in developing countries have numerous problems in various sectors such as solid waste management (SWM), water supply, sewerage, drainage, air pollution, slum, and transportation. Recently inclusiveness for urban development has been more emphasized by Sustainable Development Goals, which includes "Make cities and human settlements inclusive, safe, resilient and sustainable" as Goal 11, indicating that managing city sustainably is indeed a global challenge.

On the other hand, various government organizations are commonly approaching such urban problems individually. However, these urban problems are often inter-linked with each other. For example, if solid waste is uncontrolled, scattered waste could block drains in the city, worsening flood. Therefore, linkages between SWM and other urban development sectors need to be clarified within the overall framework of urban development.

Dhaka city is one of the cities being rapidly urbanized. The city has a population of 8.91 million and an area of 316 sq. km [2], and is divided into North and South parts. The city also has multiple urban problems, and there are also various government organizations such as Dhaka Water Supply and Sewerage Authority (DWASA), Capital Development Authority (RAJUK), Dhaka North City Corporation (DNCC) and Dhaka South City Corporation (DSCC), approaching them. In addition, multiple donor agencies have implemented numerous projects to assist such organizations in specific sectors. Figure 1 shows past implemented projects for Dhaka city development. However, coordination among these organizations is quite weak [3]. Therefore they need to be more coordinated but it hasn't been discussed enough in which linkage public entities should enhance the coordination. So inter-sectoral linkages occurring in the city and their priorities should be clarified.

2. Objective

The objective of this study is to clarify linkages between SWM and other urban development sectors and these priorities recognized by officers at waste management department (WMD), DNCC and DSCC (DCCs). This objective was designed in order to clarify inter-sectoral linkages between problems occurring in the city. This study in particular focuses on SWM sector due to its high visibility in many Asian cities.

The officers working at WMD, DCCs know this situation very well as practitioners of SWM. They frequently communicate with players relevant to SWM such as citizens and other related government organizations. So they have wider perspective on SWM in the city.

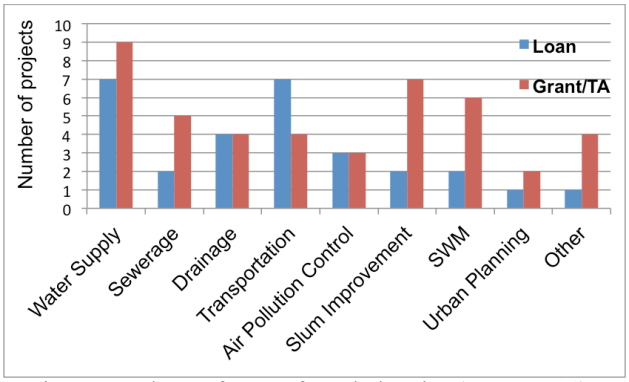

Fig.1: Numbers of ODA for Dhaka city (2003-2014)

3. Methodology

Semi-structured interviews were conducted with a help of a local waste management expert in September 2015. The numbers of respondents are summarized in Table 1.

Table 1: Numbers of respondents

Position	DNCC		DSCC	
	R	***N***	***R***	***N***
Chief Waste Management Officer (CWMO)	0	1	1	1
Zone Waste Management div.				
Assistant CWMO	5	5	4	5
Conservancy Officer	1	2~5	2	2~5
Conservancy Inspector	8	30~40	10	30~40
Cleaner/labor	0	3,000~	0	3,000~
Total	14		17	

Note. R: number of respondents *N*: number of populations

Three questions were mainly raised in the interview: priorities of SWM components, priorities of urban development sectors except SWM, and significant linkages between prioritized urban development sectors and SWM components. Respondents were asked to select highest, 2nd-highest, and 3rd-highest of the components and the sectors respectively, and also to answer any significant linkages as an open question.

As for the data analysis, this study evaluated priorities of inter-sectoral linkages by two criteria: the number of responses, and the priorities of related SWM components and urban development sectors. As for the number of responses, the more officers answered the linkage, the more prioritized it can be. Then three things—related SWM components, related urban development sectors except SWM, and influence direction between former two things—characterize a linkage. There are two cases of influence direction. One case is SWM components have a negative influence on the sectors, and the other case is an opposite one. A linkage can be also prioritized if related components/sectors influenced by the other sectors/components are highly prioritized. To evaluate priorities of SWM components and urban development sectors, correspondence analysis and cluster analysis were conducted.

4. Results

The results of the analyses for priorities of SWM components and urban development sectors are shown in Figure 2 and 3. Based on numbers of responses and evaluated priorities of components/sectors, linkages were evaluated as shown in Table 2. Table 2 shows only the linkages mentioned by more than eight respondents.

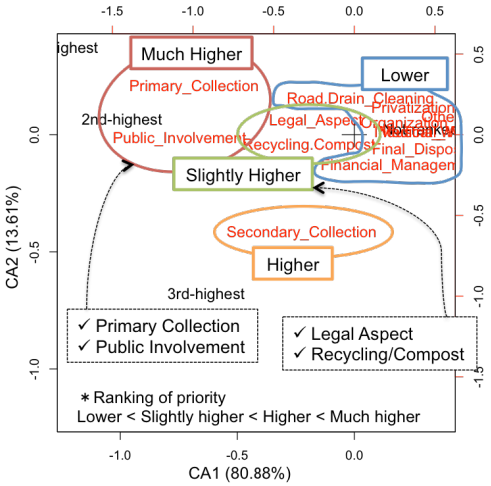

Fig. 2: Priorities of SWM components

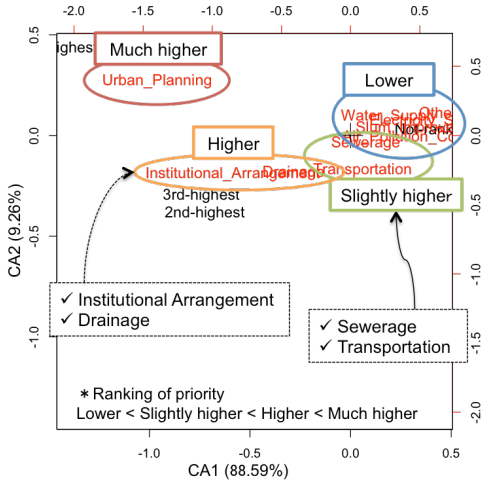

Fig. 3: Priorities of urban development sectors

As a result, the linkages marked with stars are found as particularly important and have much higher priorities. Also, all mentioned linkages have some common features and could be classified into four groups.

5. Discussion

As for urban planning, there is Dhaka Metropolitan Development Plan (1995-2015) prepared by RAJUK with assistance from UNDP/UNCHS. However, it doesn't consider SWM at all.

As for legal enforcement against illegal waste practices, police doesn't adequately play its role and duties but DCCs substantially supplement the police's role without its legitimacy of regulation. The legal responsibility against construction waste is unclear neither.

As for drainage and SWM sectors, both of them have serious problems: weak drainage function due to too old drainage facilities and quite low waste collection rate.

As for transportation, still serious traffic congestion frequently occurs in the city, even though multiple projects to improve transportation have been conducted.

These are the reason why four major linkages of urban problems written in Table 2, occurring in the city.

6. Conclusion

Four critical inter-sectoral linkages among urban development sectors are found in this study, namely those between urban planning and SWM, legal enforcement and SWM, drainage and SWM, and transportation and SWM respectively. Thus those four linkages should be prioritized for better and sustainable development of Dhaka city in the future.

References

[1] United Nations. (2014). World Urbanization Prospects The 2014 Revision, United Nations: New York, U.S.A.

[2] Bangladesh Bureau of Statistics. (2011). Population & Housing Census 2011.

[3] SENES Consultants Ltd. (2007). Dhaka Metropolitan Development Plan Strategic Environmental Assessment, The World Bank: Washington, D.C.

Table 2: Evaluation for priorities of linkages between SWM and other urban development sectors

Linkages	n^a	Related SWM components[b]	Influence direction	Related urban development sectors[b]
Group A: Lack of consideration for SWM by Urban Planning				
★ No space secured for secondary collection	17	Secondary Collection (3)	←	Urban Planning (4)
Group B: Legal Enforcement against Illegal waste practices				
★ Little observation of relevant laws by citizens (illegal dumping. illegal land possession, etc.)	14	Road & Drain Cleaning (1) Public Involvement (4) Legal Aspect (2)	←	Institutional Arrangement (3)
Inappropriate construction works (illegal dumping, illegal construction, etc.)	9	Road & Drain Cleaning (1) Legal Aspect (2)	←	Institutional Arrangement (3)
Group C: Interdependency between SWM and Drainage				
★ Blockage of drains by solid waste	14	Primary Collection (4) Road & Drain Cleaning (1) Public Involvement (4) Legal Aspect (2)	→	Drainage (3)
Insufficient drain cleaning and management by other organization, particularly DWASA	9	Road & Drain Cleaning (1)	→ ←	Drainage (3) Institutional Arrangement (3)
Waste scattered by water-logging	8	Road & Drain Cleaning (1)	←	Drainage (3)
Group D: Traffic congestion obstructing SWM				
★ Traffic jam obstructing secondary collection	14	Secondary Collection (3)	←	Transportation (2)

Note. [a]*n* is the number of responses. [b]The numbers in parentheses mean 4: much higher, 3: higher, 2: slightly higher, 1: lower.

東アジア域内におけるバルク貨物コンテナ化の要因分析

学籍番号:12_15955　氏名:米澤 祐介　指導教員:花岡 伸也

1. はじめに

1960 年代のコンテナ革命以降, 海上貨物に占めるコンテナ貨物の重量ベースの比率(コンテナ化率)は上昇を続けてきた．しかし，2000 年代後半になるとコンテナ化率は停滞し, 2015 年にいたるまで大きな変動がない．また，コンテナ輸送が抱える問題の一つとして，インバランスによる空コンテナの返送がある．バルク貨物のコンテナ化は空コンテナの返送費用削減のための有効な解決策の一つと考えられている．

特に東アジア域内では, 2015 年までコンテナ取扱量そのものは増加し続けているのにもかかわらず，コンテナ化率は 2000 年代後半からむしろ減少傾向にある．また，域内には経済発展度や貿易タイプの点で様々な国が存在することから，多角的な分析が可能である．

以上の背景を踏まえ，本研究では東アジア域内におけるバルク貨物コンテナ化の要因を明らかにすることを目的とする．

2. 手法と結果

本研究では，以下の三つの分析を通してコンテナ化率の要因を明らかにする．

(1) 品目別分析

品目別分析では, k -平均法を用いて７つの変数を基に東アジア域内で輸送される品目のグループ化を行い，どのような特性を持った品目でコンテナ化が進んでいるのかを分析する．

表１　クラスター分析結果

クラスター (品目数)	コンテナ化率変化 2000–2007(%)	コンテナ化率変化 2008–2014(%)	コンテナ化率平均 (%)	単価平均 ($/kg)	総輸送量平均 (十万トン)	コンテナ輸送変化 (十万トン)	バルク輸送変化 (十万トン)
1(21)	15.04	-0.09	92.70	3.66	9.9	5.6	-0.8
2(19)	0.75	-0.47	25.53	1.92	21.0	3.2	8.4
3(4)	11.03	1.44	44.39	1.08	310.6	102.9	86.2
4(8)	32.85	3.65	56.34	0.76	20.1	12.8	-2.7
5(3)	-5.38	-0.10	5.14	0.14	183.5	-4.3	159.2
6(1)	0.00	-0.27	64.98	179.34	0.14	0.1	0.1
7(7)	11.43	-1.71	30.40	0.69	110.5	34.1	38.8
8(66)	3.60	-0.78	87.68	7.98	9.1	5.6	0.8
9(4)	6.55	12.79	51.06	0.45	6.7	2.6	-1.3
10(3)	13.13	-23.37	75.81	0.75	22.6	16.9	7.5

表１より，クラスター番号 1,8 を見ると，コンテナ化率平均がそれぞれ 92.70%，87.68%と高く，また 2008 年以降のコンテナ化率が停滞している．これにより，工業製品や生鮮食品に分類される品目に関して, 2007 年までにコンテナ化が高い割合まで進んだために，それ以降のコンテナ化率が停滞していることが明らかになった．またクラスター番号２を見ると，コンテナ化率平均が 25.53%と低く，2000 年以降ほとんどコンテナ化が進んでいない．これにより，ドライバルク貨物に分類される品目は近年コンテナ化が進んでいないことが明らかになった．しかし，以上の要因は品目別分析では特定できなかった．

(2) 航路別分析

航路別分析では，二段階最小二乗法を用いて，二国間貿易のコンテナ化率を推定するモデルを構築し，どのような要因が影響するのかを明らかにする．二段階最小二乗法は，同時方程式による偏りを避けるために用いられる手法である．本研究では，総輸送量がコンテナ化率を推定する際に用いる説明変数であると同時に，コンテナ化率を算出する際の分母ともなっているため，二段階最小二乗法により同時方程式バイアスを避ける必要がある．

一段階目の重回帰式(1)では，操作変数$\boldsymbol{K_i}$とコンテナ化率Y_iの外生変数$\boldsymbol{L_i}$を用いて二国間貿易の総輸送量X_iを推定する．二段階目の重回帰式(2)では，得られた推定値$\widehat{X_i}$と外生変数$\boldsymbol{L_i}$を用いてコンテナ化率Y_iを推定する．

コンテナ化率・総輸送量を算出する際に，性質上コンテナ化ができない品目は除いた．分析対象とする航路は，陸続きとなっている二国間航路を除いた東アジア域内の航路とする．

$$X_i = \alpha_0 + \alpha_1 \boldsymbol{K_i} + \alpha_2 \boldsymbol{L_i} + \varepsilon_i \quad (1)$$

$$Y_i = \beta_0 + \beta_1 \widehat{X_i} + \beta_2 \boldsymbol{L_i} + \delta_i \quad (2)$$

① 一段階目

一段階目の重回帰式の結果を，表 2 に示す．F 値が 10 を超えているため，弱相関操作変数の問題はないと考えられる．

また，総輸送量に影響を与え，コンテナ化率に影響のない操作変数として, 輸出国 GDP, 輸入国 GDP, 二国間の主要港の航路距離を用いた．

表２　一段階目の操作変数と結果

F-statistic	14.34		
操作変数	単位	平均	標準偏差
輸出国 GDP	Trillion $	1.22	1.80
輸入国 GDP	Trillion $	1.22	1.80
主要港湾間の距離	海里	1563	772

② 二段階目

二段階目の重回帰式に用いた説明変数と予測される符号を表 3 に示す．

表３　二段階目の説明変数

説明変数		予測符号	単位	平均	標準偏差
輸出国特性	コンテナ取扱量	+	百万 TEU	30.90	43.2
	地上インフラ	+	-	3.55	0.5
	生鮮食品	+	%	3.73	2.9
	工業製品	+	%	74.28	14.2
輸入国特性	コンテナ取扱量	+	百万 TEU	30.90	43.2
	地上インフラ	+	-	3.55	0.5
	生鮮食品	+	%	2.94	1.3
	工業製品	+	%	64.44	10.9
二国間特性	総輸送量	−	百万トン	4.23	4.8
	単価平均	+	$/kg	5.70	6.0
	インバランス	−	千 TEU	5.84	240.5

重回帰式の結果を表 4 に示す．なお，輸出国の工業製品割合とインバランスは有意と表れたが，予測符号と異なっており，他の説明変数間との相関が考えられるため，それらの変数を除いたものを最終的

な結果とした．

表４　二段階目の結果

修正済み決定係数	0.39		
説明変数		係数	t-value
輸出国特性	コンテナ取扱量	0.0000000018	4.40***
	地上インフラ整備	0.0883	2.03**
	生鮮食品	0.016246	2.50**
輸入国特性	コンテナ取扱量	0.00000000058	1.22
	生鮮食品	0.0106	1.91*
	工業製品	0.0024	2.11**
二国間特性	総輸送量	-0.0000000089	-1.93*
	単価	0.0084	3.98***

Note: ***１％有意, **５％有意，*１０％有意

この結果より，輸出国の特性として地上インフラ整備，コンテナ取扱量，また貿易タイプとして生鮮食品，輸入国の工業製品の割合，二国間特性として，総輸送量と単価が重要な要因であることが明らかになった．なお，コンテナ取扱量はその国のコンテナ港湾設備の代理指標として用いている．

しかし，予想に反して二国間のインバランスは符号が異なる結果となった．理由として，東アジア域内での航路は比較的短いものが多く，コンテナ運賃を大きく引き下げるほど空コンテナの返送費用が大きくないことが考えられる．

また輸入国の地上インフラ整備・コンテナ取扱量も重要な要因とは示されなかった．地上インフラ整備に関しては，以下の理由が考えられる．一般に工業部品や金属などのバルク貨物を受け入れる荷主の工場などは港の近くにあることが多く、港からの陸送距離は長くない．そのため地上のインフラ整備が重要な要因とならなかった可能性が考えられる．

コンテナ取扱量に関しては，以下の理由が考えられる．一般にコンテナ輸送では，輸出国はコンテナ貨物を大きなコンテナ船に積み込み，途中のトランシップ港でコンテナ貨物を小さいコンテナ船に積み替えて輸入国へ運ばれることが多い．そのため，輸出国側では積み込みを行うために大規模なガントリークレーンなどの設備が必要であるが，輸入国側は大きな港でなくても積み下ろしを行うことができることから，輸入国側でのコンテナ取扱量が重要な要因とならなかった可能性が考えられる．

(3)　詳細分析

詳細分析では，航路別分析で構築したモデルとの誤差が大きく表れた航路を分析し，特定の航路に影響を与えている要因を明らかにする．表 5 は，残差分析により誤差が有意に大きいと特定された航路と，実際の航路のコンテナ化率とモデルで推定されたコンテナ化率を表したものである．

表５　誤差の大きい航路

輸出国	輸入国	推定されたコンテナ化率	実際のコンテナ化率
Philippines	Vietnam	57.2%	24.2%
Philippines	Hong Kong	75.3%	46.5%
Vietnam	Indonesia	50.7%	25.0%
Hong Kong	Japan	66.4%	44.6%
Hong Kong	Vietnam	65.6%	87.7%
Indonesia	Hong Kong	61.0%	85.3%

① 特定の品目による影響

誤差の大きい航路で輸送される品目を細かく見ると，コンテナ化されやすい品目として分類されているが，実際にはそのコンテナ化率が高くない品目があった．一つが香港発日本向き航路における金属スクラップ，もう一つがフィリピン発航路におけるバナナである．これらの製品はそれぞれ工業製品，生鮮食品に分類されているが，そのコンテナ化率は非常に低いものであった．

これらの品目のコンテナ化率が低い理由として，どちらも単価が非常に低いことが原因の一つと考えられる．また，バナナに関してはその輸送量が非常に大きいため，バルク船を利用するニーズが高いことも原因と考えられる．

② 単価による影響

コンテナ化率が実際よりも高く推定されたフィリピン発ベトナム向き航路，ベトナム発インドネシア向き航路に共通する性質として，著しく低い平均単価があった．これにより，単価が著しく低い航路においては，荷主はコンテナ化する利点を享受できない可能性が考えられる．

3.　結論

本研究では，東アジア域内におけるコンテナ化率の要因を明らかにするため，三つの分析を行った．品目別分析では，生鮮食品・工業製品がコンテナ化されやすい特性を持つ品目であることが特定された．航路別分析では，コンテナ化率に影響を与える要因として，輸出国のコンテナ取扱量と地上インフラ整備，二国間の総輸送量と単価を示した．また，コンテナ化率を進める要因であると考えられてきたインバランスが，航路の短い域内においては重要にはならない可能性を示した．さらに特定の航路において，コンテナ化されやすい性質の品目のコンテナ化が進んでいないことを明らかにした．また著しく平均単価が低い場合において，モデルの推定ほどにコンテナ化が進まない可能性を示した．

今後の課題として，別の地域におけるコンテナ化率の分析により，本研究で明らかにした要因の検証が必要である．

参考文献

[1]MartinStopford: “Maritime economics”, Routledge, 2009.

[2]松田琢磨，川崎智也: “バルク貨物コンテナ化の決定要因について－北米/韓国・台湾航路における金属スクラップ輸入の分析－”，海運経済研究，No.47，pp.65-73, 2013.

[3]Jean-Paul Rodrigue and Theo Notteboom: “Looking inside the box: evidence from the containerization of commodities and the cold chain”, Maritime Policy & Management，Vol. 42，No. 3，pp.207-227, 2015.

Application of Non-Linear Conjugate Gradient Method in Expectation Maximization Method for the Performance Improvement of Radio Channel Parameter Estimation

Student Number: 12B15688 Name: Yunyi Yao Supervisor: Jun-ichi TAKADA

1 Introduction

Recently, demands for high-speed and wide-band wireless communication system have been increasing significantly,and these systems are occupying most favorable electromagnetic spectrum for wireless communication (below 6 GHz band). Natrually, next generation mobile radio networks (5G) requires research toward the characteristics of channels at higher frequencies where we could occupy a larger bandwidth. Takada lab are focusing on 11GHz center frequency with 400MHz bandwidth which is a candidate carrier wave in next generation.

In the other hand, MIMO transmission is a powerful technique to improve the quality of wireless link transmission. Therefore, researh on performance of 11GHz based MIMO transmission becomes our motivation. However, the performance of MIMO communication systems is strongly dependent on propagation environment which is uncontrollable, so it is necessary to build an accurate MIMO channel model to evaluate the performance. To build such a model, propagation parameters of channels must be figured out accurately at first. EM-SAGE is well known as parameter estimation algorithm but its estimation performance is limited by resolution and huge computation. The aim of this research is to apply a gradient-base algorithm in parameter estimation in order to improve the accuracy and convergence speed. Super-high accuracy parameters estimation algorithm will help us to have better understanding of relationship between propagation environment and transmitted wave.

2 Over view of Parameter Estimation

2.1 Propagation Parameters

Fig.1 descirbes what are propagation parameters. In Ray-based MIMO channel model [1], transmitted signal is modeled by the superposition of multi paths, every path is unique and can be desribed by a group of parameter, *Direction of Departure (DoD)*, *Direction of Arrival (DoD)*, *Time delay of Arrival (ToA)*, and *Dual-polarized Path Weight*, l represents path ID. We can define a parameter vector to put them together except path weight. $\boldsymbol{\mu}_l = \begin{bmatrix}\tau_l & \theta_{T,l} & \varphi_{T,l} & \theta_{R,l} & \varphi_{R,l}\end{bmatrix} \in \mathbb{R}^{5\times 1}$

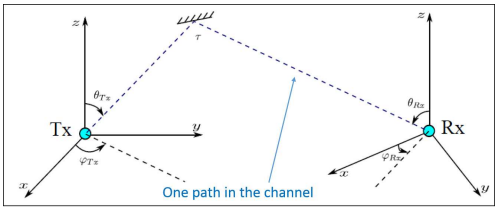

Figure 1: Propagation Parameters

2.2 Parameter Estimation and Obejective of this work

MIMO Channel Matrix, which is dependent on transmitted signal and recieved signal,can be modeled by eq(1).

$$\mathbf{H}(f) = \sum_{l=1}^{L} \boldsymbol{a}_{R,l}\left(\varphi_{R,l}, \theta_{R,l}, f\right) \cdot \boldsymbol{\Gamma}_l \cdot \boldsymbol{a}_{T,l}^{T}\left(\varphi_{T,l}, \theta_{T,l}, f\right) e^{-\mathrm{j}2\pi f \tau_l} \tag{1}$$

where $\mathbf{H}(f) \in \mathbb{C}^{M_R \times M_T}$, $\boldsymbol{\Gamma}_l \in \mathbb{C}^{2\times 2}$ represents tensor form of path weight. L is total number of paths considered, and M_R, M_T is number of antennas elements at transmitter and receiver side, $\boldsymbol{a}_{R,l}, \boldsymbol{a}_{T,l}$ are array response function of anttenna at transmitter and reciever with respect to the all propagation parameters mentioned above and a certain frequency f. Since we are considering a wide-band with multi frequency bin, then eq(1) needs to be expanded as follow.

$$\mathbf{s} = \mathrm{vec}\left\{\mathbf{H}\right\} = \mathfrak{B}(\boldsymbol{\mu}) \cdot \boldsymbol{\gamma} \in \mathbb{C}^{M_R . M_T . M_f \times 1} \tag{2}$$

where M_f is number of sampling points in frequency domain. $\mathfrak{B}(\boldsymbol{\mu}) \in \mathbb{C}^{M_R . M_T . M_f \times 4L}$ is a description to structure of the whole radio channel.$\boldsymbol{\gamma} \in \mathbb{C}^{4L\times 1}$ is vectorization of $\boldsymbol{\Gamma}$. Notice that matrix $\boldsymbol{\mu} \in \mathbb{C}^{L\times 5}$ and $\boldsymbol{\gamma}$ now contains all groups of path paramters. And this 2 parameter matrix is the target that we want to estimate from measured channel transfer function. Eq(3) shows us how to estimate this 2 matrix which is based on *Maximum Likelihood Estimation* [3].

$$\hat{\boldsymbol{\mu}} = \arg\min_{\boldsymbol{\mu}} \left[\left(\mathbf{x} - \mathbf{s}\right)^H \left(\mathbf{x} - \mathbf{s}\right)\right] \tag{3}$$

where $\mathbf{x} \in \mathbb{C}^{M_R . M_T . M_f \times 1}$ is exactly the data of measured MIMO channel transfer function. Therefore, according to this formular, parameter estimation evantually became 5L-dimensional optimization problem. SAGE [3] is a popular algorithm to optimize multi-dimensional discrete function which is very appropriate to be applied in this problem. Because in real measurement, array response $\boldsymbol{a}_{R,l}, \boldsymbol{a}_{T,l}$ are not continous function but discrete data-base with respect to all sampling angle point and frequency point which causes the structure of whole radio channel $\mathfrak{B}(\boldsymbol{\mu})$ can only be changed discretely. The basic concept of SAGE is, first decompose the measured data $\mathbf{x}$ into L part which represent information of L paths, then estimate parameters path by path through optimizing likelihood function of each path. However, SAGE faces problem that estimation accuracy and convergence speed are limited by given number of sampling points of array response which we can call resolution level. Above all, we come to our objective which is applying a gradient-based algorithm instead of SAGE in order to improve performance of MIMO channel parameter estimation.

3 Proposal

3.1 NLCG alogrithm

Non-Liner Conjugate Gradient method is one of the most efficient methods on optimizing multi-dimensional continous function. The basic concept of NLCG is to minimize a multi-dimensional continous function $\mathcal{L}(\boldsymbol{\mu}_l)$ by constructing a series

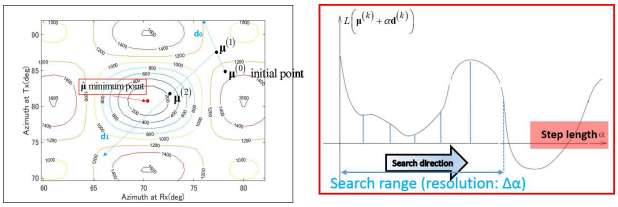

(a) Search direction (b) Step-length-search

Figure 2: Geometric interpretation of NLCG in 2D space

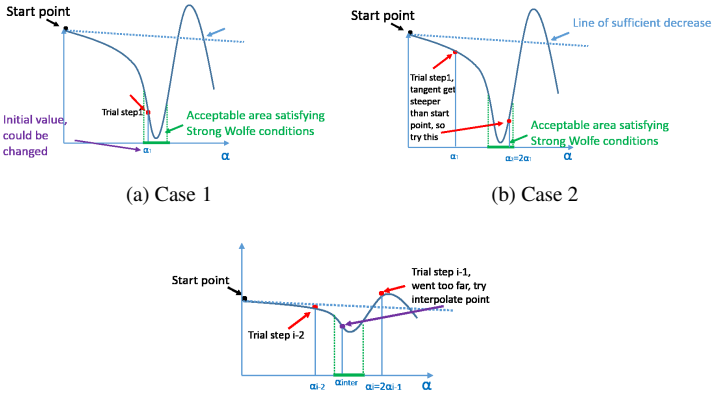

(a) Case 1 (b) Case 2

(c) Case 3

Figure 3: Geometric interpretation of SW condition based step-length-search

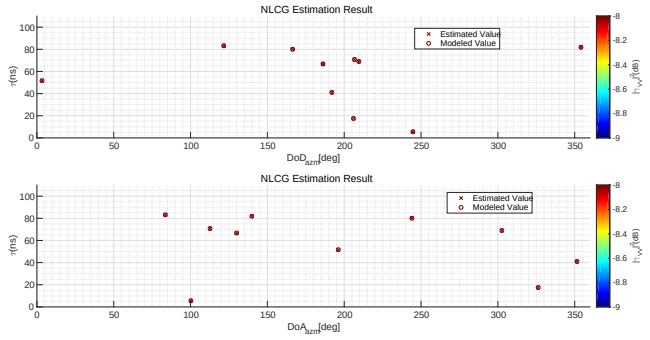

(a) Proposal result

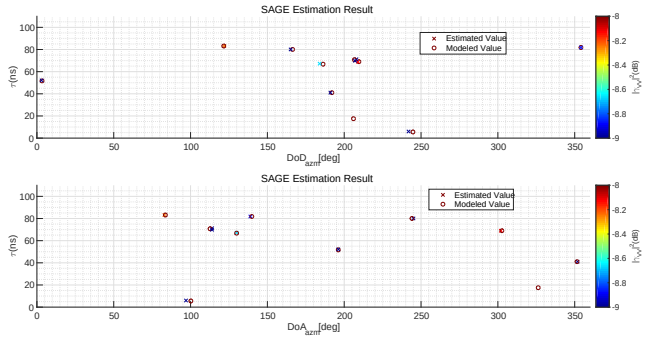

(b) SAGE result

Figure 4: Simulation result under same initialization condition

position vector $\boldsymbol{\mu}_l^{(k+1)} = \boldsymbol{\mu}_l^{(k)} + \alpha^{(k)}\mathbf{d}^{(k)}$ until the function converge at minimizer. where $\mathbf{d}^{(k)}$ is search direction(vector) in each iteration, and it is defined by what we call conjugate garadient which is constructed by gradients. $\alpha^{(k)}$ is called step-length(scalar) that determine how long should it travel along the search direction in each iteration to make function decrease significantly. This method has been introduced in parameter estimation before [2]. but in [2], optimazation result is limited by step-length-search procedure which causes exactly the same problem as SAGE which is resolution limitation. The geometric interpretation of minimum search procedure by [2] is showed in Fig2. In this Fig, we simulated a very simple case, there are only two parameter Azimuth at Tx (φ_T)and Azimuth at Rx(φ_R) in total, so the target function $\mathcal{L}(\boldsymbol{\mu})$ we want to minimize is only 2-dimensional.

3.2 SW condition based step-length-search method

To remove resolution limitation of parameter estimation using NLCG, we introduce a efficient non-resolution based step-length-search method named *Strong Wolfe condtions based step-length-search method* [4]. Strong Wolfe condtions help us to define what kind of step length we need to take. And step-length-search method help us to find such a step length. The search procedure can be visualized in Fig3.

3.3 EADF of Array Response

The neccessary condition for removing resolution out of estimation is to make array response continous. Because of limitation of given sampling angle and frequency points, all we can do is to interpolate the information between every sampling points, and creat a continous function instead of discrete data-base to describe array response. *Effective Aperture Distribution Function method* [5] is the way we did to the data-base. EADF can be considered as multi-dimensional Fourier series expansion of the discrete data-base. An advantage of this approach is that the EADF typically is concentrated to a very small support area which we call effective aperture. Another advantage is we can get derivative at same time because NLCG must require derivative of the target function.

4 Simulation and Evaluation

Fig4 shows the estimation results by both Proposal and SAGE under simulated propagation environment. In this modeled channel, there were 10 paths with 10 group of modeled random paramters. And we gave SAGE and NLCG the same initialization condition, every initial value in delay domain are set into $\tau_l^{(0)} =< \tau_l^{modeled} >$. In angular domain, $\varphi_{T,l}^{(0)} =< \varphi_{T,l}^{modeled} > \pm 4$[deg], and $\varphi_{R,l}^{(0)} =< \varphi_{R,l}^{modeled} > \pm 4$[deg]. <> means nearest interger.

5 Conclusion

In this paper we proposed a gradient-based method to improve performance of radio channel parameter estimation. Compare to SAGE algorithm, this proposal do have advantage on accuracy of estimated results and convergence speed.

References

[1] Calcev, G. and Chizhik, D. and Goransson, B. and Howard, S. and Huang, H. and Kogiantis, A. and Molisch, A. and Moustakas, A. and Reed, D. and Xu, H., 'A wideband spatial channel model for system-wide simulations," *IEEE Transactions on Vehicular Technology*, pp. 389-403, 2007.

[2] Shizhi ZHANG, "11Ghz indoor MIMO Channel Parameter Estimation Using Gradient Method," Master Thesis, Tokyo Institute of Technology, 2014.

[3] B. H. Fleury, M. Tschudin, R. Heddergott, D. Dahlhaus, and K. I. Pedersen, "Channel parameter estimation in mobile radio environments using the SAGE algorithm," *IEEE J. Sel. Areas Commun.*, vol. 17, no. 3, pp. 434-450, 1999.

[4] Jorge Nocedal and Stephen J.Wright, "Numercal Optimization", ed. Peter Glynn Stephen M. Robinson,isbn: 0-387-98793-2, pp. 100-132, Springer-Verlag New York, 1999.

[5] M. Landmann and A. Richter and R. S. Thoma, "DOA resolution limits in MIMO channel sounding", *International Symposium on Antennas and Propagation and USNC/URSI National Radio Science Meeting*, Monterey,CA, pp. 1708-1711, 2004

Concept study of a nano Mars lander with extendable aerodynamic device
Student Number: 12-01775 Name: Yuta IMAI Supervisor: Daisuke AKITA

1 Introduction

1. Concept

This paper proposes a mission that entries Mars' atmosphere and lands on Mars' surface with a nano size lander. The nano lander has two merits that are cost effective and mission flexible.

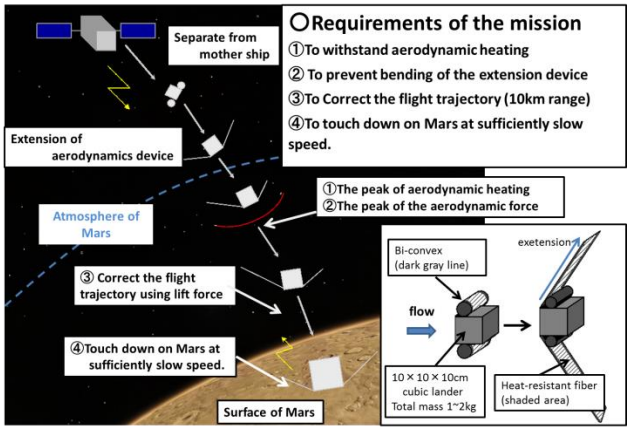

Fig. 1 Mission model

Figure 1 shows the mission scenario. The lander is separated from a mother ship before Mars entry. The extendable aerodynamic device is deployed before the Mars entry. The extendable aerodynamic device reduces the aerodynamic heating during atmospheric entry. The lander withstands aerodynamic heat and land on Mars' surface.

As the extendable devise, bi-convex is used. Bi-convex which has a shape like a combination of two steel tape measures are able to be stored by winding as shown in Figure 2.The extendable aerodynamic device is attached to the lander as shown in Figure. 1.

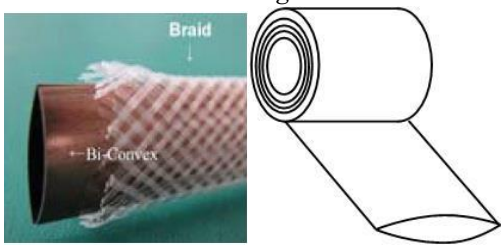

Fig. 2 Bi-convex

This lander has four requirements shown in figure 1.

2. Motion equations and entry trajectory

Motion of the lander is considered in polar coordinates as shown Figure 3.

Forces acting on the lander are only the Mars gravity and the aerodynamic force. The motion equations of the lander are given by Eq. (1).

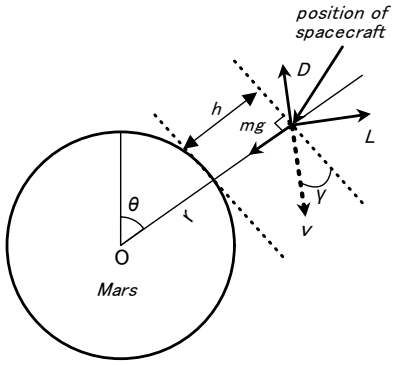

Fig. 3 Motion equations model

$$\begin{cases} \frac{dv}{dt} = \frac{\mu_m}{r^2} sin\gamma - \frac{1}{2}\rho v^2 \ \ \frac{1}{\beta} \\ v\frac{d\gamma}{dt} = -\frac{1}{2}\rho v^2 \ \ \frac{L}{D} \ \ \frac{1}{\beta} \ (\frac{\mu_m}{r^2} - \frac{v^2}{r})cos\gamma \\ \frac{dr}{dt} = vsin\gamma \\ \frac{d\theta}{dt} = \frac{vcos\gamma}{r} \end{cases} \quad (1)$$

t [s]: Time from entry
v [m/s]: velocity
γ[deg]: flight path angle
r [m] : distance from the center of Mars
ρ[kg/m^3]: density of atmosphere
θ[m]: longitude
μ_m[m^3/s^2]: a product of Mars mass and gravitational constant
β [kg /m^2]: ballistic coefficient
L/D[−]: lift − to − drag ratio

The equation is numerically calculated by 4th order Runge-KuttaMethod to estimate a trajectory of the lander. Initial v is 5.6[km/s]. Initial height as shown Figure 4 is 125 [km], Initial flight path angle is 10[deg].

3 Requirements of aerodynamic characteristics

Four requirements ①~④ shown in Fig. 1 come down to requirements of aerodynamic characteristics, which refer to ballistic coefficient and lift-to-drag ratio in this study.

Temperature of surface of the lander have to be less than 900[℃] to protect the payload.

The heat flax [W/m^2] is estimated by Tauber's equation. Temperature of lander is given by Stefan-Boltzmann law using the heat flax given by Tauber's equation.

The result of aerodynamic heating calculation, ballistic coefficient is required to be less than 9.10[kg/m^2].

For requirement ② , maximum dynamic pressure acting on the lander is needed to below 100[Pa] .To meet this dynamic pressure requirement, aerodynamic characteristics are

needed to be inside of blue area in figure 4.

To obtain 10[km] controllable down range, L/D is required to be more than 0.27.Since the landing velocity should be less than 43[m/s] to protect the payload. Result of trajectory calculations, the ballistic coefficient is required to be less than 3.08 to meet the requirement. These consideration shows that the requirements for the Aerodynamics characteristics are $\beta < 3.08$ and $L/D > 0.27$.

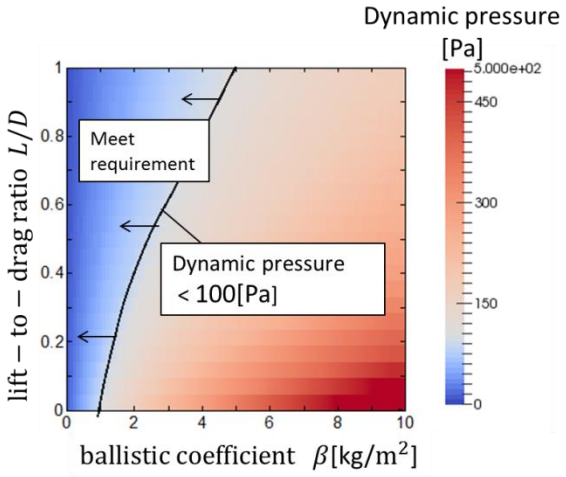

Fig. 4 requirement of aerodynamic characteristics for dynamic pressure condition

4 Estimation of aerodynamic characteristics

The aerodynamic characteristics are estimated by Newtonian impact theory. This theory gives β/m [1/m^2] and L/D. m is the total mass of the lander.

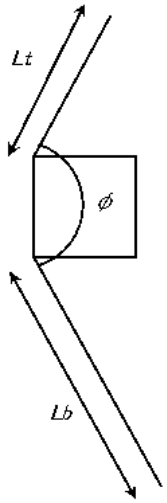

Fig.5 model for Newtonian impact theory

Aerodynamic characteristics of the lander are evaluated for the angle ϕ and Lb/Lt shown in Figure5.

Total mass is estimated from the cross sectional shape of Bi-convex. β/m is given by Newtonian impact theory.

Figure 6 shows a range of angle ϕ and Lb/Lt those meet the requirements when Lb is 3.0[m]. Red shaded area shows feasible design parameters. Figure 7 shows a minimum mass model.

5. Conclusion

It is shown that nano size lander is able to archive landing on Mars' surface. A shape of the lander is shown Fig.6, and mass is 2[kg]. This lander has only small capability of payload, but it has potential to active research Mars.

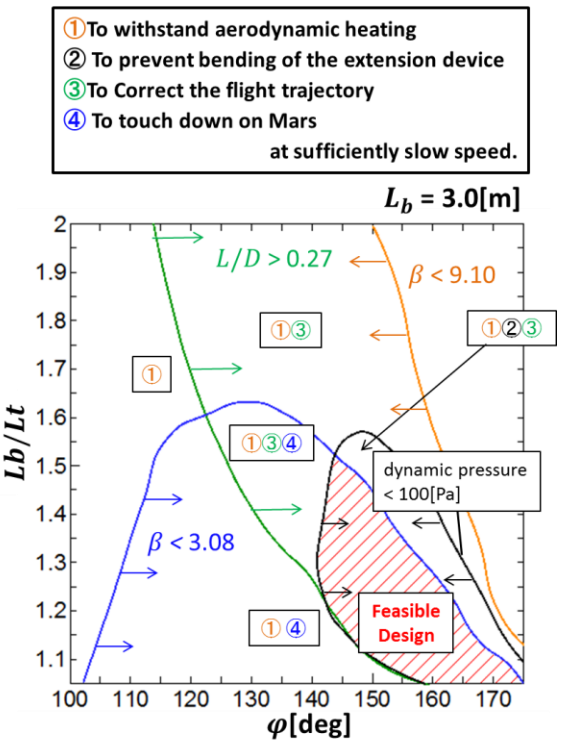

Fig. 6 range of ϕ and Lb/Lt

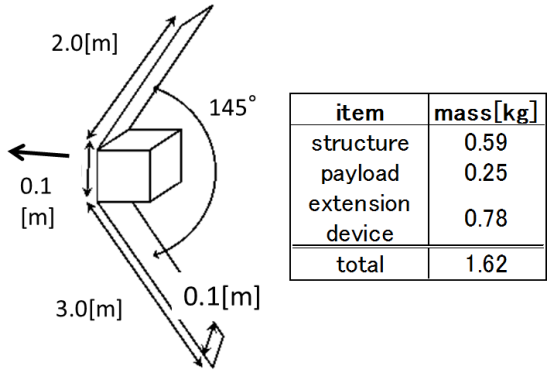

item	mass[kg]
structure	0.59
payload	0.25
extension device	0.78
total	1.62

Fig.7 minimum mass model

References

[1]Shunsuke Tanaka: "An environment of re-entry spacecraft flight", JAXA-RR-04-056 6-2., 2005

[2]Akihiro Tamura: "Analytical solution of the bending of a bi-convex boom", Mechanical Engineering Journal, Vol.2, No.6,2014

[3]Lobia Marcus:"A Framework for the Design and Optimization of Waverider-Derived Hypersonic Transport Configurations", Ph.D.thesis.University of Tokyo ,2003

[4] Michael J. Grant∗ and Robert D. Braun: "Analytic Hypersonic Aerodynamics for Conceptual Design of Entry Vehicles", 48th AIAA Aerospace Sciences Meeting Including the New Horizons Forum and Aerospace Exposition4 - 7 January 2010, Orlando, Florida

Image coding by Slant Vector Embedded Discrete Cosine Transform

Student Number:08_02231 Name:Kento Itai Supervisor:Yukihiko Yamashita

1 Introduction

DCT (Discrete Cosine Transform) is an orthogonal transform which is the most frequently used in image coding, because DCT has the energy compaction property. It can approximate the Karhunen-Loéve transform when the correlation between neighbor pixels are very high [1]. However, basis vectors of DCT are cosine funtions so that DCT is not suitable for encoding a gradiation area where pixel values varies linearly. For that reason, Yamada et. al proposed to selectively use ST (Slant Transform) instead of DCT in a gradation area [2]. In this paper, I propose a more simple method. I embed a slant vector to DCT. I call it SVEDCT (Slant Vector Embedded Discrete Cosine Transform). I show its advantage by experiment.

2 Overview of SVEDCT

I discribe how to embed a slant vector to DCT. Let x be an N-dimensional signal in R^N. Let $\Phi(i)/(i = 0, 1, ..., N-1)$ be the i-th DCT basis function. DCT is given by the inner products between x and Φ_i.

$$X(i) = \langle x, \Phi(i) \rangle. \tag{1}$$

Its inverse transform is given by

$$x = \sum_{i=0}^{N-1} X(i)\, \Phi_i. \tag{2}$$

2.1 SVEDCT

I difine a slant vector s by

$$s(n) = \frac{\frac{N-1}{2} - n}{\sqrt{\sum_{i=0}^{N-1} \{\frac{N-1}{2} - i\}^2}}. \tag{3}$$

Because of the symmetry of DCT, s is expressed by basis vectors of which orders are odd. Therefore, I define α_k $(k = 0, 1, ..., M-1)$, $M \equiv \lfloor N/2 \rfloor$ by

$$\alpha_k = \langle s, \Phi_{2k+1} \rangle. \tag{4}$$

Then, I have

$$s = \sum_{k=0}^{M-1} \alpha_k\, \Phi_{2k+1}. \tag{5}$$

It can be approximated by using $K(\leq M)$ basis functions $\{\Phi_{2k+1}\}_{k=1}^{K}$.

$$\sum_{k=0}^{K-1} \alpha_k\, \Phi_{2k+1}. \tag{6}$$

I difine KK-dimensional ventors $\varphi_0, \varphi_1, ..., \varphi_{K-1}$ by

$$\begin{aligned} \varphi_0(j) &= \alpha_j \\ \varphi_i(j) &= \begin{cases} 1 & (i = j) \\ 0 & (i \neq j) \end{cases} \end{aligned} \tag{7}$$

for $i = 1, 2, ..., K-1$ and $j = 1, 2, ..., K-1$.
I orthogonalize them. It would be better not to mix higher frequency components to lower frequency components because of the energy compaction property of DCT. Therefore, I propose a modified Gram-Schmidt orthonormalization. I denote the orthogonalized vectors by $\varphi'_0, \varphi'_1, ..., \varphi'_{K-1}$. First, let $\varphi'_0 = \varphi_0$. The two dimensional vector $(\varphi_1(0), \varphi_1(1))$ is orthogonalized to $(\varphi'_1(0), \varphi'_1(1))$ by using the original Gram-Schmidt orthonormalization. Then, I pad zeros to $\varphi'_1(j)$. Next, $(\varphi_2(0), \varphi_2(1), \varphi_2(2))$ is orthogonalized to $(\varphi'_0(0), \varphi'_0(1), \varphi'_0(2))$ and $(\varphi'_1(0), \varphi'_1(1), \varphi'_1(2))$. I pad zeros to $\varphi'_2(j)$ similarly. Let U be a (K, K)-matrix of which (i, j)-component is $\varphi'_i(j)$. Since DCT has fast algorithms, I can get SVEDCT by applying U to the first, third,...(2K-1)-th DCT coefficients.

2.2 2D-SVEDCT

For image coding SVEDCT should be extended to a 2D transform. In this paper I propose two extension methods. The first method applies SVEDCT separately to horizontal and vertical directions. I call this method 2DS-SVEDCT (2D separable SVEDCT). However, this method has a disadvantage, since many transform coefficients are different from those of DCT. These differences may make the performance worse because of the energy compaction property of DCT. The other method is to apply SVEDCT to the DC coefficients of DCT for the other coordinate. I call this method 2D-SVEDCT. In this method, differences of coefficients are less. Therefore, it will be possible to

reduce the impact on the energy compaction property of DCT.

3 Experiments

I examined the performance of SVEDCT. Fig.1 shows original images. I compress these images by using DCT, 2DS-SVEDCT, and 2D-SVEDCT. Fig.2 shows the results of image coding. I use the baseline JPEG coding scheme and apply the same quantization factor for all coefficients. The vertical and horizontal axes show the PSNR and the bit rate, severally.

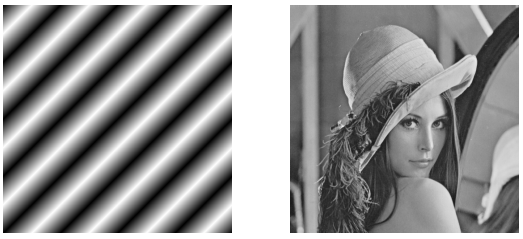

(a) Gradation(artificial) **(b)** Lenna

(c) Barbara **(d)** Peppers

Fig.1: Original images

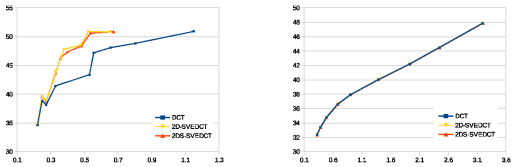

(a) Gradation **(b)** Lenna

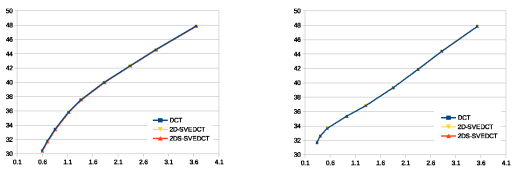

(c) Barbara **(d)** Peppers

Fig.2: Rate distortion relations

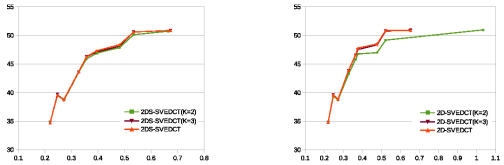

(a) Gradation, 2DS **(b)** Gradation, 2D

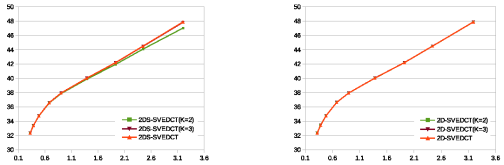

(c) Lenna, 2DS **(d)** Lenna, 2D

Fig.3: Rate distortion relations for K=2, 3, and 4

2DS-SVEDCT and 2D-SVEDCT outperform DCT for the artificial gradation image. For the three natural images, the results by respective transforms are almost the same. Fig.3 shows rate distortion relations for K=2, 3, and 4 at (6). The results by 2DS-SVEDCT (K=2) are worse than those by K=3 and 4. For artificial gradation image, the results by 2D-SVEDCT (K=2) inferior to others. The results by 2D-SVEDCT (K=2, 3, and 4) are almost the same for natural images. In all cases, the performances of K=3 and those of K=4 are almost the same. Therefore I can use K=3 to reduce of the amount of calculations.

4 Conclusions

I proposed the SVEDCT and two types of 2-dimensional SVEDCT. Then, I compare performances of SVEDCT among K=2, 3, and 4. I show the advantages of SVEDCT over DCT and the most suitable value of K by experiments. For future works, I have to conduct experiments with larger image block for example 16×16 (K=2, 3, ..., and 8).

References

[1] N.Ahmed, T.Natarajan, and K.R.Rao, "Discrete cosine transform," IEEE Transactions on computers, vol.C-23, no.1, pp.90-93, (1974)

[2] Yoshihisa Yamada, Shuichi Yamagishi, and Michihiko Minoh: "High quality image coding method for gradation areas by using slant transform", Journal The Institute of Image Information and Television Engineers vol.65, no.11, pp.1594-1602 (2011)

A PROTOTYPE OF ENERGY HARVESTING EQUIPMENT FOR COMPOST HEAT

Student Number: 12-00706 Name: Koomok Lee Supervisor: Takahashi Kunio

1. Introduction

The quantity of waste heat with a low temperature is vast amount. For effective use of unutilised energy, technologies for recovering waste heat have been investigated and thermoelectric module (TE module)Bi-Te based alloys as a thermoelectric material is expected to be used to recover waste heat under 150℃[1]. Among those heat sources, compost heat is expected to be recovered by using TE module. Compost has been used as a soil conditioner and is made when organic materials are decomposed by microorganism in aerobic condition. During composting, the temperature of compost reaches up to 60~70℃ and lasts up to 2 weeks depends on the characteristics of compost[2].Previous studies have investigated the reuse of compost heat as a water heater by designing water pipe inside the composting facility[3]. This paper aims to widen the use of compost heat as a power generation by designing a prototype of energy harvesting equipment using TE modules. By giving temperature gradient across the TE modules using water, this prototyped equipment is devised both as a water heater and power generation. Also, the performance of the equipment was evaluated by the amount of recovered heat energy from water and electrical energy stored in capacitor through energy harvesting experiment.

2. Materials and Method

2.1. Composting materials

Compost reactor (φ:323mm, height:323mm) in Nakasaki lab was used for composting and energy harvesting experiment. As a composting material, oil cake, saw dust and Aurace G were mixed. The mass of compost was 3kg.

2.2. TE module and its I-V characteristic

TE module(9500-127-085B,Ferro tech) is used to convert compost heat to electrical energy. By applying temperature gradient using temperature controller and heat sink across the both sides of the modules, the I-V characteristic of the module was examined to investigate the performance of the module. Current and voltage were measured by varying resistors(1~15Ω).

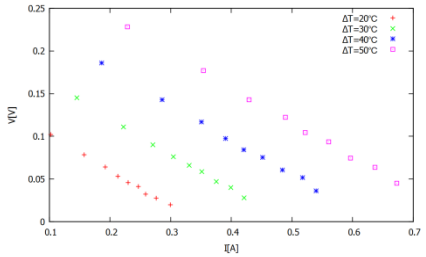

Fig.1: Results of I-V characteristic

The result shows that the TE module has constant internal resistance.

2.3. Prototype of Energy harvesting equipment

Figure 3 shows the prototype that was designed in this study. 15 TE modules were used, i.e. 5 modules were connected in series and 3 of each 5 module in parallel, sandwiched between two copper plates. The prototype is intended to put on top of the compost to have one face heated by the compost, whereas the other face is cooled by water supply. The electrical energy is finally boosted up by a boost converter with tracking the Maximum Power Point (MPPT) of TE module[4], and then stored into the capacitor. Temperature of the compost inside the reactor is monitored and recorded, while the electric potential generated by the prototype is recorded to a logger.

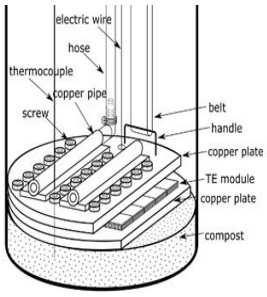

Fig.2: Inside the reactor

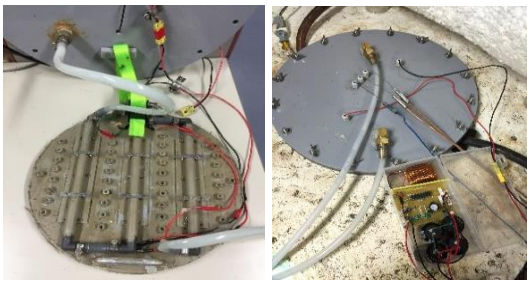

Fig.3: Assembled prototyped equipment

2.4. Experimental description

The energy harvesting experiment was done for 3 times and each experiment was started when the initial temperature of top and bottom side of the compost ranges 60~75 ℃. Heat energy recovered by water, accumulated electrical energy in capacitor and heat of combustion by microbial activity was calculated during the experiment. Air flow rate(30L/h),temperature of air, inlet/outlet temperature of water, water flow rate, accumulated voltage in capacitor, volume percent of CO_2 in exhaust air were measured and monitored to calculate recovered energy. Through each experiment ① , ② , ③ ,few parameters were modified as shown below to

investigate the energy recovery efficiency by water and electrical energy and in an attempt to maximise the temperature gradient across the modules.

①:Water flow rate kept at 30mL/s
②:Water flow rate kept at 15mL/s
③:Water flow rate kept at 30mL/s+pipes covered with polystyrene foam to insulate heat exchange between water and compost heat.

Also, the temperature change of top and bottom of the compost was monitored to investigate the effect of the equipment during the experiment.

3. Results and discussion

The results of each experiment ①,②,③ were shown below.

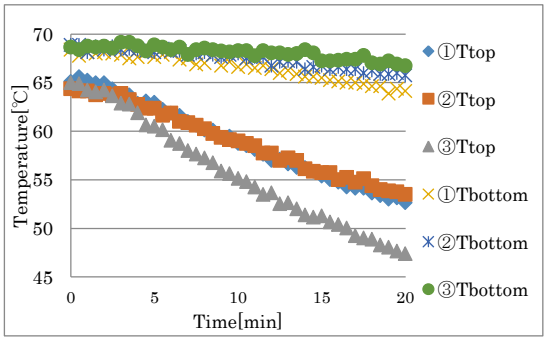

Fig.4: Temperature change on top and bottom of the compost

Table.1: Heat energy recovered by water (Q_w)

	①	②	③	unit
Q_w	673.40	971.00	544.56	kJ

Table.2:Accumulated electrical energy in capacitors (E_c)

	①	②	③	unit
E_c	148.9	107.6	152.1	J

Table.3: Heat of combustion by microbial activity during experiment(Q_m)

	①	②	③	unit
Q_m	1.41	2.16	1.25	kJ

3.1. Recovered energy and temperature of the compost

From the experiment ①, ②, ③, Q_w is much bigger than E_c and Q_m.It means that energy from compost heat is considered to be recovered more efficiently using water compared to as an electrical energy and it is expected that compost will be cooled below 40℃ using the equipment in this composting system. It is necessary to maintain the temperature of compost heap above 50℃ for sterilisation within compost[2]. It is desirable to use large quantity of compost during composting when recovering compost heat using water.

From the experiment ①,②, it is considered that, higher the water flow rate, the more electrical energy will be generated. But in terms of whole compost heat recovery, using water + power generation, the slower the water flow, the more heat energy will be recovered.

From the experiment ①, ③,the result shows that Q_w ① > Q_w③, by insulating the heat exchange between Q_w and Q_m so that ③T_{top} cooled faster than ①T_{top}. Since the quantity of E_c is small amount than that of Q_w, it is difficult to judge the energy efficiency between E_c① and E_c②.

4. Conclusion

This prototyped equipment was made in an attempt to widen the use of compost heat both as a water heater and power generator using TE module. And it is confirmed that through energy harvesting experiment, compost heat will be recovered more efficiently using water than as a electrical energy using TE module. Although the accumulated electrical energy was small amount, it is expected to acquire electrical energy proportional to the increase of the quantity of composting materials. For that, further energy harvesting experiment is needed where the heat of combustion by microbial activity is larger than heat energy loss by water within the composting system.

References

[1]Shindo Takahiko,Nakatani Yujiro,Oishi Takashi, Thermoelectric Generating System for Effective use of unutilized energy, Toshiba review,Vol.63,No.2,(2008)

[2]Nakasaki Kiyohiko, "微生物利用のエコテクノロジー -コンポスト化- ",静岡県資源環境技術研究会,Jun.1997.

[3]G. Irvine, E.R.Lamont, B.Antizar-Ladislao, Energy from Waste: Reuse of Compost Heat as a Source of Renewable Energy, International Journal of Chemical Engineering, Vol.2010, (2010)

[4] Asami Ryushi,Prototype of an autonomous energy harvesting system using boost converter,Tokyo Institute of Technology, master thesis,(2014

Liquid-Liquid Equilibrium of Sodium with Organophosphorus Acid as Extracting Agent

Student Number: 12B14499 Name: Nobuyoshi MORI Supervisor: Ryuichi EGASHIRA, Hiroaki HABAKI

1. Introduction

Solvent extraction is one of the important methods to separate metals, such as rare earth metals [1], where the metals are distributed between aqueous phase and organic phase containing extracting agent. Organophosphorus acid, e.g., 2-ethylhexyl-2-ethylhexylphosphonate (PC-88A) for rare earth metal extraction, is widely used as an extracting agent. In the extraction, the metal is exchanged with hydrogen in the extracting agent as,

$$jM^{n+} + (x+jn)/2\ \overline{(RH)_2} \rightleftarrows \overline{M_jR_{jn}(RH)_x} + jnH^+ \quad (1)$$

where M^{n+} is metal ion in aqueous phase and $\overline{(RH)_2}$ is the extracting agent dimer in organic phase. This transfer of hydrogen into aqueous phase reduces the metal extraction degree. In order to avoid this unfavorable hydrogen transfer, the extracting agent is saponified with any appropriate me tal, such as, sodium, in the practical extraction process[2,3,4]. In this thesis, liquid-liquid equilibrium of sodium with organophosphorus extracting agent was studied for rare earth metal extraction.

2. Experimental

Neodymium was selected as a rare earth metal. Sodium chloride or neodymium chloride hexahydrate was the source of the metals. The pH of the aqueous phase was adjusted with hydrochloric acid or sodium hydroxide at initial. The organic solvent phase was kerosene solution of 2-ethylhexyl-2-ethylhexylphosphonate (PC-88A). All materials were used without further purification. **Tables 1** and **2** show the experimental conditions. The specified amounts of aqueous and organic phases were brought into contact in a conical flask. These phases in the flask were shaken in the constant temperature bath to be equilibrated. After equilibration, settling, and phase separation, both liquid phases were analyzed using ICP-AES (SPS7800, Hitachi High-Tech Science Corporation) and pH meter (F-52, Horiba).

3. Results and Discussion

The material balance of the metal is written as,

$$V_{aq}\,C_{M,aq,0} + V_{org}\,C_{M,org,0} = V_{aq}\,C_{M,aq,eq} + V_{org}\,C_{M,aq,eq} \quad (2)$$

The concentration of metals in organic phase was calculated using this equation with that in aqueous phase. The extraction yield, E_M, and distribution ratio, D_M, of the metal were defined as,

$$E_M = C_{M,org,eq}\,V_{org}/(C_{M,aq,0}\,V_{aq}) \quad (3)$$

$$D_M = C_{M,org,eq}/C_{M,aq,eq} \quad (4)$$

Table 1 Experimental conditions in solvent extraction of sodium

Feed	aqueous solution of sodium, Na (NaCl)
Volume, V_{aq} [m^3]	2.0×10^{-5}
Concentration of Na^+, $C_{Na,aq,0}$ [kmol m^{-3}]	0.25 ~ 1
pH, pH_0	0 ~ 14 (adjusted by HCl, NaOH)
Solvent	kerosene solution of PC-88A
Volume, V_{org} [m^3]	2.0×10^{-5}
Concentration of PC-88A, $C_{RH2,org,0}$ [kmol m^{-3}]	0.25
Temperature [K]	298
Time [h]	12

Table 2 Experimental conditions in solvent extraction of neodymium

Feed	aqueous solution of neodymium, Nd ($NdCl_3\ 6H_2O$)
Volume, V_{aq} [m^3]	2.0×10^{-5}
Concentration of Nd^{3+}, $C_{Nd,aq,0}$ [kmol m^{-3}]	0.005
pH, pH_0	0 ~ 2.0 (adjusted by HCl)
Solvent	kerosene solution of PC-88A w/ or w/o saponification
Volume, V_{org} [m^3]	2.0×10^{-5}
Concentration of PC-88A, $C_{RH2,org,0}$ [kmol m^{-3}]	0.25
Temperature [K]	298
Time [h]	12

At pH_{eq} higher than 5, white turbidity in the aqueous phase was observed and the turbidity was kept even after the settling at pH_{eq}=5. This might result from the surface active effect by the extracting agent saponified with sodium [6]. In the range of high sodium concentration, heterogeneous three phases were formed at equilibrium. The results of sodium extraction are shown in **Figure 1**. Figure 1(a) shows the comparison between the initial and equilibrium pHs, pH_0, pH_{eq}. While, in the range of pH_0<3, pH_{eq} was almost the same as pH_0, pH_{eq} decreased after equilibration, where 6<pH_0.

The Eq.(1) is rewritten for Na^+ as,

$$jNa^+ + (x+j)/2\ \overline{(RH)_2} \rightleftarrows \overline{Na_jR_j(RH)_x} + jH^+ \quad (5)$$

The equilibrium constant of Na^+, K_{Na}, is, thus, represented with D_{Na} as,

$$K_{Na} = D_{Na}\,C_{H,aq,eq}^{\ j}/(C_{Na,aq,eq}^{\ j-1}\,C_{RH2,org,eq}^{\ (x+j)/2}) \quad (6)$$

Based on this equation, $\log[D_{Na}/(C_{Na,aq,eq}^{\ j-1}\,C_{RH2,org,eq}^{\ (x+j)/2})]$ was plotted over $\log(1/C_{H,aq,eq})=pH_{eq}$ in Figure 1(d), which is so-called slope analysis.

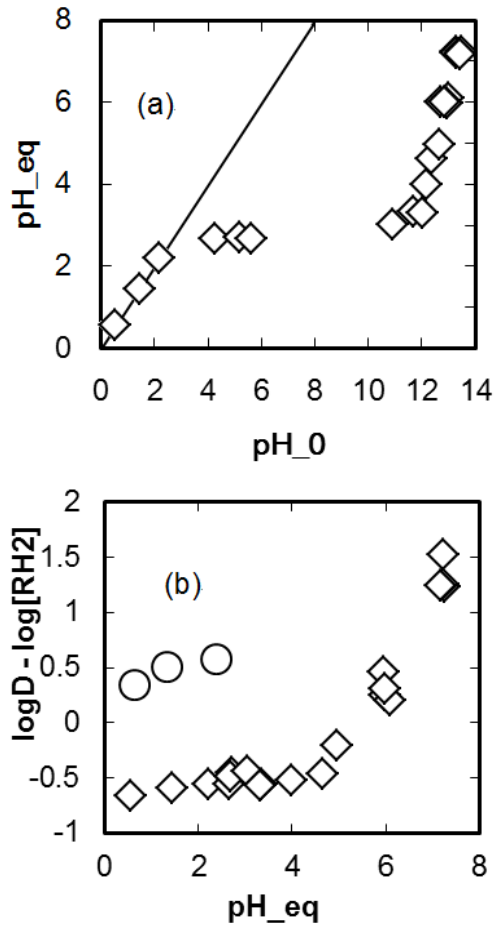

Fig. 1 Results of sodium, Na, extraction (◇ -without saponification, ○-with saponification): (a) pH change; (b) slope analysis under $C_{Na,aq,0}$=2.5×10^{-1} kmol/m^3

In the range of 5<pH_{eq}, these plots gave straight line with j=1, x=1, and K_{Na}=3.12×10^{-6}. Shono *et al.* reported j=2 and x=2 for sodium extraction with bis (2-ethylhexyl) hydrogen phosphate (D2EHPA), when pH_{eq} was higher than 4.0[5]. Where pH_{eq} was lower than 5, $\log[D_{Na}/(C_{Na,aq,eq}^{j-1} C_{RH2,org,eq}^{(x+j)/2})]$ was higher and almost constant over pH_{eq}. Although this was qualitatively attributed to the effect of chloride ion and it was reported that the chloride ion might enhance the extraction of metal by forming complex with metal [7, 8], further study is required.

Figure 2 presents the results of neodymium extraction with and without sodium. Figure 2(a) shows the pH change by neodymium extraction. The pH_{eq} was the same as or lower than pH_0 without sodium. The addition of sodium could prevent the pH reduction as mentioned above. Figure 2(b) shows the extraction yield of neodymium. Neodymium was extracted into solvent phase. The yield increased with pH_0 and exceeded 0.9 at higher pH_0. The yield could be improved by the addition of sodium as predicted. Figure 2(c) shows the slope analysis for neodymium extraction with,

$$j\mathrm{Nd}^{3+} + (x+3j)/2\ \overline{(\mathrm{RH})_2} \rightleftharpoons \overline{\mathrm{Nd}_j\mathrm{R}_{3j}(\mathrm{RH})_x} + 3j\mathrm{H}^+ \quad (7)$$

The experimental results could be well fitted by this reaction formula with j=1, x=3, and K_{Nd}=0.0136, which was much higher than that of sodium, 3.12×10^{-6}. The saponification of extracting agent with sodium did not affect the neodymium equilibrium, whereas neodymium enhanced the sodium extraction as shown in Figure 1(b).

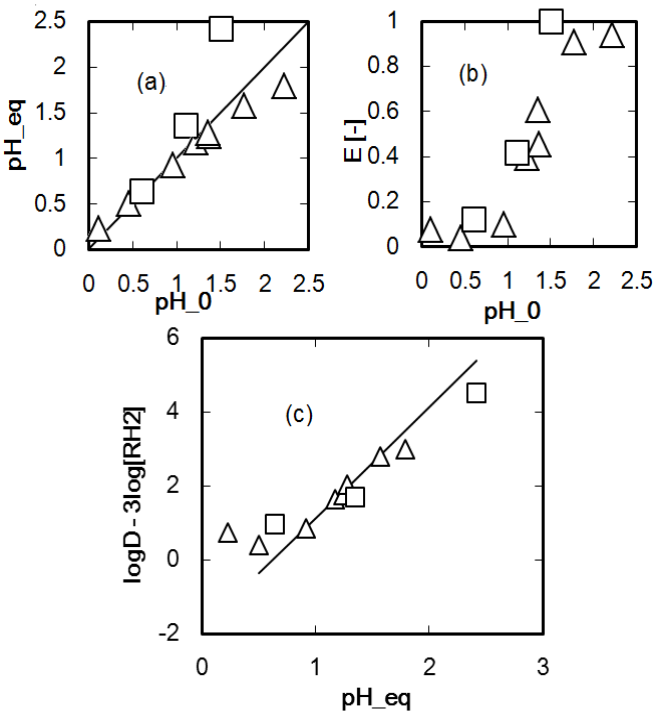

Fig. 2 Results of neodymium, Nd, extraction (△-without saponification, □-with saponification): (a) pH change; (b) extraction yield; (c) slope analysis

4. Conclusions

The liquid-liquid equilibrium of sodium with the extracting agent of PC-88A was clarified. It was confirmed that the extraction of neodymium was improved by the saponification of extracting agent with sodium.

References

[1] 塩川二朗，足立吟也，希土類元素の化学，49, (1981)
[2] Man-Seung Lee et al. Separation Purification Technology 46 (2005) 72-78
[3] I.Kojima et al. Journal of Inorganic and Nuclear Chemistry 31 (1969) 1815-1820
[4] Isao Komasawa et al. Journal of Chemical Engineering og Japan 16 (1983) 210-217
[5] 庄野厚 ほか 化学工学論文集 24 (1998) 609-614
[6] Hailong Hou et al. Chinese Journal of Chemical Engineering 24 (2016) 79-85
[7] F.J.Alguacil et al. Revista de Metalurgia Madrid 35 (1999) 255-260
[8] Thomas Charles Owens Retrospective Theses and Dissertations Iowa State University (1967)

Face Recognition under Various Lighting Conditions Using Relative Karhunen-Loéve Transform

学籍番号: 12B14163　名前: ミョウ　ゲツ　指導教員: 山下　幸彦

1　概要

近年，バイオメトリックス認証やロボットビジョン等の実現を目的として，人間の顔を認識する手法が多数研究されている。しかし，認識する顔画像の撮影条件と，学習用の顔画像の撮影条件が異なる場合，例えば照明等の変動成分が認識画像に含まれる場合，認識性能が劣化するという問題が残されている。

パターン認識のための代表的な類内特徴抽出法の一つに CLAFIC 法 [1](CLAss-Featuring Information Compression) がある。CLAFIC 法は，自分のカテゴリーのパターン集合に関する Karhunen-Loéve Transform 変換 (KL 変換) によって入力パターンから各カテゴリーに関する類内特徴を抽出し，そのノルムが最も大きくなるカテゴリーにパターンを識別する。しかし，CLAFIC 法には特徴空間内で近接したカテゴリーの間で誤認識が生じやすい欠点がある。この欠点を改善するため相対 KL 法 [2][3] を提案され，手書き数字認識実験での有効性が示されている。

本論文では，相対 KL 変換法を使って顔認識実験を行う。本実験により相対 KL 変換法は CLAFIC 法より照明変動による性能劣化を克服できるか検証する。そして，学習データとテストデータの照明条件が大きく違う場合，相対 KL 変換法の方が認識性能が高いかどうか調べる。

2　CLAFIC 法

CLAFIC 法は，パターン認識のための代表的な類内特徴抽出法としてよく知られている。CLAFIC 法では，カテゴリーの KL 変換を用いて類内特徴抽出を行う。カテゴリーの総数を K，特徴空間の次元を N とする。カテゴリー $i(i=1,\cdots,K)$ の KL 変換 $P^{(i)}$ は rank$P^{(i)}=M(M \leqq N)$ という条件で以下の評価基準式 J_1 を最小にする線形作用素 $P^{(i)}$ として定式化される。

$$J_1[P^{(i)}] = \underset{f\in\Omega^{(i)}}{E} \|f - P^{(i)}f\|^2 \tag{1}$$

ここで，f は N 次元パターン，$\Omega^{(i)}$ はカテゴリー i に属するパターンの集合，$\underset{f\in\Omega^{(i)}}{E}$ は $\Omega^{(i)}$ に関する平均を表す。KL 変換 $P^{(i)}$ は，カテゴリー i に属するパターンの相関行列 $R^{(i)}$ の固有値を $\lambda_j^{(i)}(\lambda_1^{(i)} \geq \lambda_2{}^{(i)} \geq \cdots \geq \lambda_N^{(i)} \geq 0)$ とし $\phi_j^{(i)}$ を $\lambda_j^{(i)}$ に対応する固有ベクトルとすると，次式で与えられる。

$$P^{(i)} = \sum_{j=1}^{M} \phi_j^{(i)} (\phi_j^{(i)})^T \tag{2}$$

式 (1) から分かるように，CLAFIC 法は自分のカテゴリーのパターン集合に関する類内特徴を抽出するものである。しかし，自分のカテゴリーだけ着目しているため，他のカテゴリーと区別するために適した特徴とは言えない。即ち，あるカテゴリーに多く含まれる特徴が他カテゴリーにも含まれる場合，そのような特徴を抽出しても類内特徴量の上では差が生じない。

3　相対 KL 変換法

識別に適した類内特徴量抽出は，自分のカテゴリーだけに含まれる特徴を抽出し，他カテゴリーにも共通に含まれる特徴や，自分のカテゴリーに含まれない特徴を抑制するものであると考えられる。次の評価基準 J_2 を与える。

$$J_2\left[X^{(i)}\right] = \underset{f\in\Omega^{(i)}}{E} \|f - X^{(i)}f\|^2 + \alpha \sum_{j\neq i} \omega_j \underset{f\in\Omega^{(j)}}{E} \|X^{(i)}f\|^2 \tag{3}$$

J_2 の第 1 項目は自分のカテゴリーの平均 2 乗近似誤差，第 2 項は他カテゴリーの類内特徴量の平均を表す。パラメータ α は他カテゴリーの抑制度を表している。評価基準 J_2 を最小にする作用素 $X^{(i)}$ を用いて上に述べた類内特徴抽出することができる。

4　実験

本実験の目的は次の 2 つである。相対 KL 変換法は CLAFIC 法より照明変動による性能劣化を克服できるか検証すること，学習データとテストデータの照明条件が大きく違う場合，相対 KL 変換法の方が認識性能が高いかどうか調べることである。

照明問題を扱うための顔データベースとして Yale 大学の Extended YaleFace B が公開されている。このデータベースは，38 個人を 576 条件 (9 姿勢、64 照明方向) で撮影した計 5760 枚の画像で構成されている。64 照明方向はカメラの光軸と光源とのなす方位角と仰角からなる座標で定められる。本論文では，姿勢を正面に限定し，最初の 30 人のデータを使用した。

4.1 実験 I

データベースから 1 人あたり 60 枚の画像 (計 1800 枚) を学習データとしてランダムに取り出した。残りの 4 つの照明方向に対応する画像データ（計 120 枚）をテストデータとした。作用素のランクは今回の学習データに対して最良の認識率を与える値を用いた。相対 KL 変換法のパラメータ α は，予備実験において高成績を収めた 0.01 とした。認識実験 I の結果を表 1 に示す。認識率は CLAFIC 法では 87.5%，相対 KL 変換法では 94.2% であった。

表 1: CLAFIC 法と相対 KL 変換法による認識率

	CLAFIC 法	相対 KL 変換法
認識率	87.5%	94.2%

4.2 実験 II

実験 II では，学習データとテストデータの照明方向の違いが大きい場合の性能を，相対 KL 法と CLAFIC 法で比較した。方位角が 70° より小さい座標に対応するすべて 40 枚の画像を学習データとして，方位角が 70° より大きい座標に対応する画像データから，方位角が 70°，80°，110°，120°，130° の画像データから一つずつランダムに取り出した，計 150 枚の画像をテストデータとした。作用素のランクを 10 に固定して実験した。相対 KL 変換法のパラメータ α は，予備実験において高成績を収めた 0.00005 とした。認識実験 II の結果を表 2 に示す。認識率は CLAFIC 法では 76.0%，相対 KL 変換法では 76.7% であった。

表 2: $\alpha = 0.00005$ の場合の認識率

	CLAFIC 法	相対 KL 変換法
No.1	100%	100%
No.2	100%	100%
No.3	80%	80%
No.4	63.3%	66.7%
No.5	36.7%	36.7%

相対 KL 変換法のパラメータ α が小さいほど，相対 KL 変換法は CLAFIC 法に近づくため，少し大きな値である 0.01 を用いたときの結果を表 3 に示す。

表 3: $\alpha = 0.01$ の場合の認識率

	CLAFIC 法	相対 KL 変換法
No.1	100%	100%
No.2	100%	100%
No.3	73.3%	53.3%
No.4	50%	33.3%
No.5	50%	20%

パラメータ α と認識率の関係を調べるために，様々な α を用いて認識実験を行った。作用素のランクを 9 に固定した。パラメータ α と認識率の関係を図 1 に示す。

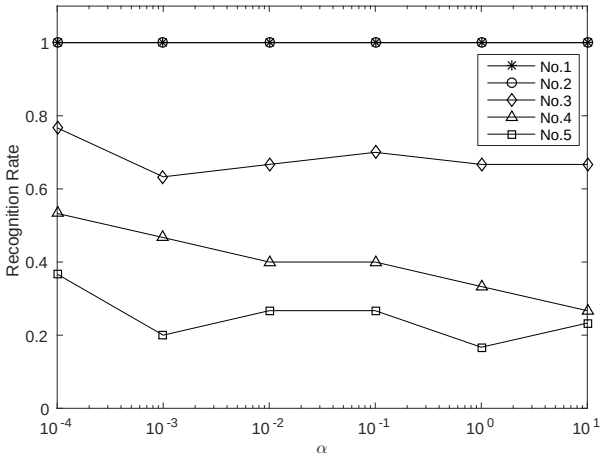

図 1: 認識率とパラメータ α の関係

実験結果から，学習データとテストデータの照明条件が同じ場合，相対 KL 変換法は CLAFIC 法より認識性能が高いことが示された。しかしながら，学習データの照明条件とテストデータの照明条件が大きく異なる場合，相対 KL 変換法及び CLAFIC 法の両方とも認識性能が低かった。また，相対 KL 変換法でも，CLAFIC 法よりあまり高い認識率が得られなかった。

5 結論

相対 KL 変換法と CLAFIC 法の照明変動による性能劣化に関して検証した。学習データとテストデータの照明条件が同じ場合は，相対 KL 変換法が優れていたが，大きく異なる場合は両方法とも性能が低いことが示された。

今後の研究としては学習データとテストデータの照明条件の違いに対して頑健な認識法を開発すること，及び他のカテゴリーを考慮する重みを個別に変える方法に関して研究を進めていく必要がある。

6 参考文献

参考文献

[1] S.Watanabe and N.Pakvasa, *Subspace method in pattern recognition. Proc. 1st International Joint Conference on Pattern Recognition, Washington DC,* pp.25-32, Feb. 1973.

[2] 池野靖行，山下幸彦，小川英光，”相対 KL 変換によるパターン認識 ” 電子情報通信論文誌， vol. 2, pp.1031-1033, Aug. 1998.

[3] Y.Yamasita and H. Ogawa, *Relative Karhunen-Loéve Transform,. IEEE Trans.on Signl Processing.* vol.44, no.2, pp.371-378, Feb.1996.

Influence of water cement ratio, initial chloride content and chloride fixing admixture on corrosion of steel bar in mortar exposed to marine environment

Student number: 11_19571 name: Koki HASHIZUME
Supervisor: Prof. Nobuaki OTSUKI

1. Introduction

For the use of RC structure in marine environment chloride attack is serious for its deterioration due to corrosion of steel bar. To reduce this risk, low initial chloride content and proper water cement ratio (W/C) are recommended

According to previous research of Mizuma[1], after 32 years exposure to marine environment, external chloride ion is much than initial chloride ion. As the result, influence of initial chloride content on corrosion is smaller than that of W/C.

It is considered that chloride ion accelerates corrosion in incubation period. Therefore influence of initial chloride content on corrosion in incubation period cannot be ignored. However influence of W/C and initial chloride content on corrosion in incubation period is not clear.

To reduce influence of initial chloride content on corrosion, the use of Chloride fixing admixture (CF) is considered to be an effective mean. CF has high chloride fixing ability because the main component of CF is calcium aluminate($CaO \cdot 2Al_2O_3$). However in case of using seawater as mixing water, influence of using CF as admixture on material property and corrosion is not clear.

Considering the background, three objectives are set in this study.

1) To clarify influence of W/C and initial chloride content on corrosion of steel bar in mortar exposed to marine environment for 91 days.
2) To clarify the factor that influences on corrosion of steel bar in mortar exposed to marine environment for 91 days and 32 years.
3) To clarify the effect of reducing influence of initial chloride content on corrosion of steel bar exposed to marine environment with using CF as admixture.

2. Materials and specimens

2.1 Materials

Freshwater and seawater(ASTMD1141-98(2003), Cl^- 2%) are used as mixing water. Land sand are used as aggregate. SR235 (Φ: 9mm, length: 100mm) are used for reinforcement. Cement type is OPC (density: 3.17g/cm^3, specific surface area: 3180cm^2/g). CF (DENKA) is used as admixture.

2.2 Specimens

Specimens are prism mortar (40x40x160mm). In mortar, there is steel bar (the cover is 15mm) to clarify oxygen permeability and corrosion behavior. Table 1 shows mix proportion of mortar used in this study. W/C has 3levels (45, 55, 65%). Mixing water has 6types (W: tap water, S: seawater, 0.25S and 0.5S: diluted seawater to two and four times, 2S and 4S: concentrated chloride ion in seawater two and four times). The replacement ratio of CF is 10%.

2.3 Exposure environment

These specimens are exposed to artificial tidal environment. Tidal cycle is 12 hours. This is because to reproduce same environment of specimens exposed to marine environment for 32 years.

3. corrosion after 91 days' exposure

Figure1 shows influence of W/C and initial chloride content on corrosion current density (i_{corr}) after 91 days exposure. Besides 0.2μA/cm² proposed by FIB is used to judge corrosion of steel bar. According to Figure1, influence of W/C is not confirmed. On the other hand, it is confirmed that as initial chloride content increases, i_{corr} increases.

Figure2 shows influence of oxygen permeability and chloride content on steel bar on i_{corr} after 91 days exposure. According to Figure2, influence of oxygen permeability on i_{corr} is not confirmed. On the other hand, it is confirmed that as chloride content on steel bar increases, i_{corr} increases.

Table 1 mix proportion of mortar specimens

Specimens Mark	W/C (%)	Initial chloride content (kg/m^3)	C (kg/m^3)	CF (kg/m^3)	W (kg/m^3)	S (kg/m^3)
45-W	45	0	652	0	297	1304
45-0.25S	45	1.45	652	0	297	1304
45-S	45	5.82	652	0	297	1304
45-2S	45	11.6	652	0	297	1304
45-CF	45	5.82	587	65.2	297	1304
55-W	55	0	613	0	337	1225
55-0.25S	55	1.67	613	0	337	1225
55-0.5S	55	3.34	613	0	337	1225
55-S	55	6.67	613	0	337	1225
55-2S	55	13.35	613	0	337	1225
55-4S	55	26.7	613	0	337	1225
55-CF	55	6.67	551	61.3	337	1225
65-W	65	0	577	0	375	1154
65-0.5S	65	3.72	577	0	375	1154
65-S	65	7.43	577	0	375	1154
65-4S	65	29.72	577	0	375	1154
65-CF	65	7.43	519	57.7	375	1154

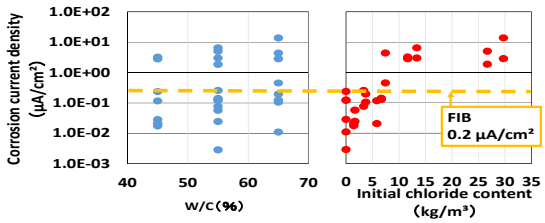

Figure 1 influence of materials on i_{corr}

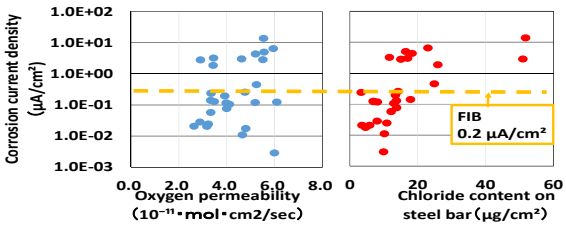

Figure2 influence of material properties on i_{corr}

Table2 T value of material to corrosion

Objective / Explanatory	Corrosion current density After 91 days exposure	Corrosion current density After 32 years exposure[1)]
W/C	0.62	1.33
Initial chloride content	5.12	1.54

Table3 T value of property to corrosion

Objective / Explanatory	Corrosion current density After 91 days exposure	Corrosion current density After 32 years exposure[1)]
Oxygen permeability	0.94	3.71
Chloride content on steel bar	4.41	0.28

4. Multiple regression analysis on the factor that influence on corrosion

Multiple regression analysis is used to evaluate influence on corrosion. Values in Table3 and Table4 show "T value". Generally, absolute value of "T vale" exceeding 2.0 shows major influence.

According to Table3, after 32 years exposure, influence of W/C and initial chloride content on i_{corr} is not confirmed. On the other hand, after 91 days exposure, correlation between initial chloride content and i_{corr} is confirmed.

According to Table4, after 32 years exposure, correlation between oxygen permeability and i_{corr} is confirmed. And after 91 days exposure, correlation between chloride content on steel bar and i_{corr} is confirmed.

Comparing the result of 91 days exposure with that of 32 years exposure, it is confirmed that chloride ion on steel bar has large influence on corrosion in incubation period and oxygen permeability has large influence on corrosion after propagation.

5. Influence of CF on corrosion

5.1 Influence of CF on material property

Figure3 shows influence of CF on material properties (chloride content on steel bar, chloride fixing ability and oxygen permeability) are measured after 91 days exposure. According to Figure3, Chloride content on steel bar in mortar mixed with CF is reduced to almost the same amount of that mixed with freshwater. Chloride fixing ability in mortar mixed with CF is higher than that mixed with freshwater. Oxygen permeability in mortar mixed with CF is almost the same amount of that mixed with freshwater.

5.2 Influence of CF on corrosion behavior

Figure4 shows influence of CF on corrosion behavior of steel bar. According to Figure4, corrosion behavior of steel bar in mortar mixed with CF is not so different from that mixed with freshwater.

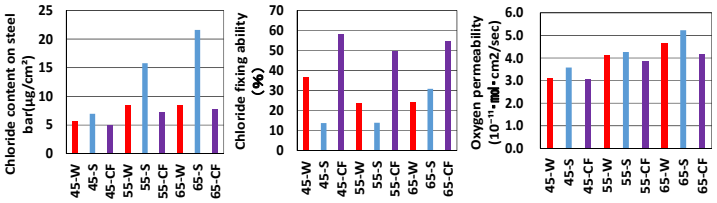

Figure3 influence of CF on material properties

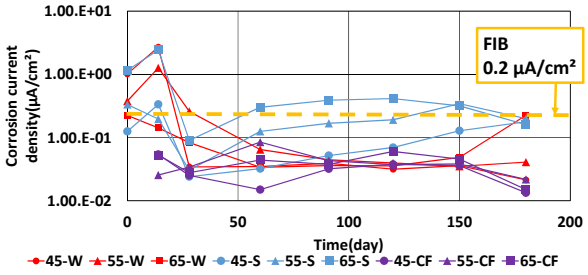

Figure4 influence of CF on i_{corr}

From above results, CF can reduce influence of initial chloride content on corrosion in incubation period.

Because corrosion behavior move to propagation period and corrosion rate is controlled by oxygen permeability. It can be considered that CF doesn't influence on corrosion behavior after propagation.

6. Conclusion

1) Initial chloride content has a large influence on i_{corr} of steel bar in mortar exposed to marine environment for 91 days. On the other hand, influence of W/C on i_{corr} is not confirmed.
2) Chloride content on steel bar has a large influence on i_{corr} of steel bar in mortar exposed to marine environment for 91 days. On the other hand, oxygen permeability has a large influence on i_{corr} of steel bar in mortar exposed to marine environment for 32 years.
3) CF can reduce influence of initial chloride content on corrosion of steel bar in mortar exposed to marine environment.

It is clarified that chloride ion in mortar has large influence on corrosion in incubation period. However in case of using CF as admixture, CF can reduce influence of corrosion behavior of steel bar in mortar mixed with seawater.

7. Reference

1) Ayako Mizuma (2014) Influence of initial chloride content and water cement ratio on corrosion of steel bar in mortar exposed to marine environment for 32 years, bachelor thesis in Tokyo institute technology

Environmental Strategies observed in Enterprise Cooperation in Japanese Automotive Industry

Student ID : 12_09239, Name: Kyosuke TANAKA, Supervisor : Naoya ABE

1. Introduction

In Japan, automotive industry is considered one of the major industries which support the national economy. The industry has many related industries and the competition among the automotive companies at global scale has been more and more getting. Automotive industry has been also one of the major targets of environmental regulations by governments because the production of this industry requires quite large amount of resource inputs and also emit various type of solid and ambient pollutants, if there is no treatment.

An environmental regulation in Japan started in 1973, which set limits to the amount of specified gas emissions, namely CO (carbon monoxide), HC (hydrocarbon), and NO_x (nitrogen oxides). In addition to these emission controls, fuel efficiency and noise reduction regulation were adapted one after another.

From a global environmental regulatory point of view, as shown in figure 1, the historical trends of NO_x & PM (particulate matter) regulation levels in Japan, EU (European Union) and the U.S. are not necessarily the same but continuously getting more stringent, implying that the compliance with various regional environmental regulations are also challenges for globally operating automotive firms. Automotive companies thus could have stronger incentives to figure out how they could maintain their competitiveness in the global market due to more stringent environmental regulations.

Increasing public interest in environmental problems and the attitudes by corporates could be found in realized social responsibility of eco-friendly products, research and development. To be executed it, there are different possible approaches which include both consideration for environment and growth of its enterprise, that is, "environmental strategies." In order to compete in the globally competitive market, automotive enterprises seek to take various measures and one of them is "cooperation" with other enterprises.

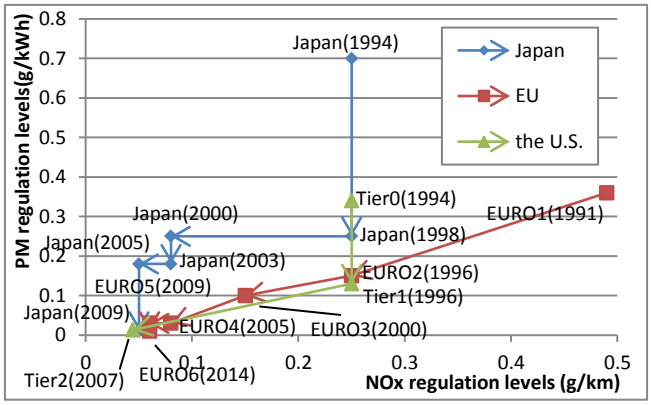

Figure 1 The trends of NOx and PM regulation levels (Source: Compiled by the author based on Japan's governmental data)

In order to compete in the globally competitive market, automotive enterprises seek to take various measures and one of them is "cooperation" with other enterprises. From the view of enterprise management, enterprise co-operation aims to realize mutually larger profits among parties and possibly increasing their own market share. [1] Remarkable point is that some of them cause by adopting renewal regulations, though the relationship between regulation and effect is not clear.

Thus the objective of this study is to investigate whether or how environmental regulations have influenced on enterprise cooperation.

2. Literature Review

There are some of literatures evaluating whether environmental regulations let companies to be more innovative, even if those are supposed to be the threat. Porter(1991) built the following hypothesis; "Strict environmental regulations do not inevitably hinder competitive advantage against foreign rivals; indeed, they often enhance it."(Porter, 1991) Some of economists insisted stronger regulations may become repellents to grow market competitiveness, but others argue it can be vitalizing external factors to research and development.

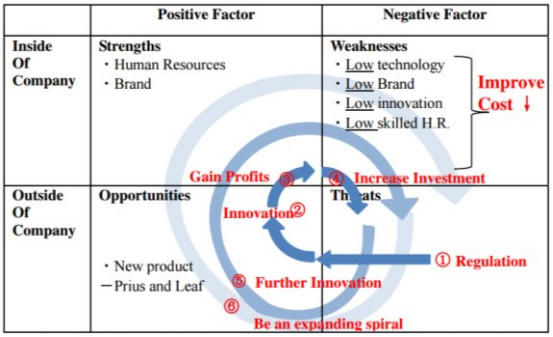

Figure 2 SWOT Evolution between Regulations and Innovation (Source: Debnath (2015))

Debnath (2015) applied SWOT analysis to evaluate the roles of external regulations. Figure 2 shows regulations can create innovations to help to develop a new product and gain profits; moreover they lead to increase investment for corporates. These efforts helped companies to improve their technological capabilities, and these flows can help companies to create further innovations. This spiral is basically synonymous with "innovation offset", which means regulations work efficiently to improve technologies.

Like this, there are some of theoretical researches of regulation efficiency, but few empirical researches are organized based on actual data. The significance of this study is worth of an example of empirical analyses of Japan's enterprise decision-making through some of regulations.

3. Data Collection and Methodology

For the objective above, the data and information about the historical evolution as well as the forms of automotive enterprise cooperation were collected. The main source of the information includes empirical data recorded in each firms and article reporting news. The analysis covers from 1978 to 2014 for those automotive enterprises which are members of JAMA (the Japan Automobile Manufacturers Association, Inc.) Some foreign companies were also considered when they were partners of a Japanese automotive enterprise.

Table 1 shows the list of the car firms, which were considered in this study and Table 2 shows the types of cooperation among the firms. As Table 2 indicates, six different forms of enterprise cooperation were identified based on details in enterprise cooperation recorded in empirical data.

Analysis method we conduct is categorizing empirical data into 6 forms and observing the changes of each cooperation forms. And compering the changes and environmental regulations, we evaluate how regulations effect on cooperation.

Table 1 The list of analysis target firms

	Target firms		
Japanese Firms	Toyota	Nissan	Mazda
	Honda	Suzuki	Subaru
	Daihatsu	Mitsubishi	Isuzu
	Hino	Fuso	UD Trucks
Foreign Firms	Renault	Daimler	General Motors
	PSA	BMW	Ford
	Fiat	Sollers	Tesla Motors

Table 2 Categorized forms of cooperation

No. of Category	Cooperation forms	No. of Pairs
1	Capital Cooperation	17
2	Production Commitment	8
3	Completed Vehicle OEM	27
4	Equipment OEM	17
5	Joint Development (to cope with environmental regulation)	11
6	Joint Development (towards others)	9

4. Analysis and Results

Fig. 3 shows the changes of Japanese automotive enterprises cooperation divided into above 6 forms. There are following remarkable 3 points. First, since 1990s, 4) equipment OEMs are rapidly increasing, second, 5) environmental technological development can be also flourish from the later 1990s. Last, many of 1) capital cooperation have been adopted since 1970s, however, this aspect may be easy to reflect from national economy situation.

Considering increasingly tighten environmental regulations since 1990s, a hypothesis can be designed; 4) and 5) are deeply related to the trend of regulations. This period of Japanese history was in the collapse of the bubble economy; in addition, our interest in environmental problems had been heightened because of Kyoto Protocol held in 1997. In these situation, diesel engine (esp. made by Mitsubishi and Isuzu) gained attention as eco-friendly engine, because of high fuel economy and efficient output. From the view of cost reduction, equipment OEM has been more popular. These are main reasons of 4)'s rapid spike. On the other hand, since 1998, 5) has progressive changes because Japanese enterprises have cooperated with foreign ones in technological development caused by sharing mutual interests. Both 4) and 5) are extremely influenced by strengthened regulations from 1997 to 2005, which reveal regulations at those times had great impacts on the automotive industry.

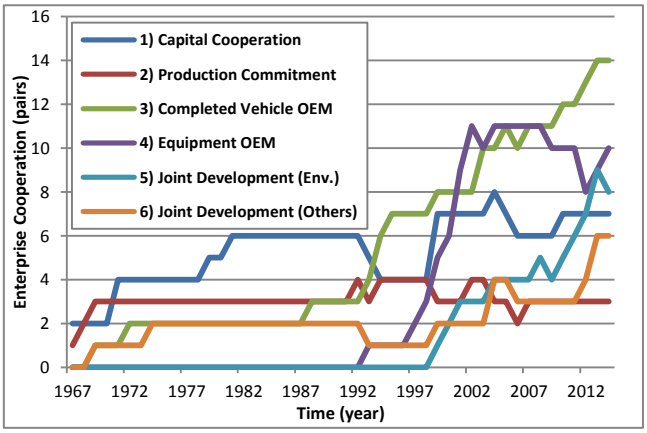

Figure 3 The changes of Japanese automotive enterprise cooperation trend (Source: Compiled by the author based on empirical data)

Nowadays, among 12 Japanese firms, 2 enterprises have adopted 4) and 5) extremely actively: Toyota and Nissan. These two firms expand their business in different background; Toyota has mainly regard capital cooperation as core management, while Nissan has done OEM relationship. However, in the aspect of resent environmental technological development, the two firms have similar enterprise cooperation trends.

5. Conclusion

This study reveals that environmental regulations deeply linked to equipment OEMs and environmental technological developments based on the empirical data, which was compiled by the author. This study found that Toyota and Nissan, which are the leading company in the Japanese automotive market, tend to have more connections with other automotive enterprises, and confirmed that they play significant role to develop environmental technologies.

REFERENCES

[1] Angel Martínez Sánchez et al. (2003), "Cooperation and the Ability to Minimize the Time and Cost of New Product Development within the Spanish Automotive Supplier Industry", *Journal of Product Innovation Management* Vol.20(1), pp.57–69

[2] Porter, Michael E. (1991), "America's Green Strategy," *Scientific American*, 264, 16

[3] S.C. Debnath(2015), "Environmental Regulations Become Restriction or a Cause for Innovation – A Case Study of Toyota Prius and Nissan Leaf", Social and Behavioral Sciences 195, 2015, pp.324-333

The prototype of side-contact type elastic multi-beam using PDMS

Student Number: 12_13212, Name: Mai Ngoc Trung, Supervisor: Kunio Takahashi

1. Introduction

Gecko can move quickly on walls and ceilings [1]. They have a lot of fine hairs on their fingers surface, which are called setae and spatula. The hairs work like springs which can absorb surface roughness and generate enough adhesion force [2]. Adhesion devices which mimic a fine hair structure gecko were prototyped [3-5]. However, compliance with rough surface and easy detachment of the existing devices are still insufficient.

A theory of adhesion between an elastic beam and a rigid body is proposed using linear beam theory [6]. In this study, based on this model, the adhesion device of multi-beam was prototyped and evaluated the performance.

2. Theoretical study and design

The relation between normalized force and normalized displacement with different value of parameter τ is shown in Fig.1.

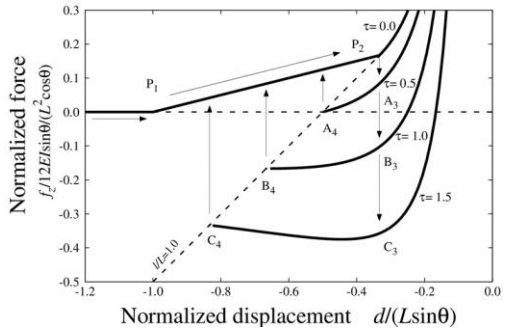

Fig.1 The relation between force and displacement

The parameter τ, related to dimensions (L, H), mounting angle (θ in Fig2) of the beam and work of adhesion $\Delta\gamma$, is defined as

$$\tau = \sqrt{\frac{6\Delta\gamma L^2}{EH^3}} \frac{1}{\tan\theta} \qquad (1)$$

, where E, H, L is Young's modulus, thickness, length of the beam. θ is mounting angle.

In order to the gripping force can be generated, the value of τ must satisfy

$$\tau > 0.5 \text{ [7]}. \qquad (2)$$

Based on this condition, the dimensions, material of the beam were determined. The dimensions of the multi-beam are shown in Fig.2. The material of the multi-beam is PDMS (Polydimethylsiloxane). The number of beams is 24 (4 rows with 6 beams in one row) and distance between rows and beams is respectively 9mm, 2mm.

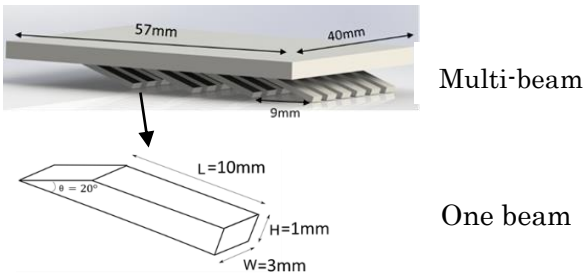

Fig.2 Dimensions of multi-beam

3. Fabrication procedure

In this study, fabrication method of the multi-beam is pouring the PDMS mixture into the mold. The multi-beam was produced as below (3 steps).

3.1 Making mold (Step1)

The mold used in this study was designed as assembly-type mold. From unit molds, arrange in a row (Fig.4b), fix with pins and screws (Fig.4c). The material of the mold is stainless (SUS304).

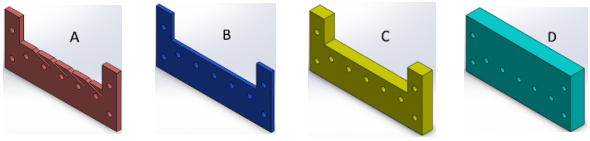

(a)Unit molds

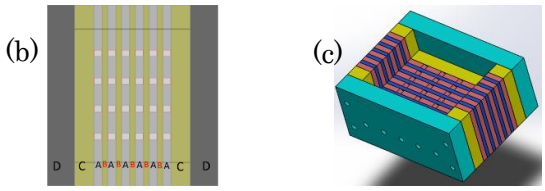

Fig.3 Assembly-type mold

3.2 Making multi-beam (Step2)

Process of pouring PDMS into the mold is shown in Fig.4.

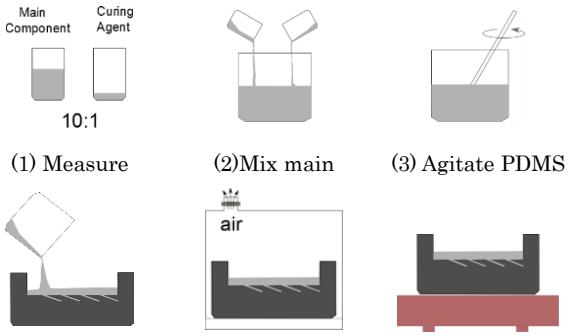

(1) Measure | (2)Mix main | (3) Agitate PDMS

(4) Flow PDMS into the mold | (5) Draw vacuum | (6)Cure PDMS (12h,60℃)

Fig.4 Process of pouring PDMS into the mold

3.3 Surface coating (Step3)

In order to absorb the roughness of the beam surface, the multi-beam is coated with different ways.

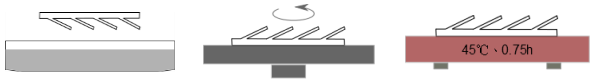

(1) Put into coating agent　(2)Rotate in spin coat　(3)Cure PDMS (1h,45℃)

Fig.5 Process of coating

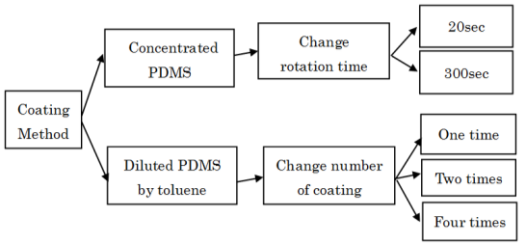

Fig6. The different ways of coating

4. Experiment and discussion

4.1 Experiment

The schematic illustration of experimental apparatus is shown in Fig.7.

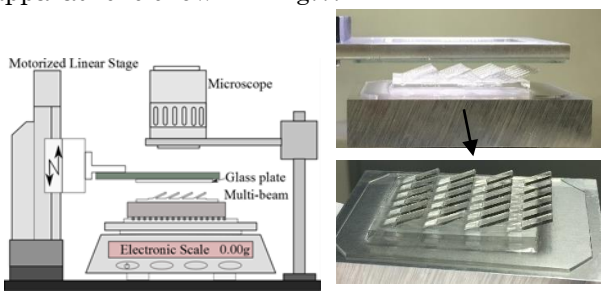

Fig.7 The experimental system.

For performance evaluation of the multi-beam, force against the displacement when the beam is in contact with the rigid body was measured. The result of the experiment is shown in Fig.8.

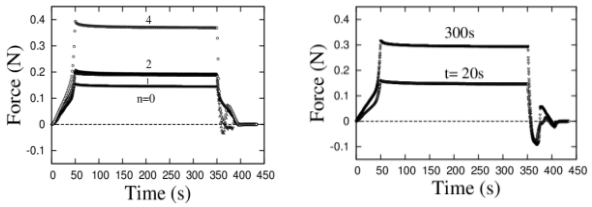

a)Coating by diluted PDMS by toluene with different number of coating time (n=0→4)　b)Coating by PDMS one time with different rotation time (t=20,300sec)

Fig.8 Experimental result of the measured force

4.2 Discussion

By the coating, there are 2 effects.

Effect1: Roughness of the surface beam can be absorbed effectively, this makes contact condition be better.

Effect2: Because of increase of thickness of the beams and accumulation PDMS at the base of the beam, the stiffness of the beam is larger.

The maximum gripping force of multi-beam is shown in Fig.9. As shown in Fig.9a, the adhension force of multi-beam coated by diluted is steady increase when the number of coating is from 0→1→2 times. The reasion of this result is considered that because of improvement of the beam surface (effect1).

However, the adhension force decreases from 2 to 4 times of coating. It is considered that because of the increase of the stiffness of the beam, as shown in Fig.10 (effect 2). The highest adhension force is when the number of coating is 2 times (34mN).

As shown in Fig.9b, the adhension force of multi-beam coated by PDMS are almost same, about 80mN. The adhension force was larger than when coating by diluted PDMS.

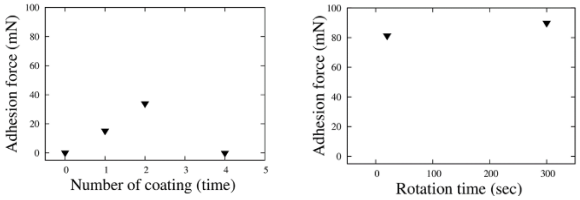

a)Coating by diluted PDMS　b)Coating by PDMS

Fig.9 Adhesion force with different ways of coating

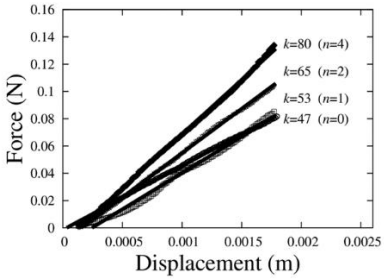

Fig.10 Stiffness of multi-beams coating by diluted PDMS　(n is number of coating time)

5. Conclusions

By using the method of flowing the resin into the assembly-type mold, multi-beam was prototyped. Different ways of coating surface beam was considered. The adhesion force was compared and the result shows that coating by PDMS is more effective than diluted PDMS by toluene.

References

[1] Autumn K, et al, Nature 405, 681-685, 2000.
[2]Takahashi K, et al, J. Adhesion& Adhesive 26, 639-643, 2006
[3] Giem A., et al, Nature Materials, 2, 461 – 463, 2003
[4] Sangbae Kim, et al, IEEE Transactions on Robotics, Vol 24 no1, 65-74, 2008.
[5] Hoon Eui Jeonga, et al, PNAS vol.106 no.14, 5639-5644, 2009
[6] Sekiguchi Y, et al, J Adhesion Science and Technology, Vol 26, 2615-2626, 2012.